Form and Function of Photoreceptors in *kcnv2* Mutant Zebrafish: Implications for the Human Disease *KCNV2* Retinopathy

by

Nathan Joseph Nadolski

A thesis submitted in partial fulfillment of the requirements for the degree of

Master of Science

Medical Sciences - Medical Genetics
University of Alberta

© Nathan Joseph Nadolski, 2020

ABSTRACT

KCNV2 retinopathy is a rare inherited retinal disease caused by mutations in the gene *KCNV2,* which encodes the potassium channel subunit $K_V8.2$. Expressed by photoreceptors, $K_V8.2$ is a critical component for the efficient generation of a neural response to light. *KCNV2* retinopathy is characterized by an abnormal light- and dark-adapted electroretinogram (ERG) waveform, macular photoreceptor degeneration, and variable associated vision deficits such as night blindness, photophobia, a central blind spot, colour blindness, and a reduction in visual acuity. The pathology underlying *KCNV2* retinopathy is currently unknown, so I set out to develop a zebrafish animal model of *KCNV2* retinopathy with the intention of examining both functional and cell biological changes caused by the absence of $K_V8.2$. Here, I have used CRISPR-Cas9 mutagenesis to generate a line of zebrafish harbouring presumptive loss-of-function variants of *kcnv2a* and *kcnv2b*, homologs of human *KCNV2*. I also developed a novel approach to the zebrafish ERG that allowed us to measure the visual function of *kcnv2* mutants. In addition, I evaluated the retinal morphology of *kcnv2* mutants with optical coherence tomography (OCT), a common clinical assessment for human ocular diseases. Finally, I performed histology on *kcnv2* mutant zebrafish retinal tissue to assess potential cellular changes. *kcnv2* mutant zebrafish exhibited subnormal ERG amplitudes and delayed responses in both dark- and light-adapted conditions. Furthermore, the retinae of *kcnv2* mutant zebrafish presented with several OCT abnormalities including an unusual signal between the ellipsoid and RPE layers, hyperreflective spots, and retinal holes. Histology revealed dysmorphic photoreceptor outer segments in *kcnv2* mutants that were correlated to a reduction in visual function. This thesis documents the development and characterization of a novel zebrafish model of *KCNV2* retinopathy. At the juvenile and young adult stages, the zebrafish model already shares phenotypic characteristics

with human *KCNV2* retinopathy patients, and I anticipate that this model will provide valuable insights into both photoreceptor biology and the enigmatic pathology of *KCNV2* retinopathy.

PREFACE

This thesis is an original work by Nathan J. Nadolski. Approval for this study was obtained from the Animal Care and Use Committee: Biosciences, under protocol AUP1476.

All illustrations are original works unless otherwise stated. Figure 1.8 was reused with permission from Barnes (1994) (licence number: 4907141260031).

Chapter 3 is modified from a manuscript of the same title that was published in *Documenta Ophthalmologica* on July 20, 2020 with a citation as follows:

Nadolski, N. J., Wong, X. L. C., & Hocking J. C. (2020) Electroretinogram analysis of zebrafish retinal function across development. *Doc Ophth.* doi:10.1007/s10633-020-09783-y

Chapter 3 was reprinted with permission from Springer Nature Publishing under licence number 4906711105892. Approval for the work in this chapter was obtained from the Animal Care and Use Committee: Biosciences, under protocol AUP1476. All authors of Chapter 3 contributed to the study conception and design. The 3D apparatus described in Chapter 3 was designed by Nathan Nadolski. The schematics for the 3D apparatus can be downloaded through the publication listed above. Material preparation, data collection and analysis were performed by Nathan Nadolski and Casey Wong. The first draft of the manuscript was written by Nathan Nadolski and all authors commented on previous versions of the manuscript. All authors read and approved the final manuscript.

To my fiancé, Kris.

ACKNOWLEDGEMENTS

I would first like to thank my supervisor, Dr. Jen Hocking, for taking me on as her first graduate student. You have been a phenomenal mentor whose expertise, support, and friendship has helped me grow both professionally and personally. Your unwavering curiosity and proficiency in understanding topics outside of your research area are qualities that I greatly admire. Thank you for giving me the opportunity to work under your guidance; it was an experience that I will be forever grateful for.

I would also like to extend my gratitude to my committee members, Dr. Andrew Simmonds and Dr. Joe Casey and my external examiner, Dr. Fred Berry. “I’m having a hard time following your logic” is never a phrase you want to hear during a committee meeting; however, I believe the honest feedback and guidance you both provided set a sensible course for my research project. I would especially like to thank Dr. Simmonds for his daily one-liners and seemingly bottomless pool of knowledge.

The 2020 COVID-19 global pandemic has emphasized the value of friendship and connection. I am immensely grateful for the relationships I have made throughout my graduate studies. To Lance and Nicole, especially, thank you for being my friends. The many mid-afternoon Sherlock’s meetings and weekly Dungeons & Dragons adventures with Gavin, Sam, and Casey will be extremely hard to beat.

No one knows the highs and lows of my graduate studies better than my fiancé, Kris. I want to thank you for your unconditional love and support. The countless hours and days staring puzzled at electrical noise alone in a dimly red lit room weighed on me. Returning home to you continues to be the highlight of my day.

I also want to thank my family for their endless support and love. Mom, Dad, Jen – Thank you.

Throughout my graduate studies, I received help and guidance from so many lovely people. To Christine and Susanne of the Webber Lab, all the members of the Simmonds Lab, MacDonald Lab, Waskiewicz Lab, SASS, & MBSU, Arlene Oatway of the Microscopy Unit, Spencer Balay and the undergraduate students of the Hocking Lab: Thanks to each and every one of you.

TABLE OF CONTENTS

LIST OF TABLES

LIST OF FIGURES

LIST OF ABBREVIATIONS

APB	2-amino-phosphonobutyric acid
BCA	bicinchoninic acid
bp	base pair
$cd\cdot s/m^2$	candela second/square metre
cDNA	complementary DNA
CDSRR	cone dystrophy with supernormal rod response
cGMP	cyclic GMP
CNG	cyclic nucleotide-gated channel
CRISPR	clustered regularly interspaced short palindromic repeats
C_t	cycle threshold
DNA	deoxyribonucleic acid
dNTP	nucleoside triphosphate
dpf	days post-fertilization
DSB	double-stranded break
EDTA	ethylenediaminetetraacetic acid
ELISA	enzyme-linked immunosorbent assay
ER	endoplasmic reticulum
ERG	electroretinogram
FAF	fundus autofluorescence
ffERG	full-field ERG
GABA	gamma-aminobutyric acid
gDNA	genomic DNA
GFP	green fluorescent protein
GMP	guanosine monophosphate
GPCR	G protein-coupled receptor
gRNA	guide RNA
H&E	hematoxylin & eosin
HCN	hyperpolarization-activated cation channel
HRM	high resolution melt
INL	inner nuclear layer
IPL	inner plexiform layer
ipRGC	intrinsically photosensitive retinal ganglion cell
IS	inner segment
ISCEV	International Society for Clinical Electrophysiology of Vision

LB	Luria-Bertani
MBSU	Molecular Biology Service Unit
mpf	months post-fertilization
mRNA	messenger RNA
NAB	N-terminal A and B binding
nt	nucleotide
OCT	optical coherence tomography
OLM	outer limiting membrane
ONL	outer nuclear layer
OPL	outer plexiform layer
OP	oscillatory potential
PAM	protospacer adjacent motif
PBS	phosphate-buffered saline
PBST	PBS-tris
PCR	polymerase chain reaction
PDE	phosphodiesterase
PR	photoreceptor
qPCR	quantitative PCR
RFLP	restriction fragment length polymorphism
RIPA	radioimmunoprecipitation assay
RNA	ribonucleic acid
RPE	retinal pigmented epithelium
SB	sodium borate
SD	standard deviation
SEM	standard error
sgRNA	single guide RNA
ssDNA	single stranded DNA
TBOA	threo-β-benzyloxyaspartic acid
TL	Tüpfel long-fin
TM	transmembrane
TMS	tricane mesylate
TOPO	topoisomerase
TUNEL	terminal deoxynucleotidyl transferase dUTP nick end labeling

CHAPTER 1: INTRODUCTION

1.1 Anatomy of the Human Eye

1.1.1 Overview

The ability of our eyes to detect light and form high-acuity visual images depends on the precise formation and arrangement of multiple unique cell populations. Vision is undoubtably one of the most important senses and often the primary means by which organisms interact with their environment, whether used to navigate during travel, forage for food, or to perceive social cues from a friend or foe. The advantages of vision have resulted in the evolution of light-detecting structures numerous times throughout history, leading to several optically distinct means of producing images (Fernald, 1997). In humans, the primary cells responsible for detecting and transmitting light cannot regenerate, and therefore cell and tissue damage in the eye can lead to life-long vision loss. Genetic abnormalities, both inherited and sporadic, are capable of disrupting or even depleting visual function. The focus of this thesis is a rare form of retinal dystrophy termed *KCNV2* retinopathy. While the function of the $K_V8.2$ in regulating photovoltage in individual photoreceptors is known from previous electrophysiology studies (Beech & Barnes, 1989; Czirják et al., 2007; Gayet-Primo et al., 2018; Smith et al., 2012), the retinal disease process that occurs following loss of $K_V8.2$ is not well understood.

1.1.2 General Anatomy

Located anteriorly within the two orbits of the skull, human eyes are positioned to receive binocular visual information from the surrounding environment. The primary purpose of the eye is to capture photons and generate a neural response which can be transmitted as visual information to the brain. The eye is an exceedingly complex organ that utilizes each component of its anatomy to fulfill its physiological role of sight.

The adult eye is roughly spherical, measuring approximately 2.5 cm in diameter (Forrester et al., 2016). The eye can be divided into two distinct regions: the smaller *anterior segment* filled with aqueous humor and the larger *posterior segment* filled with vitreous humor (Figure 1.1). Separating the two segments is the transparent and flexible lens that fine tunes the focus of incoming light. The globe of the eye consists of three distinct layers: the *fibrous tunic*, the *uveal tract*, and the *retina*, which work together to focus incoming light and generate a photoresponse to be sent to the visual processing centres of the brain.

The outermost layer, the fibrous tunic, is mostly made up of connective tissue and comprises the anterior *cornea* and posterior *sclera*. The cornea is a transparent, multilayered tissue positioned on the anterior pole of the globe (DelMonte & Kim, 2011). It has slightly more curvature than the sclera and provides passage and coarse focus for light entering the eye. The sclera envelopes the remainder of the globe, maintaining its spherical shape and providing a sturdy barrier that separates the ocular contents from the surrounding environment (Forrester et al., 2016). The cornea and the sclera work together to form a sheath around the globe, protecting it from infection and injury.

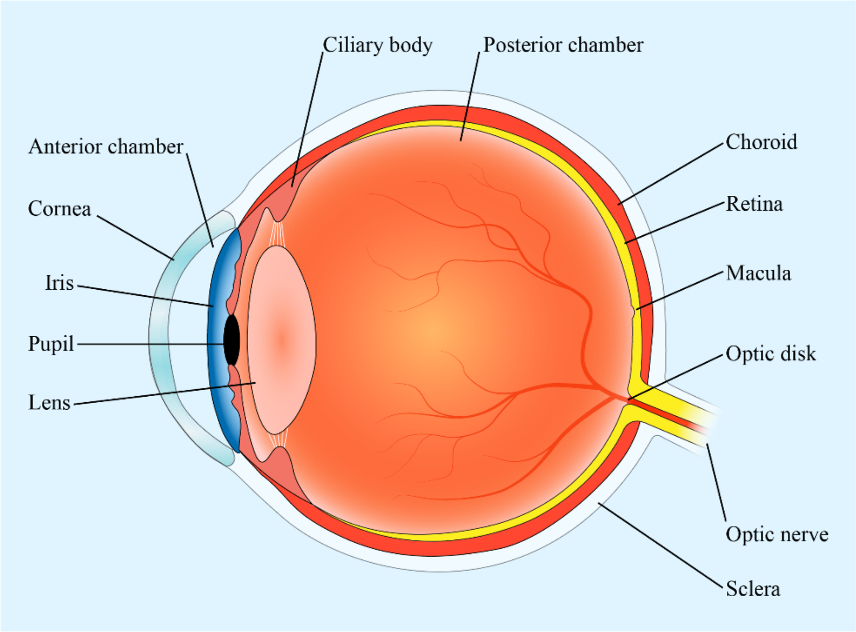

Figure 1.1 – The human eye is a complex sensory organ with many distinct tissues and structures.

The uveal tract is the middle tissue layer surrounding the globe and contains structures such as the *iris* and the *ciliary body*, as well as the *choroidal vasculature*. The iris is a thin, discoidal structure on the anterior pole of the eye. The iris is best known for its pigmentation that denotes an individual's eye colour, but it also contains a set of opposing muscles that work to control the size of the central opening, the *pupil.* Like the diaphragm of a camera, the iris responds to environmental luminosity and contracts or dilates to control the amount of light entering the eye. Surrounding the lens is the ciliary body, a ring of tissue that contains muscles used to manipulate the shape of the lens and change its refractive index through a process called accommodation. Additionally, the ciliary body replenishes the continually draining aqueous humor and ensures the shape and refractive index of the anterior chamber is maintained (Murgatroyd & Bembridge, 2008). Finally, the choroid is a multilayered vascular tissue that supplies blood to the tissues of the uveal tract and neural tunic. It nourishes the retina and plays an important role in preventing reflection of photons that are not detected by the retina (Forrester et al., 2016). The choroidal vasculature can be identified through optical coherence tomography (OCT), a technique that was utilized in this work and will be discussed in detail later in the thesis. Collectively, the uveal tract exerts control over the intensity of light within the eye and provides sustenance to the neurosensory retina.

1.1.3 Anatomy of the Retinal Layers

The innermost tissue layer of the eye, the retina, is a complex tissue made of several laminated cellular populations. The retina is organized into two distinct sublayers: the inner neurosensory retina and the outer retinal pigmented epithelium (RPE). Broadly speaking, the neurosensory retina is responsible for transducing incoming light into a photoresponse, processing visual information, and transmitting the photoresponse out of the eye towards the visual cortex. Distinct cell strata exist throughout the thickness of the neurosensory retina: the outer nuclear layer, populated by rods and cone photoreceptors; the inner nuclear layer, containing horizontal, bipolar, amacrine, and Müller glial cells; and finally the ganglion cell layer, composed of retinal ganglion cells (Figure 1.2). Most distal, the RPE forms a single cell layer with several critical supporting functions such as metabolite recycling and regulation of substance transmission into and out of the eye (Strauss, 2005). Each of these highly organized cellular populations will be detailed in the following subsections.

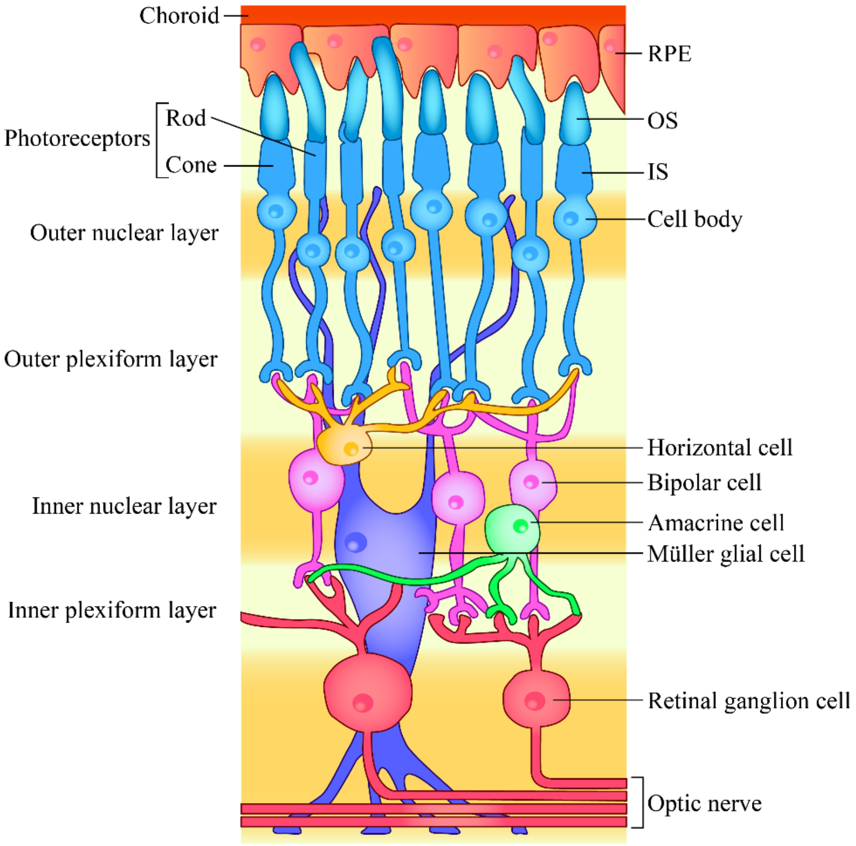

Figure 1.2 – The retina contains many cell populations organized into several laminated layers.

1.1.3.1 Photoreceptors

Photoreceptors are the primary light-detecting cells of the retina. There are two broad subtypes of photoreceptors in the vertebrate eye: rods and cones. Rods are highly sensitive cells that primarily detect contrast and brightness under low-light conditions, while cones are responsible for high-acuity colour vision. Cones are outnumbered in the human eye with approximately 115 million rods to 6.5 million cones, though their distribution in the retina designates a cone-dominated central region called the macula (Forrester et al., 2016). Although photoreceptor subtypes are distinct, their general morphology and function is comparable.

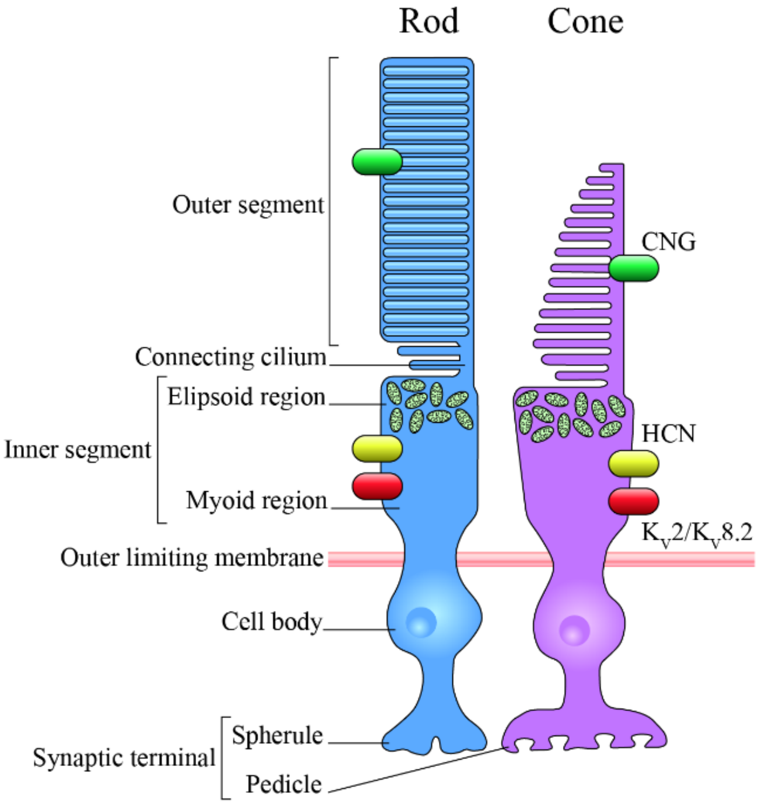

Figure 1.3 – Rod and cone photoreceptors are the primary light-detecting cells of the retina. Rods and cones share many structural features including an inner and outer segment, cell body, synaptic terminal, and a mosaic of membrane bound ion channels. CNG, cyclic nucleotide-gated ion channel; HCN, hyperpolarization-activated cyclic nucleotide-gated ion channel.

Morphologically, photoreceptors are complex, highly organized, polarized cells (Figure 1.3). Both subtypes have an *inner* and *outer segment* that are easily identifiable on retinal cross sections (Figure 1.2). The outer segment is a modified cilium that extends apically and is densely packed with stacked membranous discs containing the components necessary for phototransduction. In a process of ongoing renewal, these discs are generated basally and shed distally where they are phagocytosed by the RPE. The outer segment is connected to the inner segment by a thin connecting cilium that shuttles lipids, metabolites, and proteins between the two segments as needed. The distal portion of the inner segment, the *ellipsoid region*, contains the basal body of the connecting cilium and is densely packed with mitochondria. The proximal portion of the inner segment, the *myoid region*, contains a selection of organelles including the Golgi apparatus, smooth endoplasmic reticulum, and microtubules. The *outer limiting membrane* (OLM) is a network of cell adhesion junctions connecting photoreceptors to the apical processes of Müller glia (see Section 1.1.3.4) and providing both structural integrity and selective permeability to the retina (Omri et al., 2010). Collectively, the OLM marks the transition between the inner segment and the photoreceptor cell body. Photoreceptor nuclei occupy the *cell body*, or soma, and grossly form the *outer nuclear layer* in retinal cross sections (Figure 1.2). Short photoreceptor axons travel basally from the cell body and synapse with downstream bipolar cells and horizontal cells in the *outer plexiform layer*.

The cell membranes of photoreceptors are studded with ion channels. Many of the channels contribute to maintaining a resting state membrane potential through an ionic flow called *dark current*, while others work to shape the electrical response to light. These channels are spatially distributed throughout the photoreceptor with some being found exclusively on the outer or inner segment membrane. The nature of many of these channels will be discussed in detail in Section 1.2. The photoreceptor ion channels work in concert to elicit a controlled and precise chain of events that are essential for generation, transmission, and shaping of the photoresponse. The role of tightly regulated ion flux across the photoreceptor membrane is critically important, as dysfunction in any of these ion channels can lead to severe visual deficits.

Rods are highly sensitive photoreceptors specialized for dark vision. As their name suggests, these cells feature a long, cylindrical outer segment that sheathes hundreds of membranous discs. Light-sensitive G protein-coupled receptors called photopigments are contained within rod disks and play a critical role in the generation of photoresponses, as will be discussed in Section 1.2 (Park, 2019). Specific to rods, the photopigment *rhodopsin* is sensitive to blue-green wavelengths of light and enables detection of single photons. A consequence of this heightened sensitivity is the tendency for systematic saturation under bright lighting conditions.

Rods have specialized synaptic terminals known as *spherules* (Forrester et al., 2016). Bipolar and horizonal cell processes penetrate and embed within the spherule forming an intimate connection between the cells. *Synaptic ribbons* within the rod spherule feed pre-loaded vesicles containing the neurotransmitter glutamate into the synapse to mediate intercellular communication. Up to five processes can associate with a single rod spherule providing amplification of the visual signal.

Cone photoreceptors owe their name to their tapered outer segment morphology. Cone outer segment discs are continuous with the plasma membrane as opposed to the sheathed rod discs. The human retina contains three subtypes of cones: red, green, and blue. The outer segment of each subtype contains photopigments sensitive to their respective wavelengths of light (Mannu, 2014), designating human vision as *trichromatic*. Together, cone subtypes confer the ability to distinguish between wavelengths of incoming visual information, manifesting as colour vision. In addition to the broad visual spectrum sensitivity, cones provide high-acuity vision in a central retinal region known call the *fovea* (see Section 1.1.4). Cones create well-resolved neural input and define the highest quality sight within the visual field.

Cones have specialized synaptic terminals called *pedicles* that are pyramidal in shape and broader than rod spherules. The cone pedicle can harbour up to 12 interactions with neighboring cells, each of which is made up of three distinct connections referred to as a *triad*. The central triad connection is made with a downstream bipolar cell dendrite, while the outer two are made with horizontal cells. As in rod spherules, synaptic ribbons are also present in cone pedicles and control the release of the neurotransmitter glutamate to downstream cells. The synaptic connections between photoreceptors and downstream cells represent the *outer plexiform layer* (OPL) on retinal cross sections (Figure 1.2).

1.1.3.2 Retinal Interneurons

Photoreceptor cells synapse with retinal interneurons to form the first cellular junction in the transmission path of visual information. Nuclei of retinal interneurons, collectively and with nuclei of Müller glia, form the *inner nuclear layer* (INL; Figure 1.2). The most distal population of interneurons, *horizontal cells*, are situated alongside the OPL and work laterally in the retina by establishing connections between the photoreceptors. By integrating and regulating photoreceptor signalling, horizontal cells underlie the contrast-generating process of lateral inhibition in the retina (Chaya et al., 2017). Briefly, lateral inhibition creates contrast in the visual field by dampening the photoresponse signal transmission of circuits neighbouring an activated photoreceptor. Horizonal cells mediate lateral inhibition through the controlled release of the inhibitory neurotransmitter GABA to the photoreceptor synaptic terminals lateral to the stimulated photoreceptor (Baylor et al., 1971).

Bipolar cells have a central soma with two processes, one extended apically and one extended basally. Their nuclei represent a large proportion of the *inner nuclear layer* of the retina (Forrester et al., 2016). Bipolar cells form synaptic connections with a variety of retinal cells, and the particular synaptic partners differ depending on the subtype of photoreceptor the bipolar cell is servicing. Cone bipolar cells directly bridge between cone photoreceptors and downstream retinal ganglion cells (Seeliger et al., 2011). Alternatively, bipolar cells that synapse with rod photoreceptors transmit the photoresponse to amacrine cells that then carry the signal to ganglion cells (Seeliger et al., 2011). The number of photoreceptors that synapse with a single bipolar cell varies by retinal location. Generally, a single bipolar cell in the peripheral retina interacts with around 50-100 rods, whereas bipolar cells in the central retina can serve as a dedicated bridge between a single cone and retinal ganglion cell (Forrester et al., 2016; Schein, 1988). This devoted service to the central cones manifests as greater resolution in the central visual field relative to the peripheral field. Conversely, many rods sharing a single bipolar cell results in a greater receptive field and confers the heightened sensitivity for which the rod system is known.

Similar to horizontal cells, *amacrine cells* function laterally in the retina. Amacrine cells are situated at the proximal limit of the INL and synapse with bipolar cells and downstream retinal ganglion cells (Balasubramanian & Gan, 2014). There are many subtypes of amacrine cells, each with their own function and associated neurotransmitter. Though their precise roles remain enigmatic, amacrine cells are thought to perform a modulatory function for the photoresponse signal travelling to retinal ganglion cells (Marc et al., 2014).

1.1.3.3 Retinal Ganglion Cells

Synapsing with the bipolar and amacrine cells at the *inner plexiform layer* (IPL; Figure 1.2), the *retinal ganglion cells* are the final cell type in the path of photoresponse transmission within the eye. Almost all retinal ganglion cells function to carry the signal initiated by photoreceptors; however, a small subset of intrinsically photosensitive retinal ganglion cells (ipRGCs) has been identified. The photoresponse generated by ipRGCs is shuttled to the suprachiasmatic nuclei within the brain and plays a significant role in pupillary dilation and regulation of the circadian rhythm (Chen et al., 2011; Hattar et al., 2002). The axons of the approximately 1.2 million retinal ganglion cells across the human retina converge at the optic disk and exit the eye as a single bundle called the optic nerve (Forrester et al., 2016). The optic nerve is myelinated with oligodendrocytes that hasten action potential signal transmission to the visual processing centres of the brain (Magoon & Robb, 1981).

1.1.3.4 Müller Glia

Müller glia span nearly the entire apical-basal width of the neurosensory retina and, compared to microglia and astroglia, are the most abundant glial cell type within the eye (Reichenbach & Bringmann, 2013; Figure 1.2). Due to the widespread presence of Müller glia across the retinal layers, contact is made with each cell type. Müller glia have many roles within the retina, but generally support the metabolism and function of retinal neurons (Reichenbach & Bringmann, 2013). For example, Müller glia mediate cone-specific photoreceptor chromophore renewal through a process called the visual cycle (Morshedian et al., 2020; Wang & Kefalov, 2011; Ward et al., 2020). Chromophores are the components of photoreceptor photopigments that undergo conformational changes upon light absorption. Following this structural change, the chromophore cannot respond to light until it is returned to its original state. Through a series of chemical events, Müller glia recycle the spent *all-trans retinal* to its photosensitive *11-cis* state. The chromophore can then be returned to cone outer segments and reused for light detection within the photopigments (Wang & Kefalov, 2011). Additionally, Müller glia increase the speed of photoresponse transmission through rapid uptake of glutamate, the neurotransmitter released by photoreceptors (Matsui et al., 1999). For more information on glutamatergic neurotransmission in the retina, see Section 1.2.1. Müller glia have many more functions within the retina, including structural support, neurotransmitter recycling, and maintenance of the extracellular space (Reichenbach & Bringmann, 2013). The broad range of responsibilities

Müller glia have within the retina highlight the importance of these cells for maintaining visual function.

1.1.3.5 Retinal Pigmented Epithelium

The RPE is a pigmented cell layer just outside the neurosensory retina, situated between the choroid and photoreceptor outer segments. It is a monolayer of hexagonal epithelial cells that are densely packed with pigment granules. Although not a component of the neurosensory retina, the RPE is intimately associated with the underlying photoreceptor layer and is in fact derived from the same neuroepithelium during embryogenesis (Strauss, 2005). The RPE is not directly involved in the generation, processing, or transmission of the photoresponse; however, its many supportive functions make the RPE an important structure for vision. For example, the RPE contributes to keeping the extracellular space surrounding photoreceptors free of cellular debris by phagocytosing shed disks following outer segment renewal (Strauss, 2005). Additionally, the RPE is responsible for the entire visual cycle for rod photoreceptors through recycling of the all-*trans* retinal produced following bleaching of rhodopsin (Strauss, 2005; Weinstein et al., 1967). The visual cycle for cones is likely mediated by both Müller glia, as discussed above, and the RPE (Morshedian et al., 2020; Ward et al., 2020). Importantly, the RPE also forms an integral part of the outer blood-retina barrier and tightly regulates the passage of substances between the choroidal vasculature and retinal tissue (Runkle & Antonetti, 2011). Overall, the RPE plays important roles ensuring continual photoreceptor function and maintaining an optimal extracellular environment within the neural layers of the retina.

1.1.4 Topographic Anatomy of the Retina

Although the retina as a whole is given a unifying name, there is considerable cellular heterogeneity across the tissue. An understanding of retinal topography is important, as different regions of the tissue host unique cellular populations and layering patterns. Distinct components of visual function, such as colour vision or night vision, can therefore be delegated to specialized regions of the retina. Locations on the surface of the retina are measured relative to the focal point of incoming light and are illustrated in Figure 1.4. Anatomical descriptions of these regions for a human retina are as follows (Note that clinical terms can differ and are given in brackets):

1. The *central retina* (macula) is an approximately 5 mm diameter area of the retina centered on the focal point of incoming light. It is dominated by cone photoreceptor subtypes, though some rod photoreceptors also populate this area.
2. The *macula lutea* (fovea) is a smaller area within the central retina with a diameter of 1.5 mm. It appears yellow on colour fundus photographs due to carotenoid pigments present in the cone photoreceptor axons.
3. The *fovea* (foveola, foveal pit) has a 0.35 mm diameter and is centered on the macula. This region is a depression on the retina manifesting as an area of reduced thickness on anatomical cross-sections. The cellular population of the fovea is almost exclusively cone photoreceptors; however, a small number of Müller glia also occupy this region (Reichenbach & Bringmann, 2020). Rod photoreceptors are absent and downstream cell layers are displaced laterally, accounting for the reduced thickness of this region. The fovea is the target for focused light and is responsible for high-acuity colour vision.
4. The *optic disk* is positioned 3 mm medial to the fovea and has a diameter of 1.8 mm. This structure represents the egress point for the optic nerve leaving the retina and traveling towards the brain. Vasculature enters and exits the eye at this landmark.
5. The *peripheral retina* includes all portions of the retina outside of the central retina. Retinal thickness in the periphery between 110-140 µm. Rod photoreceptors make up the

primary photoreceptor subtype, though some isolated cones can be found in the peripheral retina.

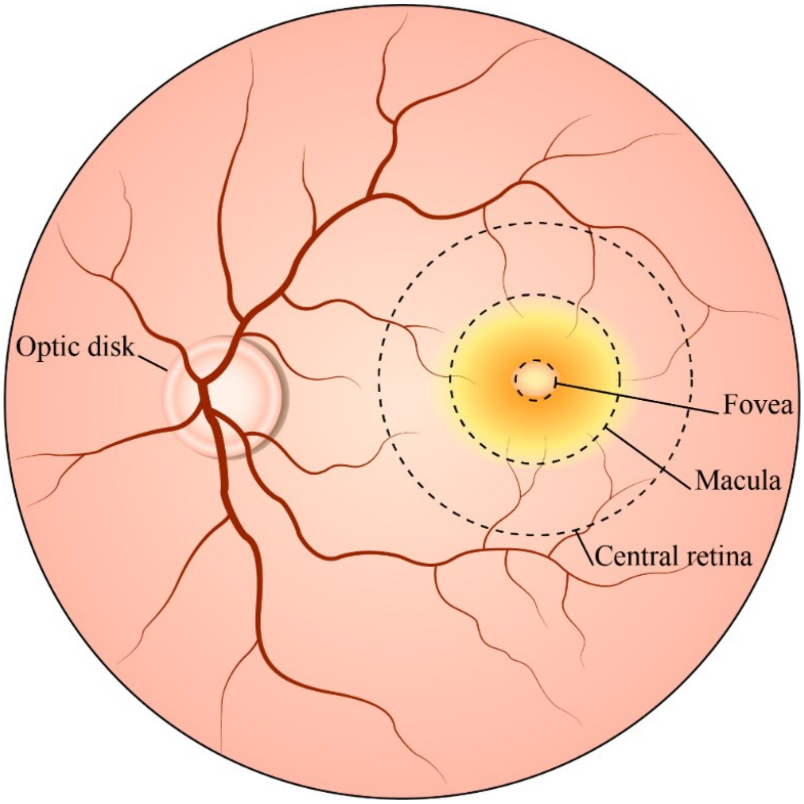

Figure 1.4 – Topographic anatomy of the inner surface of the retina (fundus). The inner surface of the eye opposite the pupil has distinct topographic coordinates. The rod-dominated peripheral retina, responsible for low light vision, lies outside of the central retina. The cone-rich macula surrounds the cone-only fovea that is responsible for high-acuity colour vision.

1.2 Retinal Physiology of Light Detection

The primary function of the retina is to capture and transduce incoming light energy into electrical impulses that can be transmitted to the brain. In order to understand how light initiates the photoresponse, it is critical to discuss what is happening within photoreceptors in the dark.

1.2.1 Dark Current

The resting membrane potential of human photoreceptors is not currently known; however, cellular recordings from other vertebrates can be used to estimate membrane potentials of human rods and cones. Resting membrane potentials of rods range between -30 to -45 mV in salamanders (Armstrong-Gold & Rieke, 2003; Bader et al., 1978; Baylor & Nunn, 1986; Beech & Barnes, 1989), -32 to -40 mV in frogs (Ogura et al., 2003), and register at -46 mV in macaque (Schneeweis & Schnapf, 1995). Cone photoreceptor resting membrane potentials are less studied, but were measured at -45 mV in salamanders (Attwell et al., 1982; Thoreson & Bryson, 2004), -35 mV in turtles (Baylor et al., 1971), and -46 mV in macaque (Schneeweis & Schnapf, 1995). Regardless of the exact resting membrane potential of human photoreceptors, rods and cones exhibit a static voltage range that is a more depolarized than is typical for neurons (~-65 mV (Lewis et al., 2011)).

The resting membrane potential of photoreceptors remains relatively stable in the dark; however, ionic flux at the cell membrane is far from static. While multiple channels conduct ions across the plasma membrane of photoreceptors, two channels primarily maintain the resting membrane potential: cyclic nucleotide gated (CNG) channels in the outer segment and heterotetrameric $K_V2.1/K_V8.2$ potassium channels in the inner segment (Barnes, 1994; Biel, 2009; Figure 1.3). CNG channels activated by bound cytoplasmic cGMP in the photoreceptor allow primarily Na^+, but also Ca^{2+}, to flow into the outer segment from the extracellular environment. Importantly, the positive current supplied by CNG channels is counteracted by heteromeric $K_V2.1/K_V8.2$ channels in the inner segment. $K_V2.1/K_V8.2$ voltage-gated potassium channels provide an approximately equal and opposite negative current through the efflux of K^+ into the extracellular environment (Beech & Barnes, 1989). The structure and function of

K_V2.1/K_V8.2 heteromeric channels will be discussed in detail in Section 1.4.4. In the absence of light, CNG and K_V2.1/K_V8.2 heteromeric channels work together to facilitate the dark current and maintain resting membrane potential.

The relatively positive resting state membrane potential maintained by the dark current causes sustained release of the neurotransmitter glutamate from the synaptic terminal of the photoreceptor (Nakanishi et al., 1998). To clarify, photoreceptors release neurotransmitter in dark environments and therefore are in constant communication with downstream bipolar cells prior to light exposure. Importantly, two opposing subtypes of bipolar cells exist in the human retina: ON and OFF bipolar cells (Werblin & Dowling, 1969). Glutamate released by photoreceptors in the dark binds to ionotropic receptors on downstream OFF bipolar cells resulting in activation of the OFF pathway of the retina (Nelson & Kolb, 2003). Conversely, glutamate released by photoreceptors actively inhibits ON bipolar cells through metabotropic receptors, keeping the ON pathway inactive in the dark (Nakanishi et al., 1998; Nelson & Kolb, 2003). The presence of both bipolar cell subtypes is important for two reasons: 1) facilitation of centre-surround visual processing that is critical for high-acuity vision (Nelson & Kolb, 2003), and 2) isolation of the cellular origins of the electroretinogram (see Section 1.3.1). Ultimately, when light strikes the photoreceptor, the glutamatergic inhibition of the ON visual system is ceased and the photoresponse can be propagated.

1.2.2 Phototransduction Cascade

The phototransduction cascade is a series of molecular events that takes place within photoreceptors upon the absorption of a photon (Figure 1.5). Before light strikes the photoreceptor, dark current is active and the chromophore 11-cis retinal is bound to an outer segment opsin within a disc membrane. Chromophore-opsin complexes are collectively referred to as photopigments, such as rhodopsin (Mannu, 2014). Rhodopsin, and all other transductive photopigments, are G protein-coupled receptors (GPCRs) that follow the canonical GPCR pathway (Park, 2019). The cascade begins with the absorption of a photon by the chromophore leading to photoisomerization into all-trans retinal (Kibelbek et al., 1991; Mannu, 2014). The conformational change causes retinal to dissociate from the opsin binding partner and diffuse out of the photoreceptor. Once in the extracellular space, retinal is taken up by either Müller glia or the RPE and recycled through the visual cycle (See Section 1.1.3; Strauss, 2005; Wang & Kefalov, 2011). Upon chromophore dissociation, the opsin assumes an activated form and associates with the heterotrimeric G protein *transducin* (Pepe, 1999). The interaction causes the α-subunit of transducin to dissociate from the remaining β- and γ-subunits and activate the membrane-bound *phosphodiesterase* (PDE; Pepe, 1999) As a result of PDE activity, cytoplasmic cGMP is hydrolysed to GMP, resulting in the closure of outer segment CNG channels (Van Hook et al., 2019). Importantly, closure of CNG channels leads to cessation of the inward component of dark current. The photoreceptor membrane potential hyperpolarizes following the reduction in sodium ion influx at the outer segment and the continued potassium ion efflux at the inner segment (Van Hook et al., 2019). Hyperpolarization of the photoreceptor leads to closure of voltage-gated calcium channels at the synaptic terminal, resulting in the stoppage of glutamate neurotransmitter release (Nakanishi et al., 1998). The negative drop in membrane potential triggers opening of a hyperpolarization-activated cyclic nucleotide-gated (HCN) ion channel that actively works to repolarize the photoreceptor back into its normal operating range (Barnes, 1994).

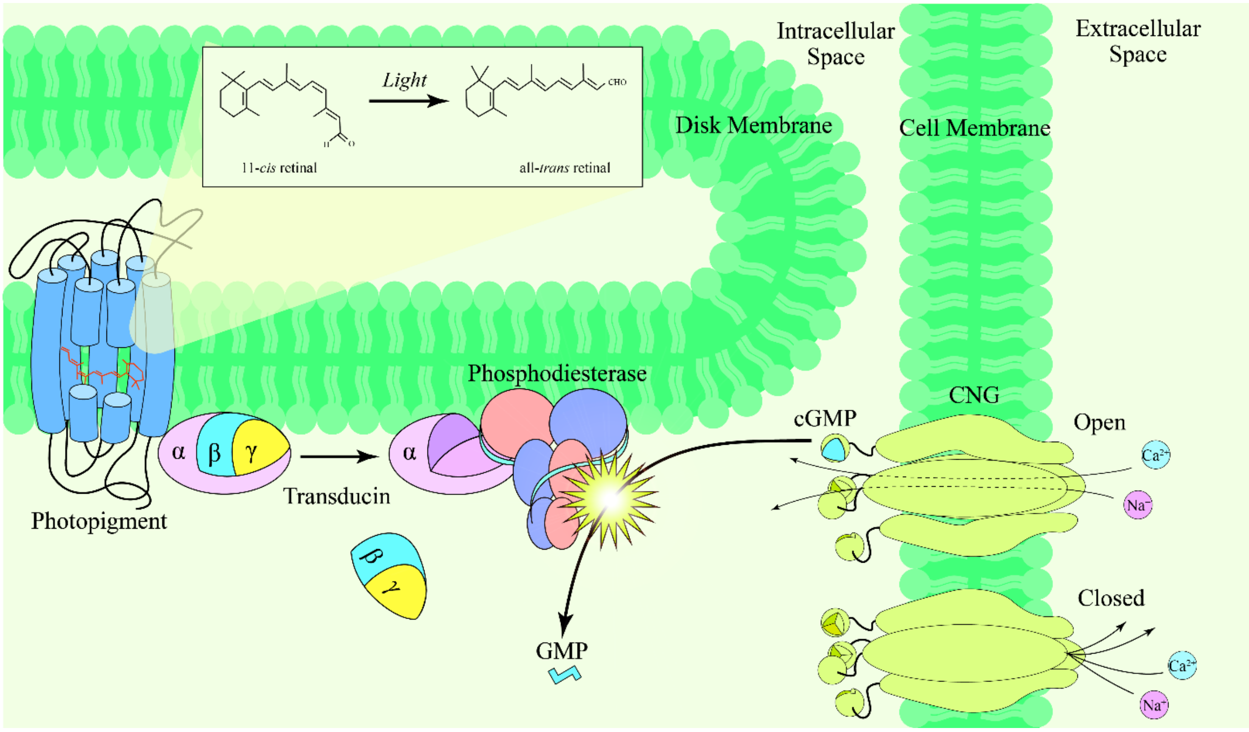

Figure 1.5 – The phototransduction cascade. Light detection by the chromophore 11-*cis* retinal initiates a chain of molecular events within the outer segments of photoreceptors. This pathway hydrolyses cGMP into GMP, altering the conductivity of the cell membrane cyclic nucleotide-gated (CNG) ion channel. In turn, the membrane potential of the photoreceptor hyperpolarizes, leading to the propagation of the photoresponse to downstream bipolar cells. This illustration takes place in a rod photoreceptor with internalized outer segment disks; however, the same physiological process occurs in cone outer segments.

1.2.3 Communication to the Visual Cortex

Cessation of glutamate release from photoreceptors reduces the inhibition on bipolar cells, allowing them to depolarize and communicate with downstream cells via neurotransmitter release. The photoresponse is transmitted through bipolar cells to downstream retinal ganglion cells that ultimately form the optic nerve. While retinal cell populations such as amacrine and horizontal cells process the photoresponse within the retina, the response is subject to further processing in the thalamus and visual cortex of the brain. The optic nerve propagates the photoresponse signal out of the eye at the optic disk where it travels to the visual processing centres of the brain (Forrester et al., 2016).

1.3 Measurements of Retinal Function

1.3.1 The Electroretinogram

The eye was not considered to be an electrically active organ until 1865 when the Swedish physician Frithiof Holmgren observed a reproducible voltage trace in amphibian eyes following a flash of light (Brown, 1967). The characteristic trace has since been termed the electroretinogram (ERG). Following this discovery, ERGs from a wide range of organisms, including humans, have been extensively studied. Various ERG protocols were developed to assess different features of the retinal response to light. For example, the ERG detected by Holmgren in 1865 and the method used in this thesis is the full-field ERG (ffERG). For the ffERG, the entire retina is flashed with light of uniform luminosity resulting is an electrical response spanning the entire retina. Alternatively, specific areas of the retina can be stimulated in the multi-focal ERG, giving a read out of the spatial functionality of the tissue. Disease states of the visual system can significantly alter the ERG waveform, making the ERG a standard tool in the clinical assessment of visual function.

The ffERG (hereinafter ERG) waveform presents as a classic sequence of peaks and valleys following the flash (Figure 1.6). Specifically, these sequential features have been designated in order as a-, b-, c-, and d-waves, each of which represent specific retinal cell populations. The first feature of the ERG is the negatively deflecting *a-wave* that is relatively small compared to the subsequent positive *b-wave*. The a-wave reflects photoreceptor hyperpolarization and cessation of the dark current following light detection (Sillman et al., 1969). As a result, alterations in the size, shape, or timing of the a-wave indicate deficiencies within the photoreceptor layer of the retina. Importantly, the initial slope of the a-wave represents events leading to photoreceptor hyperpolarization following CNG closure and does not indicate photoreceptor pathologies involving cell recovery or pre-synaptic signalling defects.

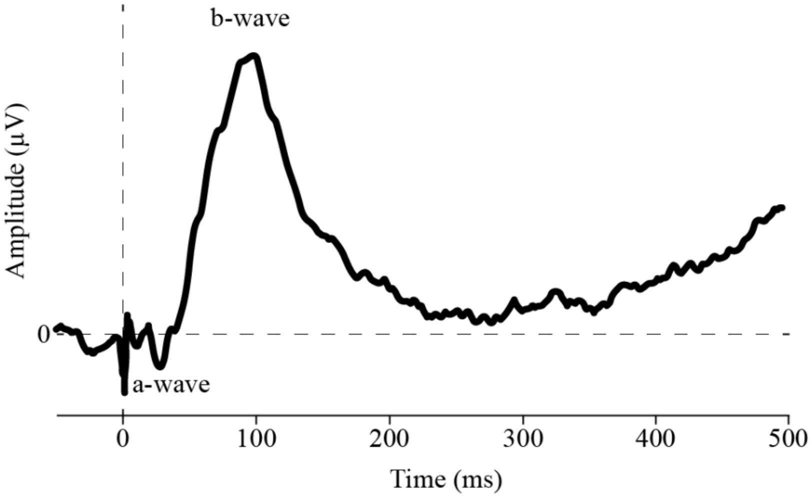

Figure 1.6 – The ERG waveform. This exemplary ERG trace illustrates the major wave components plotted against time (x-axis). The horizontal dashed line represents the baseline amplitude against which the a-wave amplitude is measured. The amplitude of the b-wave is measured from the trough of the a-wave to the peak of the b-wave. The vertical dashed line indicates the time of stimulus exposure and the start of the ERG waveform. Implicit times for both major waves are measured from t=0 to the time of the wave's trough/peak. The large negative deflecting spike at t=0 is a photovoltaic artefact. The c- and d-waves are not pictured, as they occur at timepoints greater than 500 ms. Oscillatory potentials (OPs) can be seen as small ripples on the ascending arm of the b-wave.

The most prominent feature of the ERG is the large, positively deflecting b-wave. The b-wave has long been known to represent cellular activity downstream of photoreceptors owing to its disappearance following pharmacological intervention that blocks photoreceptor synaptic transmission (Pepperberg & Masland, 1978; Sillman et al., 1969). Studies investigating the ERG and potassium flux at different retinal depths concluded that the b-wave primarily represented ON bipolar cell depolarization (Dick & Miller, 1985). Oscillatory potentials (OPs) are high frequency ripples on the ascending arm of the b-wave and are thought signify aspects of photoreceptor and interneuron activity (Dai et al., 2017), though their precise physiology remains unclear. Late components of the ERG like the c- and d-waves result from RPE and OFF bipolar cell activity, respectively (Steinberg et al., 1970; Xu & Karwoski, 1995). The ERG is a complicated waveform that represents the summation of electrical activity within the retina. For this reason, the ERG is a powerful diagnostic tool for identifying the cellular basis of many ocular diseases.

The shape of the ERG waveform is affected by many factors that can be manipulated in an experimental setting to separate the functional integrity of rod and cone systems. These factors include the light adaptation level of the retina and the intensity and frequency of light stimuli. Owing to their differential physiology, rod and cone photoreceptors respond to changes in these factors in a characteristic fashion. There are two states of light adaptation: scotopic (dark-adapted) and photopic (light-adapted). In a scotopic environment, all photoreceptors are able to respond to light. Conversely, in a photopic environment, rod photoreceptors are saturated and only cones can contribute to the ERG. Photoresponses from the very sensitive rods can be isolated in a scotopic environment using dim flashes that are too weak to stimulate cone photoreceptors (McCulloch et al., 2015). Cone-driven responses begin to dominate the ERG waveform as stimulus intensity increases, i.e., the ERG transitions from a rod-driven response at dim intensities to a mixed response at medium intensities and finally to a cone-driven response at high intensities (McCulloch et al., 2015). Stimulus frequency can also be increased above 25 Hz to exploit the high-refresh rate of the cone system, resulting in a cone-only response (McCulloch et al., 2015). These fundamental differences between photoreceptor ERG responses enable clinicians and scientists to carefully manipulate experimental conditions to further break down the functional output of the retina.

ERGs are primarily quantified through two parameters: amplitude and implicit time (McCulloch et al., 2015). The amplitude of the a-wave is measured from the baseline to the trough of the a-wave. The b-wave amplitude is measured from the trough of the a-wave to the peak of the b-wave. Implicit time, or time-to-peak, is the duration of time between the stimulus (vertical dashed line in Figure 1.6) and the trough or peak of the wave being measured. Alterations in wave amplitude or implicit time are common indications of retinal dysfunction and therefore have become standard quantifications of the ERG waveform.

1.3.2 Whole Cell Patch Clamp Electrophysiology

Whole cell patch clamp electrophysiology has been essential in the investigation of retinal cell physiology in response to light. Patch clamp techniques gather electrical information from individual cells, unlike the mass retinal response recorded in an ERG. Although this methodology was not used in the experiments reported in this thesis, whole cell recordings of rods and cones informed much of the current understanding of ion flux at the photoreceptor membrane.

Whole cell recordings utilize a glass micropipette suction electrode able to gain access to the intracellular environment by applying negative pressure to the cell membrane. The tensile forces caused by suction produce a rupture in the membrane, establishing a tight seal between the micropipette and membrane. The electrode housed within the micropipette is in direct contact with the intracellular environment and can detect changes to the electrical environment within the cell (Segev et al., 2016). There are two main variations that are critical to assess electrical properties cell populations: the voltage clamp and the current clamp. In voltage clamp experiments, the micropipette serves as conduit to manipulate the membrane potential while simultaneously recording changes to cellular current. Conversely, current clamp experiments inject currents into the cell and record changes in membrane voltage. These approaches are often used in conjunction to establish the electrophysiologic properties of cells and their associated ion channels.

1.4 Potassium Channels

1.4.1 Overview

Ion channels are protein structures that facilitate the movement of charged atoms across the normally impermeable cell membrane. Cellular processes often require the highly controlled movement of many different ions, so channels have evolved to specialize in the transport of certain ionic species. An excellent example of this phenomenon is the flux of potassium ions across cell membranes through dedicated oligomeric channels. From proliferation to nerve conduction to apoptosis, potassium channels serve numerous functions throughout living systems. Potassium channels are assembled from either two or four α-subunits that interact with each other to form a potassium selective pore. An exemplary potassium channel subunit is illustrated in Figure 1.7. The enormous sphere of influence these channels have on the body is reflected in the wide range of genetic variation their subunits possess.

All potassium channels regulate the movement of a common ion; however, gross functional and morphological differences have resulted in the designation of four distinct channel families. These families are defined by molecular features of their subunits, namely the number of transmembrane (TM) and pore (P) domains, the total number of subunits in the holochannel, and the possession of family-specific sensors (Capera et al., 2019). First, the inward rectifier potassium channels, K_{ir}, are formed by four 2TM/1P subunits and are generally responsible for potassium influx (Hibino et al., 2010). Second is the simplest channel family, K_{2P}, formed by the dimerization of two 4TM/2P subunits to create constitutively open or ‘leaky’ channels (Enyedi & Czirják, 2010). Third, calcium-activated potassium channels, K_{Ca}, are generated through the assembly of four 6TM/1P subunits, each with a ‘calcium-bowl’ sensor unique to the family (Capera et al., 2019; Vergara et al., 1998). The focus of this thesis revolves around the fourth and final family: the voltage-gated potassium channels, K_V. Voltage-gated potassium channels are formed by the tetramerization of four 6TM/1P subunits (Kim & Nimigean, 2016), similar to K_{Ca} assemblies. K_V channel subunits possess a potassium-selectivity sensor in addition to a voltage sensor (Heginbotham et al., 1994; Long et al., 2005). As a result of the diversity of potassium channels, each family inhabits a functional niche dictated by the nature of their structure.

While the presence of environmental sensors varies alongside the numbers of transmembrane and pore domains between families, the composition of the potassium-selective pore does not. The pore, a feature of all four families, permits the movement of potassium ions across the cell membrane while simultaneously selecting against other small, positively charged ions like sodium (Doyle et al., 1998). The pore is formed through the quaternary structure of the oligomerized subunits, each of which possesses an individual pore domain (Hibino et al., 2010). A defining feature of the pore is the conserved amino acid sequence, GYG, that has been identified as the common selectivity filter of potassium channels (Heginbotham et al., 1994). Through this selectivity filter, potassium ions are conducted at a rate close to diffusion, while other monovalent cations like sodium have no measurable conductance (Doyle et al., 1998). The potassium-selective pore represents a shared feature of all potassium channel families and helps specialize these highly selective and conductive channels.

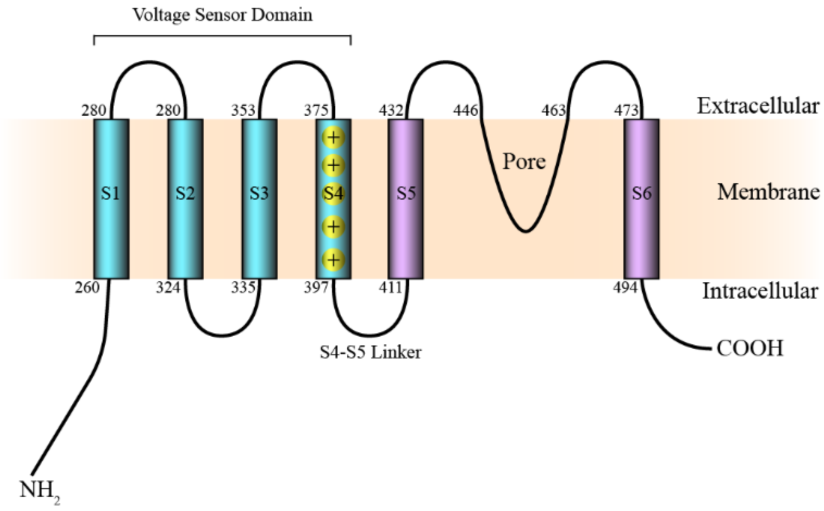

Figure 1.7 – The general structure of a voltage-gated potassium channel subunit. Diagram of human $K_V8.2$ with the amino acid residue locations of each transmembrane domain. The voltage sensor domain encompasses S1-S4, with S4 containing charged residues that interact with changing electrical fields.

1.4.2 Voltage-gated Potassium Channels

The regulatory domain of potassium channels is the main source of diversity between the four families. Each channel family, with the exception of the simple K_{2P}, has a unique regulatory domain able to sense different environmental stimuli. Within the K_V family, the regulatory domain is defined by a *voltage sensor* that spans the first four TM domains (Figure 1.7). Once folded, the voltage sensor establishes a chemical linkage with the pore domain (Long et al., 2005). When the voltage sensor domain detects changes in the membrane potential, charged amino acids initiate a conformational change that pulls the pore domain open (Long et al., 2005). The straightforward mechanism of voltage-gated pore dynamics creates a connection between membrane potential and potassium conductance. The ability to sense and subsequently alter membrane potential places voltage-gated potassium channels perfectly within the biological niche of excitable cells.

1.4.3 Currents of the Photoreceptor Inner Segment

Although closure of the CNG channels determines the photocurrent response to light, the resulting photovoltage change is significantly modified by currents of the inner segment. As the mediator of synaptic release of glutamate, photovoltage is the more direct regulator of visual perception. The primary inner segment currents responsible for shaping the photovoltage are I_h and I_{kx}, carried by HCN1 and Kv2/Kv8.2 channels, respectively.

In the photoreceptor inner segment, HCN1 channels produce a delayed inward current (influx), I_h, following hyperpolarization of the membrane potential (Barnes, 1994; Bruening-Wright & Larsson, 2007; Seeliger et al., 2011). HCN channels are voltage-gated non-specific cation channels that mediate the inward current of both sodium and potassium ions at a ratio that depends on ion concentrations but was estimated at 0.4 for mouse cones (Ingram et al., 2020). I_h is activated at photoreceptor membrane potentials negative to -55 mV (Figure 1.8; Barnes, 1994; Biel et al., 2009), which is close to the resting membrane potential of many other cells in the body (Biel et al., 2009; Lewis et al., 2011; Sperelakis, 2011). Most ion channels are activated by membrane depolarization, which explains why the hyperpolarization-activated I_h was initially termed a “funny” or “queer” current when identified in heart tissue (Brown et al., 1979) and neurons (Halliwell & Adams, 1982), respectively. Unlike cardiac and neural tissues, photoreceptors maintain a relatively depolarized resting membrane potential of ~-40 mV (Barnes, 1994). Due to the discrepancy between the activation range of I_h and the resting membrane potential of photoreceptors, it is unlikely to contribute to the maintenance of the standing membrane voltage. By one estimate, only 44 out of ~2000 HCN1 channels would be open in a dark-adapted salamander rod, while 1430 would be open following a bright light stimulus (Barrow & Wu, 2009b). Photoreceptors respond to light by hyperpolarizing, so the function of the inward current generated by I_h instead works to actively return the cell voltage of photoreceptors back to within a normal operating range following light detection. Therefore, the role of I_h is redefined in the context of the photoreceptor to serve as a major regulator of the photoresponse timing and shape (Barnes, 1994).

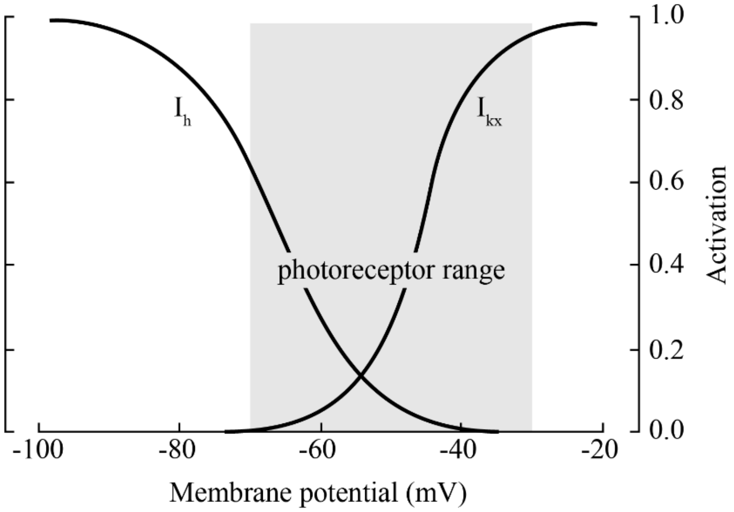

Figure 1.8 – Activation curves of I_h and I_{kx}. Range of activation of ion currents within the photoreceptor inner segment, I_h and I_{kx}, mediated by HCN and Kv8.2/Kv2 heteromeric channels, respectively. Both currents operate within the physiological voltage range of photoreceptors and

play critical roles in tightly regulating changes to membrane potential. Adapted from Barnes (1994) with permission under licence number 4907141260031.

Given the relatively depolarized resting voltage of photoreceptors, an ion current other than I_h must be responsible for the maintenance of the standing membrane potential. The outward potassium current (efflux) dubbed I_{kx} was first suggested by Beech and Barnes (1989) to have an essential role in setting the resting membrane potential of photoreceptors. Beech and Barnes suggested that I_{kx} acted as an equal and opposite ionic flux to that of the inward dark current generated by the outer segment channel CNG (see Section 1.2.1; Beech & Barnes, 1989). Therefore, it is the coordinated effort of an inward current through the outer segment channel CNG and a balancing outward I_{kx} current though an inner segment channel that is responsible for establishing the resting membrane potential of photoreceptors. The channel responsible for I_{kx} was only recently identified as a heteromeric $K_V2/K_V8.2$ voltage-gated potassium channel (Gayet-Primo et al., 2018). A detailed description of the discovery and kinetics of this channel will be discussed in the next section.

Unlike I_h, $K_V2/K_V8.2$-mediated potassium ion flux is in the opposite, outward direction and activates at potentials positive to -70 mV (Figure 1.8; Barnes, 1994; Fan & Yazulla, 1997). Blockade of I_h and I_{kx} in isolated salamander photoreceptors allowed further functional differences between the two to be teased apart (Beech & Barnes, 1989). Hyperpolarizing currents mimicking dim and bright stimuli were injected into the photoreceptors while their voltage response was monitored. Application of cesium, a selective blocker of I_h, resulted in a normal photoresponse to dim stimuli injection, but a slow and sustained hyperpolarization in response to bright stimuli injection. Similarly, the photoresponse to dim light current injection was large and passive when the photoreceptors were bathed in both cesium and barium, a blocker of I_{kx} (Beech

& Barnes, 1989). Therefore, these two ion currents are complementary and function to accelerate the photoreceptor response to differing stimulus intensities. In other words, I_{kx}, in addition to setting the resting membrane potential, is responsible for accelerating the recovery from small hyperpolarizing photoresponses following dim stimuli. Notably, I_{kx}-mediated shaping of photovoltage occurs through closure of voltage-gated potassium channels following hyperpolarization in response to a light stimulus, with a resulting reduction in outward current flow. In contrast, photoreceptor hyperpolarization following bright stimuli is recovered through increased inward current (I_h) flow via opening of HCN channels (Beech & Barnes, 1989). Although these two currents have different activation ranges and current directions, they work closely with each other to rapidly shape the voltage recovery following a light stimulus. The high degree of control over the photoresponse by I_h and I_{kx} are an important factor in providing high temporal resolution to vision.

1.4.4 $K_V2/K_V8.2$ Heteromeric Channels

Although the presence and functional properties of I_{kx} had been known since 1989 (Beech & Barnes, 1989), the identity of the channel mediating this potassium flux was not confirmed until almost 30 years later. A heterotetrameric voltage-gated potassium channel consisting of three K_V2 subunits and one $K_V8.2$ subunit had striking similarities in location and functional properties to I_{kx} (Gayet-Primo et al., 2018). Specifically, $K_V2/K_V8.2$ channels were primarily localized to the photoreceptor inner segments of mouse, macaque, and human retinae. Further, $K_V2/K_V8.2$ channels in macaque were found to be barium-sensitive and facilitated a sustained outward current when photoreceptors were voltage clamped to the dark resting membrane potential. As the voltage clamp was stepped down to hyperpolarize the cell, $K_V2/K_V8.2$ channels slowly developed an inward current (less efflux) that had a reversal potential near that of I_{kx}

(Gayet-Primo et al., 2018). These data strongly indicate that the molecular identity of the I_{kx} potassium current in photoreceptors is the heteromeric K_V2/K_V8.2 channel.

The subunit composition of 3:1 heterotetrameric K_V2/K_V8.2 channels is of interest in the context of the photoreceptor. All four subunits are members of the voltage-gated potassium channel family; however, there are fundamental differences between K_V2 and K_V8.2 subunits. While K_V2 is expressed throughout the body and able to form functional homomers with other K_V2 subunits, the same is not true for K_V8.2 (Ottschytsch et al., 2002). Homomers of four K_V8.2 subunits are successfully formed in the endoplasmic reticulum (ER), but are deemed as *electrically silent* owing to their inability to be trafficked to the cell membrane (Ottschytsch et al., 2002). Instead, single K_V8.2 subunits leave the ER and reach the cell membrane through compulsory assembly with other subunits, such as the promiscuous K_V2 (Ottschytsch et al., 2002; Smith et al., 2012).

Homomeric and heteromeric assembly is mediated by the NAB domain located near the amino terminus of voltage-gated potassium channel subunit proteins (Yu et al., 1996). Interestingly, the inclusion of K_V8.2 in K_V2 channels modifies the kinetics of potassium flux (Czirják et al., 2007; Ottschytsch et al., 2002; Smith et al., 2012). As a result, the term *silent modifier subunit* has been used to refer to K_V8.2 and similar subunits that cannot form functional homomers. In the context of K_V2/K_V8.2 channels, K_V8.2 modulates the K_V2 homomeric kinetics in several important ways.

First, the K_V2/K_V8.2 heteromeric channels inactivated slower in depolarized environments than K_V8.2 homomers in *Xenopus* oocytes (Czirják et al., 2007) and HEK293 cells (Smith et al., 2012). In fact, K_V2/K_V8.2 heteromeric channels did not ever fully inactivate in HEK293 cells (Smith et al., 2012). These same studies also identified a faster rate of recovery from an inactivated state compared to KV2 homomers (Czirják et al., 2007; Smith et al., 2012). Furthermore, KV2 homomers were unable to sustain an outward current, a defining feature of I_{kx}, due to a heightened susceptibility for inactivation (Czirják et al., 2007). Altered inactivation and recovery kinetics of KV2/KV8.2 heteromeric channels relative to KV2 homomers permit efficient sustained potassium efflux in depolarized environments, a function that is not supported by KV2 homomers.

Additionally, inclusion of KV8.2 silent subunits modulated the voltage range of activation compared to KV2 homomers. Specifically, the activation curve of KV2/KV8.2 heteromeric channels was shifted to more negative potentials than KV2 homomers in *Xenopus* oocytes (Czirják et al., 2007). The shift allows KV2/KV8.2 heteromeric channels to activate at -40 mV (Czirják et al., 2007), within the normal -30 to -70 mV operating range of photoreceptors (Werblin, 1975). Conversely, KV2 homomeric channels do not activate at membrane potentials negative of -20 mV (Frech et al., 1989), making their contribution to photoreceptor physiology questionable. These studies highlighted the influence of the KV8.2 silent modifier on KV2.

Finally, KV2/KV8.2 heteromers amplify transient hyperpolarizations of the cell, a feature remarkably similar to the photoreceptor response to sudden light onset (Czirják et al., 2007). The amplification occurs because of the sustained outward current mediated by Kv2/Kv8.2 at rest, which is not present with Kv2 alone, and a delay between onset of hyperpolarization and closure of the Kv2/Kv8.2 channel. Taken together, these studies highlight the influence of the KV8.2 silent modifier on the kinetics of KV2 homomeric channels. Specifically, the inclusion of KV8.2 fine tunes the KV2 potassium channel through modulation of activation and inactivation properties. The KV8.2-mediated alterations allow KV2/KV8.2 heteromers to effectively function in the unique cellular environment of the photoreceptor.

1.5 *KCNV2* Retinopathy

1.5.1 Overview

In 1983, 118 years after the discovery of the electroretinogram, siblings aged 11 and 15 presented in Dr. Peter Gouras' New York City clinic with "a most unusual alteration of the rod system" (Gouras et al., 1983). In addition to reading difficulties, extreme light sensitivity, and night blindness, an abnormal scotopic b-wave was detected. At low intensity stimuli, the b-wave was entirely absent or diminished and delayed relative to unaffected individuals. Remarkably, as stimulus intensity was incrementally increased, the b-wave amplitude climbed sharply and surpassed the normal threshold by a significant margin. In addition to these scotopic observations, severe dysfunction of the cone system manifested as reduced ERG amplitudes under photopic conditions. Assessment of other unaffected family members led to the conclusion that the condition was inherited in an autosomal recessive pattern (Gouras et al., 1983). At this time, there were no documented cases of ocular disorders that featured this unusual combination of electrophysiological deficits. As a result, the condition was coined *cone dystrophy with supernormal rod response* (CDSRR), a direct reference to the ERG waveforms observed in the subjects.

One year after its initial identification, news of the unusual cone dystrophy travelled down the interstate highway to the University of Illinois where three patients presented with supernormal scotopic ERGs. Aside from possession of the hallmark waveform, investigation of the subjects' fundi revealed that all three had some degree of macular dystrophy (Alexander & Fishman, 1984). The frequency of reports of CDSRR diminished and were largely absent until after the turn of the 21st century. The lack of reports was likely due to the fact that some of the clinical features of CDSRR are subtle and difficult to detect, leading to the disease being largely underdiagnosed or misdiagnosed altogether (Zelinger et al., 2013).

1.5.2 Discovery of the Genetic Origin

The Human Genome Project in the 1990s provided the reference library that greatly facilitated identification of genetic correlates of human disease (Lander, 2011). The published human genome led to a resurgence in the investigation of CDSRR in 2005 when Dr. Michel Michaelides and colleagues attempted to correlate the CDSRR to the gene *NR2E3*. This gene was associated with Enhanced S-cone Syndrome, the only other inherited retinal disease that features supernormal ERGs (Haider et al., 2000). As a result, *NR2E3* represented a logical starting point in the hunt for the genetic basis of CDSRR. The group concluded that variants in *NR2E3* were not the cause of CDSRR; however, their in-depth phenotypic assessment of 10 individuals with CDSRR-like ERGs was an important contribution to the disease characterization (Michaelides et al., 2005). One year later, the same research group identified a strong correlation between CDSRR and the potassium channel subunit gene *KCNV2* (Wu et al., 2006). CDSRR has since been exclusively linked to mutations in *KCNV2* and has led to the conventional renaming of the disease to *KCNV2* retinopathy (Abdelkader et al., 2020; Robson et al., 2010; Vincent et al., 2013; Wissinger et al., 2008; Zobor et al., 2012). *KCNV2* is a 2-exon gene that encodes the protein product $K_V8.2$, the silent modifier subunit in $K_V2/K_V8.2$ heteromeric potassium channels. The gene's probable involvement in the photoreceptor current I_{kx} made it a reasonable candidate for the electrophysical and qualitative traits observed in patients with *KCNV2* retinopathy.

There are many unique variants of *KCNV2*; however, two alleles in particular have been identified as major contributors to the disease in a survey of all documented *KCNV2* variants (Guimaraes et al., 2020). The variant of highest frequency is c.1381 G > A (p.Gly461Arg), found within the highly conserved potassium-selective GYG motif of the pore domain. This mutation accounts for ~35% of the total variants in the gene. Additionally, c.427 G > T (p.Glu143X) was identified as a second mutational hotspot located in the NAB domain, the region responsible for subunit assembly (Yu et al., 1996). There is no strong correlation between specific variants and disease manifestation, although some evidence suggests that individuals completely lacking K_V8.2 protein product have more severe phenotypes than those with amino acid deletions or substitutions (Zobor et al., 2012).

1.5.3 Clinical Phenotype

With the genetic locus of *KCNV2* retinopathy identified and genetic screening becoming more routine in the clinic, detailed phenotypic studies of the disease began accumulating. Such accounts have helped to define the disease characteristics and offer suggestions towards possible disease mechanisms. In general, individuals are first affected by the disease in the first or second decade of life. They frequently present to the clinic with a central blind spot, colour blindness, night blindness, myopia (near-sightedness), photophobia (light sensitivity), and reduced visual acuity (Abdelkader et al., 2020; Robson et al., 2010; Vincent et al., 2013; Wissinger et al., 2008; Wu et al., 2006; Zobor et al., 2012). Disease features such as these are variable, but largely aid the genetic, electrophysiological, and fundus assessments in the diagnosis of *KCNV2* retinopathy.

ERG findings of *KCNV2* retinopathy have been briefly discussed in Section 1.5.1, but a detailed description of the disease hallmark is important. A common finding first identified by Gouras and colleagues in 1983 has been an absent or late scotopic b-wave (Gouras et al., 1983). The increased implicit time of the dim flash scotopic b-wave has been observed in all electrophysiology studies to date (Abdelkader et al., 2020; Robson et al., 2010; Vincent et al., 2013; Wissinger et al., 2008; Wu et al., 2006; Zobor et al., 2012). Additionally, the absence of the scotopic b-wave to the dimmest recordable intensity was observed in many studies (Abdelkader et al., 2020; Robson et al., 2010; Vincent et al., 2013; Wu et al., 2006); however, two reports failed to identify this feature (Wissinger et al., 2008; Zobor et al., 2012). The most prominent electrophysiological feature, the supernormal scotopic b-wave, is a feature that has recently been called into question due to considerable overlap with normal amplitudes (Abdelkader et al., 2020; Robson et al., 2010; Zobor et al., 2012). The hallmark supernormal b-wave is certainly a feature in the ERGs of some affected individuals, but its periodic absence in *KCNV2* retinopathy indicates not all affected individuals exhibit the same phenotype. Regardless, a consistent finding even in the absence of a supernormal scotopic b-wave is the rapid increase in b-wave amplitude relative to unaffected individuals as the stimulus intensity increases (Abdelkader et al., 2020; Robson et al., 2010; Zobor et al., 2012).

Analysis of the photopic ERG has demonstrated a large reduction in cone system function (Robson et al., 2010; Vincent et al., 2013; Wissinger et al., 2008; Wu et al., 2006), though a recent study of 15 individuals with *KCNV2* retinopathy found their cone b-wave amplitudes to fall within normal parameters (Abdelkader et al., 2020). Another assessment of the cone system, the 30 Hz flicker ERG, consistently demonstrated dysfunction relative to unaffected individuals, even in individuals with normal photopic ERG waveforms (Abdelkader et al., 2020; Robson et al., 2010; Vincent et al., 2013; Wu et al., 2006). As mentioned in Section 1.3.1, the flicker ERG selectively stimulates cones due to their hastened refresh rate relative to rods. Single photopic flashes are cone-dominated, but also contain transient responses from light-adapted rods (McCulloch et al., 2015). Broadened a-waves, another consistent finding on the ERG waveform, feature an increased implicit time relative to unaffected individuals (Fujinami et al., 2013; Robson et al., 2010; Vincent et al., 2013; Zobor et al., 2012). Finally, studies of isolated oscillatory potentials from the patient ERG waveforms found them to be severely irregular, presenting with reduced amplitudes and distorted waves (Wissinger et al., 2008; Zobor et al., 2012).

Fundoscopy has proven to be another useful approach in the characterization of *KCNV2* retinopathy. Although there is vast variability in colour fundus photography findings, changes to the fundus are consistently localized to the macula in *KCNV2* retinopathy (Abdelkader et al., 2020; Robson et al., 2010; Wissinger et al., 2008; Zobor et al., 2012). Degeneration in this location reflects the general loss of visual acuity and photopic ERG response discussed above. Outside of the central degeneration is a relatively normal presenting peripheral retina (Robson et al., 2010; Zobor et al., 2012). Fundus autofluorescence (FAF) imagery measures the level of autofluorescence produced by lipofuscin, molecules stored in the liposomes of RPE cells (Tsang & Sharma, 2018). The RPE normally takes up precursors of lipofuscin through phagocytosis of shed outer segment discs, but altered levels of accumulation can occur in disease states (Tsang & Sharma, 2018). FAF findings in *KCNV2* retinopathy are also highly variable, but a common feature is a parafoveal ring of hyperreflectivity which represents dysfunction or loss of the photoreceptor or RPE cells (Abdelkader et al., 2020; Robson et al., 2010).

Finally, optical coherence tomography (OCT) is a non-invasive imaging approach that generates cross-sectional images of the retina and the layers within. Briefly, OCT measures the refractive index of tissues by reflecting a beam of low coherence light off of the retina. The beam is then captured by the OCT apparatus and compared to a reference beam that was reflected off of a mirror. Differences between the two beams, namely the intensity and timing, are then used to generate a 2D image of a plane of the retina (a so-called a-scan). Multiple a-scans can be stacked together to produce a 3D image (b-scan) that gives insight into the cross sectional architecture of the retina (Tsang & Sharma, 2018). Several studies have utilized OCT to investigate morphological changes to the retina associated with *KCNV2* retinopathy. As with the fundus findings discussed above, OCT imaging revealed abnormalities localized to the macula of affected individuals. Specifically, these examinations identified disruption of the macular photoreceptor layer, once again supporting the functional reduction in visual acuity and photopic ERG amplitude (Abdelkader et al., 2020; Kiray et al., 2020; Sergouniotis et al., 2012; Vincent et al., 2013; Wissinger et al., 2008; Zobor et al., 2012). Central retinal thickness was reduced in affected individuals (Vincent et al., 2013), reflecting atrophy in this region. Distal a-scans can image the photoreceptor mosaic, a highly organized pattern that photoreceptors occupy across the retina. The cone-specific photoreceptor mosaic was found to be significantly disrupted in humans with *KCNV2* retinopathy (Vincent et al., 2013). As with most of the clinical presentations of *KCNV2* retinopathy, variability exists in the degree of OCT abnormality. Changes to the retinal cross section were nonspecific; however, they highlight several important indications of a dysfunctional macula in of *KCNV2* retinopathy. The mechanism underlying the macular restriction of morphological features in *KCNV2* retinopathy is unclear, but consistent.

In summary, functional data from electrophysiological studies have shown widespread dysfunction of the retina. Increased scotopic implicit times and variable wave amplitudes with a rapid increase relative to unaffected individuals identifies deficiencies in the rod system. Simultaneously, photopic experiments point to a cone system disease through latent and diminished light-adapted ERG waves. A pan-retinal dysfunction is not surprising, as K_V8.2 is expressed in both rod and cone photoreceptors of the macaque (Gayet-Primo et al., 2018). However, retinal imagery through OCT, FAF, and fundus photography identified macula-specific pathologies with no apparent peripheral retina involvement. It is curious that the rod system in *KCNV2* retinopathy has such a robust functional phenotype, yet a seemingly unaffected morphology. I_{kx}, the potassium current mediated by K_V8.2/K_V2 heteromeric channels has been extensively studied in rod photoreceptors of several animals (Barrow & Wu, 2009a; Beech & Barnes, 1989; Demontis et al., 1999; Gayet-Primo et al., 2018); however, identification of I_{kx} in cones has been limited to two studies in macaque (Gayet-Primo et al., 2018) and zebrafish (Fan & Yazulla, 1997). The disconnection between the functional and morphological manifestations of *KCNV2* retinopathy and the limited investigation of I_{kx} in cones warrants the need for further research on these topics.

1.5.4 Current Understanding

To date, the disease mechanism of *KCNV2* retinopathy remains enigmatic. The first animal model of *KCNV2* retinopathy was created in 2019 (Hart et al., 2019). The organism of choice was the mouse, a staple of laboratory animal models of disease. The Australian research group generated three distinct mutant lines: a K_V8.2 knockout, a K_V2 knockout, and a double knockout mutant. They characterized the retinal architecture and functional capacity of 6-month-old female mutant and wildtype mice. The data gathered from these mutant mice provided valuable insight into the disease process that could not have been inferred from human patients living with *KCNV2* retinopathy. Overall, the mouse model of *KCNV2* retinopathy had pathologic retinal changes and altered ERG waveforms relative to wildtype mice (Hart et al., 2019).

Hart and colleagues analysed retinal organization of K_V8.2, K_V2, and double mutant mice. They determined that the total retinal thickness of all mutant mice was significantly lower than wildtype control mice (Hart et al., 2019). Furthermore, they localized the thickness disparity specifically to the photoreceptor layer (outer nuclear, inner segment, and outer segment layers). Interestingly, a TUNEL assay revealed a significant level of cell death in the retinae of mutant mice (Hart et al., 2019). Specifically, they found that cone photoreceptor numbers had been reduced to ~80% of that in the wildtype retina in all mutants (Hart et al., 2019). The authors claimed that rod photoreceptors died in even greater numbers, though this was not supported through any quantification. Through the assessment of retinal morphology in the novel mouse model of *KCNV2* retinopathy, the authors identified increased retinal cell death as a significant component of disease process.

Retinal function was then assessed in the mouse model through a series of ERG tests. Under scotopic lighting conditions, the authors identified a reduced a-wave amplitude and delayed b-wave implicit time in mutant mice at all stimulus intensities (Hart et al., 2019). The mutant scotopic b-wave amplitude, the ERG waveform most commonly investigated in *KCNV2* retinopathy, ranged from subnormal to normal across all intensities (Hart et al., 2019). Under photopic conditions, the mouse model generated b-waves that were around half of the amplitude observed in wildtype mice (Hart et al., 2019). Mouse ERGs generate robust OPs, an understudied feature of the waveform in *KCNV2* retinopathy. Here, the authors identified a significant reduction in early OP amplitude (OP1 and OP2) in all mutants and an increased OP implicit time in KV2 and double mutants (Hart et al., 2019). Unfortunately, the significance of the disrupted OPs is unclear since we do not yet understand the biological basis for these ERG peaks. Overall, the retinal function of the *KCNV2* retinopathy mouse model exhibits some features akin to the human disease, namely the delayed and reduced scotopic b-wave and the reduction of the photopic b-wave.

Investigation of both KV8.2 and KV2 (and their combination) knockout mice broadens our inquiry into the disease mechanism. KV2 variants have not yet been reported in cases of *KCNV2* retinopathy, although this may be due to a narrow focus on KV8.2 variants. Importantly, KV2 mutant mice revealed significant changes to both form and function of their retinae. Further investigation into the disease manifestation of K_V2 mutants will surely clarify our understanding of its role in vision and disease. Additionally, the novel mouse model gave researchers a first look past that of OCT into the organization of the $K_V8.2$-deficient retina. The higher resolution images captured through histology highlighted changes at the cellular level of the mutant retinae. Taken together, the recent development of a mouse model of *KCNV2* retinopathy shows promising results.

However, the investigation of this mouse model is not without its shortcomings. While TUNEL analysis positively marked upwards of four thousand retinal cells, cone cell death in the mutant retina only accounted for ~25% of missing cell representation (Hart et al., 2019). The identities of the remaining three quarters of dead or dying cells remains a mystery that may hold valuable information into the nature of *KCNV2* retinopathy. Additionally, the choice of mice as a model organism limited the size of each mutant cohort to three individuals. Although this is common in mouse studies, the level of variability with such small sample sizes in undeniable. Furthermore, mice and human retinae differ significantly from an anatomical perspective. The nocturnal nature of mice leads to a significantly higher rod:cone ratio than that of humans (Jeon et al., 1998). As *KCNV2* retinopathy manifests both scotopically and photopically, the differential photoresponses generated using the mouse retina cannot accurately reflect the human condition, and the question remains as to why cone survival is particularly impacted in patients. Regardless, the mouse model of *KCNV2* retinopathy provided the scientific community with an animal model of this rare disease and hope for shedding light on the puzzling disease mechanism.

1.6 Zebrafish as a Disease Model

1.6.1 Overview

Over recent years, the zebrafish (*Danio rerio*) has risen to become a popular animal model for the study of human disease. Although not as genetically similar to humans as other research animals like mice, zebrafish have homologs for roughly 70% of human genes (Howe et al., 2013). Zebrafish underwent a teleost-specific whole genome duplication over 300 million years ago, so there are often two paralogs within fish for each homolog of a human gene (Glasauer & Neuhauss, 2014). One paralog will often become non-functional and the original function of the gene will be retained by the remaining copy (Glasauer & Neuhauss, 2014). In some cases, the paralogs will specialize in subsets of the same function (sub-functionalization) or develop novel functions altogether (neo-functionalization) (Glasauer & Neuhauss, 2014). For the zebrafish *KCNV2* homolog, two paralogs exist: *kcnv2a* and *kcnv2b*. It is not currently known what the functions of the paralogs are within the zebrafish, although *kcnv2a* was recently identified in the transcriptome of the zebrafish rod (Sun et al., 2018). Additionally, *kcnv2b* transcripts have been found in larval whole-eye lysates, indicating preservation of an ocular function for *kcnv2b* (Nadolski et al., 2020). Interestingly, a current consistent with I_{kx} was found in zebrafish blue cones following cellular recordings of retinal slices (Fan & Yazulla, 1997). Zebrafish genetics are complex but create an opportunity to study both human disease mechanisms and novel biological paradigms.

From gastrointestinal tracts to hearts to eyes, the conservation of vertebrate organs in zebrafish allows researchers to study a wide range of physiological processes common between humans and zebrafish. A pair of zebrafish will typically produce hundreds of fertilized eggs following each breeding leading to a high fecundity relative to mice. Furthermore, large numbers of zebrafish can be densely housed in racked fish tanks, allowing for maintenance of numerous genetic strains. Ultimately, experiments utilizing zebrafish can be done in high numbers while keeping operating costs moderately low.

Zebrafish also develop externally from the parents, which creates an opportunity for early access to genetic manipulation. With the injection of genomic editing tools into the single cell zygotes, genomic modification occurs in the early blastomere embryo and is therefore highly penetrant. CRISPR-Cas9 mutagenesis was used to precisely disrupt the genetic sequence of a gene of interest. As our understanding of the genetic basis of disease increases and the precision and versatility of genomic editing improves, the versatile zebrafish presents itself as a powerful animal model of human disease.

1.6.2 Zebrafish Retinal Structure

The zebrafish retina displays striking similarity to the human retina with three cellular layers separated by two plexiform layers (Richardson et al., 2017). The identities of the cell layers are conserved between the two species: an outer nuclear layer containing photoreceptors; an inner nuclear layer containing interneurons (bipolar, horizontal, and amacrine cells); and a retinal ganglion cell layer. In zebrafish, photoresponses are generated and follow a similar pathway as occurs in humans.

In the human retina, cones make up 5% of the total photoreceptor population and are distributed heterogeneously across the retina (Forrester et al., 2016). Cones primarily populate the macula with sparse peripheral representation. Importantly, the zebrafish retina has a uniform 1:1 cone: rod ratio that is similar to the cone-rich human macula (Richardson et al., 2017), making the fish eye an ideal organ to study the cone system of the retina. It should be noted that zebrafish have an additional cone subtype sensitive to UV light, affording zebrafish *tetrachromatic* vision (Richardson et al., 2017). Regardless of small differences, the similarities between these two retinae make the zebrafish eye an extremely useful model for the investigation of human ocular disease.

1.7 Purpose

The primary objective of this thesis was to develop a zebrafish model of *KCNV2* retinopathy. As discussed above, the pathogenic mechanism underlying this rare disease is still unknown. Functional data highlight deficiencies across the entire retina that affect both the rod and cone systems (Abdelkader et al., 2020; Fujinami et al., 2013; Kiray et al., 2020; Robson et al., 2010; Sergouniotis et al., 2012; Vincent et al., 2013; Zelinger et al., 2013; Zobor et al., 2012). The current mouse model of *KCNV2* retinopathy provides a means for investigating the disease mechanism, but due to anatomical differences between the mouse and human retina, does not exhibit a comparable cone system response. Owing to their nocturnal behaviour, the mouse retina is overwhelmingly rod-dense with only a small selection of cone photoreceptors. Furthermore, the mouse retina does not feature a macula or similarly cone-dense structure. Conversely, the zebrafish retina has a roughly equal representation of cone and rod photoreceptors, similar to the human macula (Richardson et al., 2017).

Hypothesis: Loss of $K_V8.2a$ and $K_V8.2b$ will disrupt cone and rod function in the zebrafish eye and produce a phenotype analogous to the human disease *KCNV2* retinopathy.

My first aim was to develop a zebrafish line that harboured mutations analogous to those seen in humans with *KCNV2* retinopathy. To do this, CRISPR-Cas9 mutagenesis was used to manipulate the genetic sequence of *kcnv2a* and *kcnv2b*, genetic homologs to human *KCNV2*. The generation of this double mutant line (*kcnv2a; kcnv2b*) produced zebrafish that effectively mimicked the genotype of individuals with *KCNV2* retinopathy.

My second aim was to develop a methodology for electroretinography assessment of *kcnv2a; kcnv2b* mutant zebrafish. Aside from genetic testing, the ERG waveforms of patients with *KCNV2* retinopathy are useful diagnostic indicators. Zebrafish ERG technology was not available locally prior to this thesis work, so the implementation discussed here not only adds to the methodology of this project, but also to other zebrafish ocular disease investigations at the University of Alberta. In addition, I developed a new and simplified method that may improve adoption of zebrafish ERG analysis at other institutions.

My final aim was to characterize retinal cell morphology and function in the double mutant fish I generated in my first aim. To do this, I utilized OCT, histology, and the ERG methodology developed in my second aim.

CHAPTER 2: MATERIALS AND METHODS

2.1 Animal Ethics

Approval for this study was obtained from the Animal Care and Use Committee: Biosciences, under protocol AUP1476.

2.2 Zebrafish Care

Zebrafish were cared for following standard protocols (Nüsslein-Volhard & Dahm, 2002; Westerfield, 2000). Larvae were grown in E2 embryo media (15 mM NaCl, 0.5 mM KCl, 1 mM $MgSO_4$, 0.15 mM KH_2PO_4, 1 mM $CaCl_2$, 0.7 mM $NaHCO_3$) and kept in a 28.5°C incubator until 5 days-post-fertilization (dpf). Zebrafish were then transferred to 3.5 L tanks at a density of 30-60 fish/tank. Once fish reached adulthood, their density was reduced to 15 fish/tank to optimize developmental conditions. Zebrafish were grown under 14:10 hour light/dark conditions. Tüpfel long-fin (TL) zebrafish were used as wildtype control fish throughout this thesis and served as the genetic background for the *kcnv2* mutants. Tricane mesylate (TMS) anesthetic (Acros Organics, Geel, BE) was prepared as a stock solution by mixing 400 mg tricane powder, 97.9 mL distilled water, and 2.1 mL 1M Tris pH 9. A 4.2% working solution was prepared with distilled water for zebrafish anesthesia.

2.3 CRISPR Mutagenesis

The CHOPCHOP web tool (https://chopchop.cbu.uib.no) was used to select target sites for *kcnv2a* and *kcnv2b* CRISPR-Cas9 mutagenesis (Labun et al., 2019). Two Cas9 target sites were selected for *kcnv2a* (Target 1 & Target 2; Figure 2.1; Table 2.1), and a single target was selected for *kcnv2b* (Target #184; Figure 2.1; Table 2.1). Target sites were required to adhere to a strict

(G/A)(G/A)-N_{19}-GG sequence structure, where the 3' NGG was representative of the protospacer adjacent motif (PAM; Gagnon et al., 2014). Additionally, target sites that had a high G/C content (>50%) and that were near the 5' end of the first exon were given selection preference. All target sites for *kcnv2a* and *kcnv2b* were selected upstream of the first transmembrane domain in the K_V8.2a and K_V8.2b protein products.

Cas9 is known to introduce a double-stranded break (DSB) in the DNA 3 base pairs (bp) upstream from the PAM (Jiang & Doudna, 2017), so precise cut sites could be determined for each target selected. For *kcnv2a*, Target 1 directed Cas9 to cut after the 652nd nucleotide (nt) and Target 2 after the 753rd nt. The upstream Target 1 corresponded to a leucine residue in the 217th position on the predicted protein. The two *kcnv2a* target sites were designed 82 nt apart with the intention of generating a large deletion following co-injection of both single guide RNAs (sgRNAs), which are molecules that direct Cas9 to the target site (Figure 2.1). For *kcnv2b*, a single target site was selected to introduce a DSB after the 345th nt, corresponding to a leucine residue at the 115th position in the protein sequence.

sgRNAs were generated as previously described (Gagnon et al., 2014), by first annealing the target-specific oligonucleotide (hereinafter *oligo*) with a constant oligo (Table 2.1). Target-specific oligos contained 20 nucleotides specific to the target site selected flanked on one side by a SP6 promoter sequence and on the other side by a region complementary to the constant oligo. The PAM was not included in the sgRNA sequence but was required to be present in the genome for effective Cas9 nuclease activity. Annealing of the target-specific and constant oligos was accomplished by combining 1 µL of both oligos (100µM) with 8 µL molecular biology grade water. The mixture was then heated to 95°C for 5 minutes before decreasing the temperature to

85°C at a rate of -2°C/second. Following this, the temperature was decreased further to 25°C at a rate of -0.1°C/second, and the reaction then put on ice.

The overhanging ssDNA was then filled in by adding 2.5 μL dNTP (2.5 mM each), 2 μL 10X Buffer 2 (New England Biolabs (NEB), Ipswich, MA), 0.2 μL 100X bovine serum albumin (BSA; NEB), 0.5 μL T4 DNA polymerase (NEB), and 4.8 μL molecular biology grade water to the annealed oligo mixture. The reaction was then incubated at 12°C for 20 minutes before being purified with a PCR cleanup kit (Qiagen, Hilden, DEU) and eluted in 30 μL of molecular biology grade water. A small amount of the reaction mixture was then run on an agarose gel to confirm an oligo size of ~120 bp.

The filled-in oligos were transcribed with an Ambion MEGAscript SP6 Kit (Life Technologies, Carlsbad, USA) by mixing 0.5 μL each of ATP, GTP, CTP, UTP, 10X buffer, SP6 RNA polymerase, 1 μL water, and 1 μL template DNA. The transcription reaction was then incubated at 37°C for 3 hours before adding 14 μL of molecular biology grade water and 1 μL of TURBO DNase (Life Technologies). Finally, the transcription reaction was left to incubate at 37°C for an additional 15 minutes.

Transcription reactions were purified by adding 10 μL of 5 M ammonium acetate and 60 μL of 100% ethanol and incubating at -80°C overnight. The next morning, the tubes were centrifuged at 13 000 rpm for 15 minutes at 4°C. The supernatant was removed, and 1 mL of 70% ethanol added. The samples were centrifuged for an additional 5 minutes at 13 000 rpm at 4°C and the supernatant was removed again. The pellet was allowed to dry at room temperature before resuspending in 50 μL of molecular biology grade water. Final sgRNA concentrations were determined on a NanoVue spectrophotometer (GE Healthcare, Chicago, USA) and ensured to be between 200-400 ng/µL.

Upwards of 50 single-cell embryos of wildtype TL zebrafish were injected with 3 nL of the CRISPR-Cas9 mutagenesis mixture. The injection mixture for *kcnv2a* contained 2 µL of sgRNA (1 µL of each sgRNA) & 1 µL Alt-R® S.p. HiFi Cas9 Nuclease V3 (1000 ng/µL; Integrated DNA Technologies, Coralville, USA), plus a small amount of phenol red solution diluted in RNase-free water to visualize the injection bolus. The injection mixture for *kcnv2b* contained 3 µL of sgRNA #184 (44 ng/µL; Table 2.1) and 2 µL of Alt-R® S.p. Cas9 Nuclease V3 (1000 ng/µL). Injections were performed under a Zeiss stereo microscope with a WPI micromanipulator (World Precision Instruments, Sarasota, USA). Injection needles were made from filamented borosilicate glass capillary tubes (OD 1.20 mm, ID 0.90 mm; Sutter Instruments, Novato, USA) pulled on a Sutter micropipette puller (Sutter Instruments, Novato, USA). Injected embryos and a selection of uninjected sibling controls were allowed to develop for 1-5 days at 28.5°C in embryo media before genotyping.

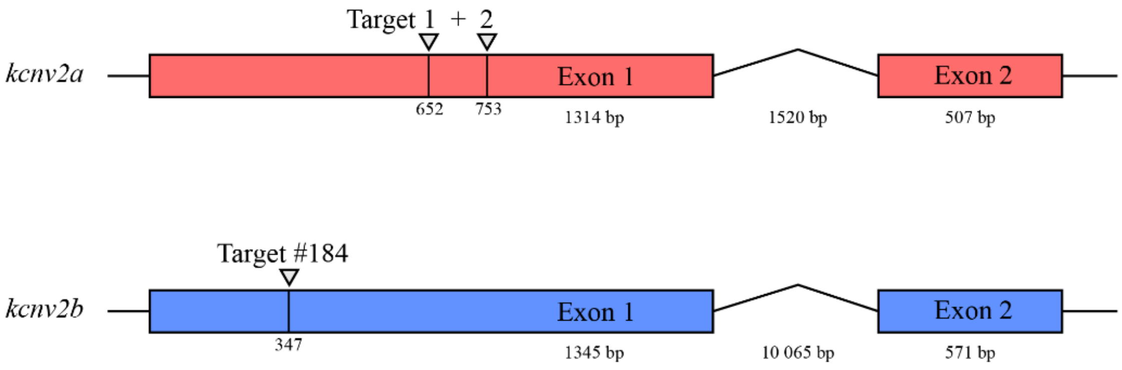

Figure 2.1 – CRISPR-Cas9 target sites. Illustrations of the *kcnv2a* and *kcnv2b* exon map highlighting the CRISPR-Cas9 target sites selected through CHOPCHOP for mutagenesis. Two

target sites separated by 82 nt were selected mid-way through the first exon of *kcnv2a.* A single target site was selected for *kcnv2b* near the 5' end of the first exon. All CRISPR-Cas9 targets were selected upstream of the first transmembrane domain in the transcribed protein.

Oligo ID	**Sequence**
kcnv2a Target 1	ATTTAGGTGACACTATAGGAACATGAGGACTTGTTTCGTTTTAGAGCTAGAAATAGCAAG
kcnv2a Target 2	ATTTAGGTGACACTATAGTCGATCATAGCCAAAATCAGTTTTAGAGCTAGAAATAGCAAG
kcnv2b Target #184	ATTTAGGTGACACTATAAGAGATCCATCTTCATGTTGGTTTTAGAGCTAGAAATAGCAAG
Constant Oligo	AAAAGCACCGACTCGGTGCCACTTTTTCAAGTTGATAACGGACTAGCCTTATTTTAACTTGCTATTTCTAGCTCTAAAAC

Table 2.1 – Oligomer sequence identity of both *kcnv2a* target sites and the constant oligo. Target oligos have three distinct motifs: The 20 underlined nucleotides represent bases specific to the target site, excluding the PAM. The remaining nucleotides upstream of the target motif are the promoter for SP6 required for *in vitro* transcription of the sgRNA. Downstream from the target motif is the overlap region. The overlap region is reverse complimentary to the 3' end of the constant oligo and facilitate annealing of target and constant oligos.

2.4 Genotyping

2.4.1 High Resolution Melt Analysis

High resolution melt (HRM) analysis was used to identify genetic sequence variation in the potentially mutated zebrafish. Pools of 10 injected zebrafish were analysed alongside pools of 10 uninjected control siblings. Genomic DNA (gDNA) was extracted from each group of zebrafish by heating euthanized larvae in 100 µL of 50 mM NaOH at 95°C for 20 minutes before cooling and neutralizing with 10% v/v Tris pH 8. Crude gDNA extract was then diluted with molecular biology grade water to a V_{10} working solution. HRM primers for *kcnv2a* (#235 and #236; Table

2.2) were designed to flank both Target 1 and Target 2 cut sites. HRM primers for *kcnv2b* (#188 and #189; Table 2.2) flanked the single Cas9 target site. For a full run of 80 samples, a master mix was made by combining 400 µL of HRM Master Mix (Qiagen Type-it HRM PCR kit) with 112 µL each of the appropriate forward and reverse primer (5 mM ea.). 8 µL of the master mix was then combined with 2 µL of the V_{10} gDNA before being placed in a Rotor-*Gene* Q HRM machine (Qiagen). Three technical replicates of each pool of gDNA were used to increase confidence in the DNA melt curves. The HRM protocol began with an initial temperature increase to 95°C for 5 minutes before 40 cycles of the following: 95°C for 10 seconds (DNA denaturation) then 55°C for 30 seconds (annealing and extension). Amplicons were then melted in an increasing temperature ramp beginning at 65°C and ending at 95°C at a rate of 0.1°C/2 seconds. Fluorescent data was collected by the Rotor-*Gene* Q HRM machine and displayed through its associated software.

Oligo ID	**Sequence (5'-3')**
kcnv2a #231F	TGTCCTCTCCGGTTAAGAACT
kcnv2a #232R	TGCATTTCCTCTACCGTGTTG
kcnv2a #235F	GCTCAACATCAACGTAGGAGGC
kcnv2a #236R	ATGTTGGGGAAGACGTCTGGGT
kcnv2b #188F	ATACCCGCAAACCAGACTTG
kcnv2b #189R	TCCTCGGACAGAGTTCGTCT
kcnv2b #197F	TCAACGTTGGAGGAAAGTCC
kcnv2b #198R	CAAACGCTTCTTCGTTCTCC

Table 2.2 – Sequences of primers used to amplify *kcnv2a* and *kcnv2b* CRISPR-targeted regions. All primers were ordered through Integrated DNA Technologies with standard desalting purification. Note that some primers were used for both standard polymerase chain reaction (PCR) amplification and for PCR amplification integrated with HRM analysis.

2.4.2 Polymerase Chain Reaction Amplification

Standard polymerase chain reaction (PCR) amplification of regions of *kcnv2a* and *kcnv2b* was carried out for further genetic analysis of mutations induced by CRISPR cutting and later for genotyping assays (see Section 2.4.5). Primers were designed to flank the Cas9 target sites for both *kcnv2a* and *kcnv2b*. Primers #231 and #232 were used for PCR amplification of *kcnv2a*, while primers #197 and #198 were used to amplify *kcnv2b* (Table 2.2). gDNA was extracted from whole larvae or adult zebrafish fin tissue as described above and diluted to a V_{10} working solution. Each 25 µL PCR reaction contained 2 µL V_{10} gDNA mixed with 14.25 µL molecular biology grade water, 2 µL each of forward and reverse primer (5 mM ea.), 2 µL dNTP (2.5 µM ea.), 2.5 µL ExTaq Buffer (TaKaRa Bio Inc., Kusatsu, JPN), and 0.25 µL Taq polymerase (Invitrogen, Carlsbad, USA). Thermocycler protocols for PCR amplification of both genes are outlined in Figure 2.2.

PCR amplification of the expected size DNA fragment was confirmed by running a 2 µL sample of the reaction on a 1% TAE (Tris-acetate-EDTA) agarose gel. The remaining DNA was then used for TOPO cloning or sent directly for sequencing (see Sections 2.4.3 and 2.4.4). Alternatively, the PCR reaction was used for a genotyping assay as described in Section 2.4.5.

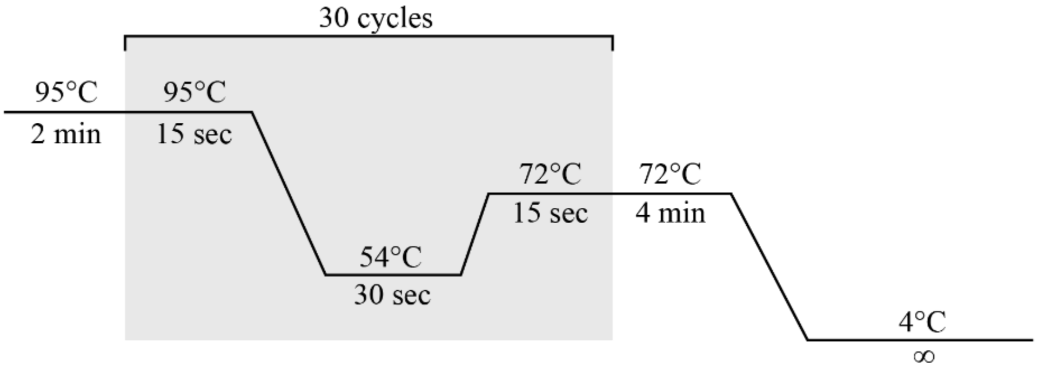

Figure 2.2 – PCR protocol for amplification of *kcnv2a* and *kcnv2b*. Thermocycler settings were identical for both *kcnv2a* and *kcnv2b*. Protocols were optimized for both genes using several primer combinations. For *kcnv2a,* primer combination #231 and #232 paired with the protocol outlined above was found to produce bright singular on agarose gels. Similarly, primer combination #188 and #198 was determined to be the most effective for amplification of *kcnv2b*.

2.4.3 TOPO Cloning

TOPO cloning was used to identify genetic variants introduced through CRISPR-Cas9 mutagenesis. TOPO cloning was particularly useful for allele identification in the mosaic P_0 fish or in the heterozygous F1 generation, as each vector contained one allele and could be used to provide an orderly nucleotide sequence.

To begin, both genes were amplified from CRISPR-Cas9 injected fish *via* PCR using primers #231 and #232 for *kcnv2a* and #197 and #198 for *kcnv2b* (Table 2.2). Poly A overhangs were added to each amplicon by mixing 16.5 µL of the PCR product with 2 µL 10X ExTaq buffer, 1 µL dNTP (2.5 µM each), and 0.5 µL Taq Polymerase before incubating at 72°C for 10 minutes. Amplicons were then inserted into pCR2.1 or pCR4 TOPO vectors (Thermo Fisher, Waltham, MA) by mixing 4 µL poly A PCR product with 1 µL salt solution and 1 µL vector. This mixture was allowed to incubate at room temperature for 5 minutes before transforming into One Shot® TOP10 chemically competent *E. coli* (Thermo Fisher). 2 µL of the vector/PCR mixture was combined with 50 µL of *E. coli* and left on ice for 30 minutes. Transformation of the vector into the *E. coli* was then facilitated by a heat shock in a 42°C water bath for 30 seconds. Tubes were immediately put on ice and 250 µL of S.O.C. (Super Optimal broth with Catabolite repression) medium was added to the mixture.

The bacteria were allowed to incubate at 37°C for 30 minutes before plating. 100 µL of the cell mixture was spread onto Luria-Bertani (LB) agar plates containing 50 µg/mL carbenicillin and left in a 37°C incubator overnight. Bacterial colonies resulting from a single transformant were selected and used to inoculate glass test tubes of LB liquid medium containing 50 µg/mL carbenicillin. The test tubes were then left to incubate at 37°C on a shaker overnight. Plasmids were purified the following morning using a Mini-Prep kit (Qiagen) and prepared for sequencing by mixing 575 ng of the purified plasmid (determined on a NanoVue spectrophotometer (GE Healthcare)) with 0.5 µL M13F primer, and molecular biology grade water up to 10 µL.

2.4.4 Sanger Sequencing

Sanger sequencing was outsourced to the University of Alberta's Molecular Biology Services Unit (MBSU). Samples were prepared as described above for TOPO cloning; however, the eventual routine sequencing of homozygotic mutants was performed directly on purified PCR product. For sequencing using purified PCR products, sample concentration was determined on a NanoVue spectrophotometer (GE Healthcare) and subsequently diluted to a concentration of 15 ng/µL and topped up to 9.5 µL with molecular biology grade water. Finally, 0.5 µL of a single gene-specific primer (#232 for *kcnv2a* and #198 for *kcnv2b*) was included into the mixture before submitting the sample to MBSU. Regardless of whether the sample contained PCR product or purified plasmid, samples were sequenced using a 3730 DNA Analyser (Thermo Fisher) and BigDyeTerminator v3.1 Mastermix (Thermo Fisher). Through this service, an 85 bp deletion starting at the 652nd nucleotide in *kcnv2a* and a 2 bp deletion at the 345th nucleotide in *kcnv2b* were identified in the CRISPR-Cas9 injected zebrafish. Allelic designations were subsequently assigned as *kcnv2a*$^{\text{ua1023}}$ and *kcnv2b*$^{\text{ua1025}}$.

2.4.5 Genotyping Assays

Once the *kcnv2a* and *kcnv2b* frameshift alleles were identified, subsequent generations of heterozygous and homozygous mutants were identified using the PCR genotyping assays described here. The initial PCR reactions were performed as described in Section 2.4.2.

For *kcnv2a*, the 85 bp deletion was sufficiently large as to create a detectable difference in amplicon size when run on an agarose gel. For further resolution, we loaded the samples on a 3% sodium borate (SB) gel (Brody & Kern, 2004) that was run at 200 V for ~40 minutes. SB buffer was made as a 20X stock solution by combining 45 g of boric acid (Sigma-Aldrich, St. Louis, USA) with 8 g NaOH and topping up with distilled water to 1 L. A clear negative band shift ~80 bp in *kcnv2a* mutants compared to the wildtype 586 bp band was used for genotyping fish carrying one or two mutant alleles of *kcnv2a*.

For *kcnv2b* mutants, the 2 bp deletion identified by sequencing was too small to resolve by a shift in band size and we therefore designed a restriction fragment length polymorphism (RFLP) assay. Following PCR amplification with primers #197 and #198, the DNA was subjected to digestion with the restriction enzyme BstXI by combining 10 µL of template DNA with 2 µL 10X Buffer 3.1 (NEB), 1 µL BstXI restriction enzyme (NEB), and 7 µL molecular biology grade water. The reactions were incubated in a 37°C water bath for one hour before being run on a 3% SB gel. Wildtype gel bands for *kcnv2b* were 350 bp in size. The BstXI restriction enzyme cut the mutant allele amplicon into two fragments of 50 bp and 300 bp. The negative band shift of ~50 bp in samples from homozygous mutant zebrafish was evident following the digest and was used to quickly detect the presence of the relatively small genetic change in *kcnv2b* mutants. Samples from heterozygous fish appeared as two bands of 300 and 350 bp.

kcnv2a; *kcnv2b* double mutant zebrafish were identified through a combination of the two genotyping assays described above. Conveniently, the annealing temperatures for both genes were identical, enabling PCR reactions to take place simultaneously.

2.5 Quantitative PCR

Eyes dissected from 5 dpf *kcnv2b* homozygous mutant and control fish were collected in RNAlater (Ambion Inc., Austin, USA) in three pools of 50 eyes each. Total RNA was extracted from the tissue using an RNeasy Mini Kit (Qiagen) as directed by the manufacturer. Tissue samples were homogenized with a motorized pestle in 600 µL of Buffer RLT with 1% β-mercaptoethanol (Sigma) and run through an on-column DNAse digestion using DNAse I (Qiagen). RNA was eluted in 32 µL of molecular biology grade water and the concentration determined on an Agilent 2100 Bioanalyzer (Agilent Technologies, Santa Clara, USA).

cDNA was synthesized using an AffinityScript QPCR cDNA Synthesis Kit (Agilent Technologies) as per the manufacturer's instructions. Each cDNA reaction contained 350 ng RNA, 10 µL of 2X first strand master mix, 1.7 µL of oligo(dT) primers, 0.3 µL of random primers, and topped up to 20 µL with molecular biology grade water. The cDNA was diluted to a V_{10} working concentration for qPCR experiments.

qPCR experiments were performed on a 7500 Real-Time PCR system (Applied Biosystems Inc., Foster City, USA) following the Minimum Information for Publication of Quantitative Real-Time PCR Experiments (MIQE) guidelines (Bustin et al., 2009). Each reaction contained 2.5 µL 2X QPCR Dynamite Mastermix (MBSU, University of Alberta), 0.5 µL gene-specific primer (5 µM; Table 2.3), and 2 µL V_{10} cDNA. Biological and technical replicates were completed in triplicate. Transcript quantities were measured relative to an endogenous housekeeping gene, *rpl13a*, which was validated through an endogenous stability assay (Figure 2.3 a). Average C_t values were not significantly different between *kcnv2b* and control fish. Primer specificity was confirmed by single peaks on the primer pair disassociation curves (Figure 2.3 b-d). Primers for *rho* and *lws2* were validated previously in an identical manner (Balay, 2018).

Oligo ID	**Sequence (5'-3')**	**Amplicon Length (bp)**	**Primer Efficiency (%)**
kcnv2a #263F	GTCTCTTGTACTGCTGGGATAAA	88	111.37
kcnv2a #263R	AACTGCATCCATCACTGGTAG		
kcnv2b #268F	GTTTAACTTTACTGAATCCTGCTGA	81	93.98
kcnv2b #269R	AACCACATCATTTGGCACTTT		
rho #290F	CCCTGCCCGCCTTCTT	76	98.10
rho #291R	CGGAACTGCTTGTTCATGCA		
lws2 #245F	TGCGATGCAATGCTGTTATTC	123	101.84
lws2 #246R	GCTCTGTGACAACAACAATACG		
rpl13a #294F	CGCCACACTGGAGGAGAAGA	82	98.024
rpl13a #295R	CTGCTTAGTCAGCTTCATCTCAACTT		

Table 2.3 – Primers used for qPCR in *kcnv2b* mutant zebrafish. Primers were designed to target the 3' end of each gene. Efficiencies scored were calculated from the slope of the standard curve for each primer set. Scores between 90-110% fell within the acceptable range (Ginzinger,

2002). All primers were ordered through Integrated DNA Technologies with standard desalting purification.

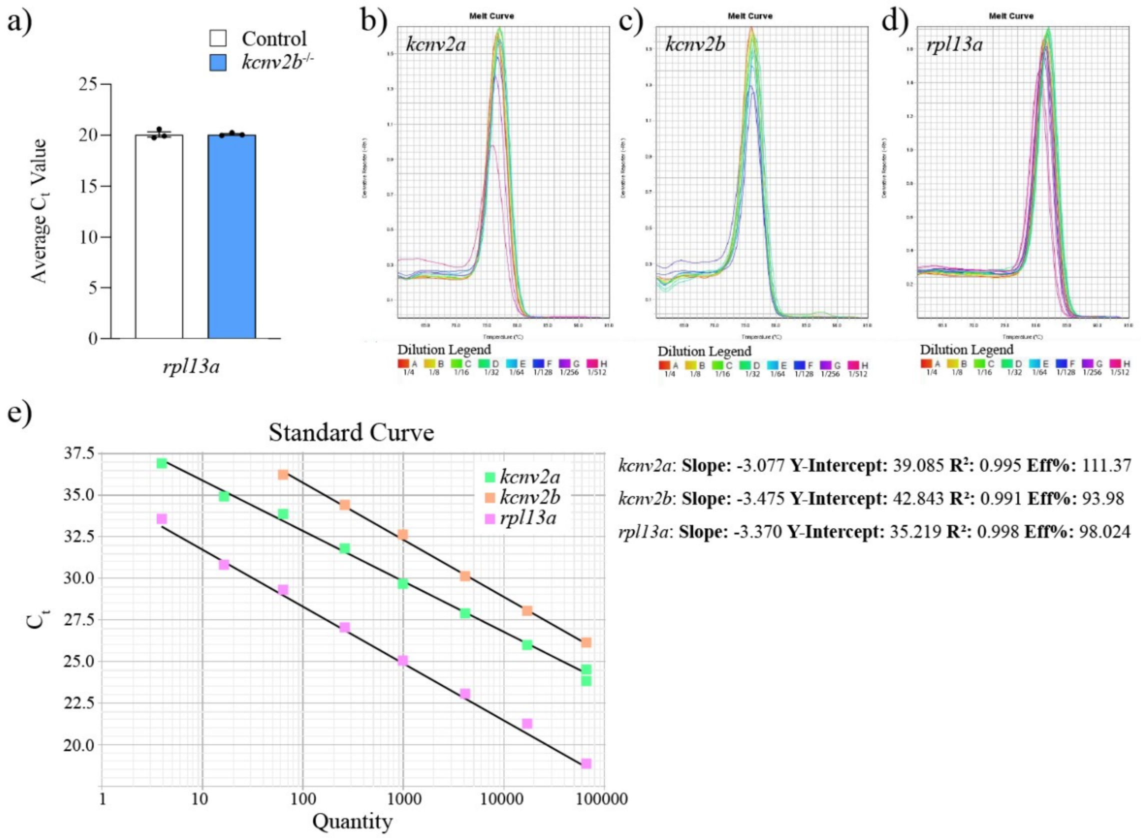

Figure 2.3 – Validation of *kcnv2* qPCR primers. a) Average cycle threshold (C_t) values of *rpl13a* did not significantly differ between 5 dpf control and *kcnv2b* mutant eyes (n=3 samples, 50 ea.; p=0.9758). b-d) Melt curve analysis of *kcnv2a*, *kcnv2b*, and *rpl13a* primer sets to ensure specificity. Biological and technical replicates were tested in triplicate. e) Standard curves and characteristics for each primer set. Primers for *rho* and *lws2* were validated previously (Balay, 2018). Primer sequence can be found in Table 2.3. Error bars are SEM. C_t, cycle threshold.

2.6 Antibody Design

Custom monospecific primary antibodies were designed to investigate the expression patterns of K$_V$8.2a and K$_V$8.2b. Four antibodies were designed in total: two targeted the protein product of *kcnv2a* (K$_V$8.2a Ab1 and K$_V$8.2a Ab2) and two targeted the protein product of *kcnv2b* (K$_V$8.2b Ab1 and K$_V$8.2b Ab2). Details of the epitope sequence and amino acid location are outlined in Table 2.3. Zebrafish *kcnv2a* and *kcnv2b* DNA sequences obtained from wildtype TL fish at the University of Alberta were referenced to the most recently updated zebrafish genome (GRCz11) to ensure sequence similarity. Predicted amino acid sequences for K$_V$8.2a (ENSDARG00000076644.5) and K$_V$8.2b (ENSDARG00000062906.5) were sent to Pacific Immunology Corporation (Ramona, USA) for epitope selection. Full length protein sequences were run through several predictive algorithms and compared against each other to identify unique regions for specific detection of each protein. Four pairs of rabbits were then inoculated, each pair with one peptide sequence from Table 2.3. Monospecific antibodies were then obtained through periodic bleedings. ELISA was performed for each antibody to ensure positive detection of the epitope. Finally, the rabbit serum was affinity purified before being shipped to our laboratory.

Antibody	Immunogen	Protein Sequence
K$_V$8.2a Ab1	a.a. 11-27 of zebrafish K$_V$8.2a	Cys-YKLGVTVPAPKDPEDSD
K$_V$8.2a Ab2	a.a. 61-76 of zebrafish K$_V$8.2a	Cys-EDRLFSTPSKLSSPVK
K$_V$8.2b Ab1	a.a. 11-22 of zebrafish K$_V$8.2b	CKLANSESTDDI
K$_V$8.2b Ab2	a.a. 59-75 of zebrafish K$_V$8.2b	HAEPTLWFTSTSPSRNC

Table 2.4 – Primary antibody information. Custom monospecific primary antibodies were designed against zebrafish K$_V$8.2a and K$_V$8.2b within a rabbit host. Two antibodies for each protein product were selected to increase the probability of a successful immune reaction.

Epitopes were selected upstream of the CRISPR-Cas9 cut sites and were located on an intracellular portion of the protein. Efforts were made to identify unique epitopes on each protein. Antibodies underwent an ELISA and affinity purification before use.

2.7 SDS-PAGE and Western Blots

Protein was harvested from enucleated zebrafish eyes submerged in RIPA buffer (Boston BioProducts, Ashland, USA) with Halt™ protease and phosphatase inhibitor cocktail (Thermo Fisher) added. The tissue was homogenized with a motorized pestle and then centrifuged at 13 000 rpm for 1 minute. The supernatant was collected before the protein content was determined using a BCA assay (Thermo Fisher) and analysed using a spectrophotometer running ScanIt (AmsterCHEM, Almeria, ESP). Following protein content analysis, 20-50 μg of protein was mixed with 6.6 μL 4X Laemmli sample buffer (Bio-Rad Laboratories, Hercules, USA) and topped up to 20 μL with lysis buffer. The protein samples were loaded into a Mini-PROTEAN TGX precast gel (4-20% gradient; Bio-Rad) submerged in 1X running buffer (10X stock solution is made from 10 g SDS, 30.3 g Tris-Base, and 144.1 g glycine in 800 mL distilled water). 3 μL of Chameleon Duo Pre-Stained Protein Ladder (LI-COR Biosciences, Lincoln, USA) was added to the gel before running at a constant voltage of 100 V for 1-2 hours at room temperature. The protein was then transferred from the gel to a nitrocellulose membrane at 30 V overnight at 4°C.

Western blotting was achieved by first incubating the nitrocellulose in ~6 mL of Odyssey Intercept Blocking Buffer in PBS (LI-COR Biosciences) for 1 hour at room temperature. The $\mathrm{K_V}$8.2a and $\mathrm{K_V}$8.2b primary antibodies were added at a 1:1000 dilution and a β-actin primary antibody (mouse host) was used as a control at a 1:6000 dilution. The primary antibodies were diluted in a solution containing 50:50 blocking buffer: PBS with 0.5% Tween (PBST) and left to incubate overnight at 4°C. The membrane was then washed for 5 minutes with PBST three times before adding secondary antibodies and incubating for 60-90 minutes at room temperature on a shaker. The secondary antibodies (α-mouse with a 680 nm-conjugated fluorophore and α-rabbit with an 800 nm-conjugated fluorophore (LI-COR Biosciences)) were diluted 1:10000 in a solution containing 50:50 blocking buffer: PBST. The membrane was then washed for 10 minutes with PBST twice before a final wash with PBS for 10 minutes. The treated membranes were then scanned on an Odyssey CLX system (LI-COR Biosciences).

2.8 Paraffin Embedding and Sectioning

30 dpf and 5 mpf zebrafish were euthanized in concentrated tricane mesylate (TMS; see protocol in Chapter 3) before fixation in neutral buffered formalin for 72 hours. 5 mpf zebrafish were decapitated prior to fixation. To aid in positioning the small larvae in paraffin wax blocks, whole 5 dpf larvae were first embedded in agarose and oriented in parallel groups of three. The solidified blocks and adult heads were placed in tissue processing cassettes and left in the fixative overnight. The next day, the tissue was put in a Leica Tissue Processor 1020 that serially dehydrated the samples in ethanol of increasing concentrations (50, 70, 90, & 100%). Samples were then introduced to toluene first though a 1:1 toluene: ethanol mixture, then through two toluene submersions. Finally, liquid paraffin wax was allowed to penetrate the tissue overnight. Tissue samples were then mounted in paraffin wax blocks and sectioned on a Leica microtome. 5 μm coronal sections halfway through the zebrafish eye were collected on microscope slides (Fisher Scientific, Hampton, USA) and dried overnight in a 37°C incubator. NB: 5 mpf zebrafish sections were difficult to collect due to the development of bony facial structures. In the future, a decalcification step should be performed to collect higher quality wax sections.

2.9 Hematoxylin and Eosin Staining

Residual wax was removed from the tissue sections with two 5-minute washes of toluene before serial rehydration through 2-minute steps of decreasing concentrations of ethanol (100, 90, 70, and 50%) and distilled water. Slides were submerged in hematoxylin Gill III (Leica Biosystems) for 2 minutes, then rinsed in cold tap water for 15 minutes. A 2-minute submersion in 70% ethanol was used to prepare the slides for a 30 second exposure to eosin (Leica Biosystems). Following this, the eosin was removed with two 100% ethanol washes before a final toluene wash. Slides were kept in toluene to avoid dehydration while coverslipping with DPX mounting media (Electron Microscopy Sciences, Hatfield, USA). The mounting media was allowed to dry on the stained slides in a 37°C oven overnight before microscopic examination.

2.10 Image Acquisition and Analysis

Hematoxylin and eosin stained tissue was imaged with a SeBaCam camera (Laxco Inc., Mill Creek, WA) mounted to a Zeiss Axioscope.A1. Images were collected at 10X, 20X, 40X, and 63X magnifications. Image processing was performed using SeBaView software (Version 3.7.11605 for Windows; Laxco Inc.). Retinal layer thicknesses were measured using FIJI image processing software (Schindelin et al., 2012). Figures were assembled using Adobe Illustrator (Adobe Inc., San Jose, USA).

2.11 Optical Coherence Tomography

30 dpf, 60 dpf, 5 mpf, and 12 mpf zebrafish were anesthetized in 4.2% TMS before being placed in a plastic petri dish with the right eye facing upwards. 30 dpf fish were positioned for the test by first being covered in 1% low melting point agarose, before transfer to the testing platform. Older fish (60 dpf, 5 mpf, and 12 mpf) fish were large enough to secure directly in place on the

testing platform with a strip of damp gauze. Zebrafish were then covered in 2% TMS diluted in aquatics facility water for the duration of the procedure to ensure continued sedation. A handheld Envisu R-Series OCT (Bioptigen Inc., Durham, USA) was mounted above the subject and InVivoVue 2.4 OCT Management Software (Bioptigen Inc.) was used to acquire and analyze images. Following image acquisition, zebrafish were either returned to aquatics facility water and resuscitated or euthanized in concentrated TMS for tissue processing.

2.13 Statistics

Statistical tests and boxplots were generated through GraphPad Prism (Version 8.4.3 for Windows, GraphPad Software, San Diego, CA). All data sets were screened for a Gaussian distribution using the Shapiro-Wilk test (Ghasemi & Zahediasl, 2012). Data sets determined to have a normal distribution were compared using a parametric t-test. In the few data sets that did not meet the statistical threshold for normality, non-parametric Mann-Whitney tests were used to compare between groups.

CHAPTER 3: ELECTRORETINOGRAM ANALYSIS OF ZEBRAFISH RETINAL FUNCTION ACROSS DEVELOPMENT

Nathan J. Nadolski[1], Casey X.L. Wong[2,3,5], Jennifer C. Hocking[1,3,4,5,†]

[1]Department of Medical Genetics, University of Alberta, Edmonton, Alberta, Canada

[2]Department of Biological Sciences, University of Alberta, Edmonton, Alberta, Canada

[3]Women and Children's Health Research Institute, University of Alberta, Edmonton, Alberta, Canada

[4]Department of Cell Biology, University of Alberta, Edmonton, Alberta, Canada

[5]Division of Anatomy, Department of Surgery, University of Alberta, Edmonton, Alberta, Canada

This chapter is modified from a manuscript of the same title that was published in Documenta Ophthalmologica on July 20, 2020 with permission from Springer Nature Publishing under license number 4906711105892.

3.1 Introduction

Only a handful of laboratories have successfully performed ERGs on zebrafish, each with their own technical approach. Most published protocols rely on the construction of a delicate fluid-filled micropipette to house the recording electrode (Fleisch et al., 2008; Saszik & Bilotta, 1999). Although this approach produces high-quality ERG waveforms, these apparatuses require special storage and careful handling so as not to break the glass micropipette or introduce a fluid leak. A recent advance in the zebrafish ERG recording technique has attempted to simplify the approach by using a moistened cone-shaped sponge fitted over a silver wire recording electrode (Xie et al., 2019). While removing the need for the fragile glass micropipette sheath, the coarse sponge tip reduces the precision of the recording electrode placement.

This section is a description of a simple and universal ERG apparatus for use on zebrafish of all developmental stages – larval (7 days-post-fertilization [dpf]), juvenile (1 month-post-fertilization [mpf]), and adult (4 mpf). This approach aimed to make ERGs more accessible by use of a novel 3D-printed platform for precise electrode placement and a simplified electrode fabrication method. The 3D model can be manipulated to each laboratory's specifications, e.g., adjustment of the micromanipulator holding arm thickness or overall scale. The 3D-printed system allows for careful, consistent, and gentle placement of the recording electrode on the centre of the cornea, all of which are necessary for high-quality ERG recordings.

Similar to the cone-shaped recording electrode previously described by Xie *et al.* (2019), the electrode used here consisted of a platinum electrical lead wire intertwined with a length of thin, chlorided silver wire. This approach further simplifies the electrode by removing the insulative tape and the cone-shaped sponge-tip. The presence of the sponge tip was found to hinder overall experimental efficiency by reducing electrode placement accuracy. The bare silver tip allowed for precise positioning of the recording electrode on the cornea and did not introduce a significantly disruptive photovoltaic artifact.

This protocol outlines a simple and effective approach to obtaining electroretinographic measurements from the zebrafish retina at all major developmental stages, a feature not commonly reported in the literature (Sun et al., 2018). Notably, canonical OPs can be isolated from the generated waveform, establishing the first instance of such analysis in the zebrafish electrophysiology community. Additionally, this approach to ERG recordings in juvenile and adult zebrafish resulted in a high survival rate following the test. This is particularly useful for the study of progressive ocular diseases, such as retinitis pigmentosa and glaucoma, because it permitted re-testing of individual fish across development.

3.2 Materials

Zebrafish Maintenance and Husbandry

Tüpfel long-fin (TL) wildtype zebrafish were cared for according to standard protocols, with animal ethics protocols approved by the University of Alberta Biosciences Animal Care Committee (AUP1476). Embryos and larvae were grown in embryo media at 28.5°C until 5 dpf before being transferred to an aquatics facility and grown under 14:10 hour light/dark conditions.

Software

Figures in this manuscript were created with Adobe Illustrator (Adobe Inc.). Supplementary File 1 was created with Google SketchUp (Google Inc., Mountain View, USA). Statistical testing was performed with GraphPad Prism 8 (GraphPad Software). Oscillatory potentials were isolated from waveforms using MATLAB (MathWorks Inc., Natick, USA).

Reagents

- Embryo media
- Tricane mesylate (TMS) anesthetic (Acros Organics, Geel, BEL) – preparation outlined below
- Household bleach (5.25%) (Clorox; Oakland, USA)

Equipment

- E3 Electrophysiology System (Diagnosys LLC, Lowell, USA)
- ColorDome Ganzfeld light stimulator (Diagnosys LLC, Lowell, USA)
- Surgical microscope – PN: 6627502701 (Carl Zeiss, Jena, DEU)
- Red-coloured plastic transparency sheets
- Micromanipulator (Narishige International USA Inc., Amityville, USA)
- Polyvinyl alcohol (PVA) sponge
- Platinum lead electrodes (Natus Medical Inc., Pleasant, USA)
- 32-gauge silver wire (Evonik Ind., Essen, DEU)
- Silver/Silver chloride reference electrode – PN: EP08 (World Precision Instruments Inc., Sarasota, USA)
- Filter paper (Whatman, Maidstone, GBR)

3.3 Protocol

3D Printing

1. Download the ERG Platform (Figure 3.1 b) .stl file from Supplemental File 1 accessed through the original article in *Documenta Ophthalmologica*.
2. (Optional) Alter the dimensions of the model with your choice of 3D software – e.g., Google SketchUp.
3. Print the .stl file on an appropriate 3D printer. A Prusa MK2 3D printer was used here, but the .stl file type is a common file format for most 3D printers.

Electrode Preparation

1. Begin preparing the recording electrode by removing 2 cm of insulative housing from a platinum electrical lead wire designed to fit your ERG recording system. A Diagnosys E3 System paired with a ColorDome Ganzfeld light stimulator was used here.
2. Intertwine the exposed platinum with a 4 cm length of 32-gauge silver wire and connect the two securely (Figure 3.1 a).
3. Use 600 grit sandpaper to clean the silver wire until it shines metallically.
4. Prepare the reference electrode in a similar manner, but do not sand as the silver chloride layer is very fragile. Note that this method uses a commercially available silver/silver chloride reference electrode with a thick, but brittle silver chloride layer. In-house reference electrodes can also be fabricated in a similar fashion as the recording electrodes.
5. To increase electrode conductivity, submerge both the recording and the reference electrode into household bleach for 5 minutes. Take care to only submerge the distal silver and not the platinum, as this will result in corrosion and performance loss.
6. Let the electrodes air dry for 3 minutes on paper towel before mounting in a truncated plastic Pasteur pipette. A slice down the side of the pipette allows the electrode to enter at a lower point, reducing the overall wire length (Figure 3.1 c).
7. Ground the system by connecting a platinum electrical lead wire to a nearby metal surface.

TMS Anesthetic Preparation

1. Prepare a stock solution by dissolving 400 mg of tricaine powder (CAS number: 886-86-2) into 97.9 mL distilled water.

2. Add 2.1 mL 1M Tris pH 9 and adjust the pH of the solution to 7.
3. Prepare a 4.2% working solution by diluting 4.2 mL stock TMS with 95.8 mL distilled water.
4. Store the concentrated stock solution at -20°C and the working solution at 4°C.

Testing Platform Assembly

1. Securely attach the micromanipulator to the holding arm, ensuring an appropriate approach angle for the recording electrode.
2. Slide the truncated pipette containing the recording electrode into the micromanipulator.
3. Use a soldering iron to melt a slot for the reference electrode in the side of a 35 mm petri dish and position it in the designated well on the platform.
4. Lay the reference electrode on the bottom of the 35 mm dish and secure the electrical lead wire to the platform using adhesive tape.
5. Using a utility knife, cut a section of PVA sponge to fit within the 35 mm petri dish. Soak this sponge in anesthetic and gently place on top of the reference electrode in the petri dish. The sponge should be just saturated, not dry to the touch or dripping wet (Figure 3.1 c).

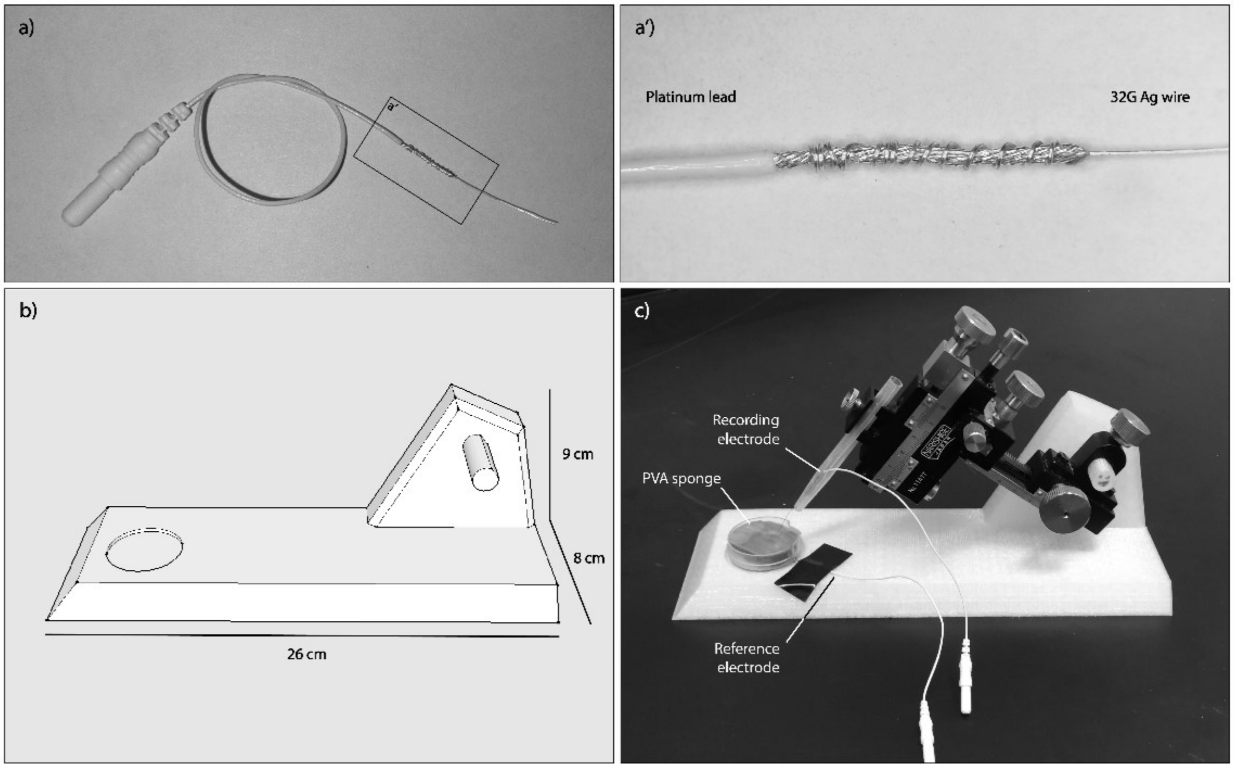

Figure 3.1 – Electrode and testing platform assembly. a) The recording electrode is constructed easily by intertwining a platinum electrical lead wire with 32-gauge silver wire. a') The inlay gives a closer look at the junction. b) 3D render of the testing platform with current dimensions. c) Assembled testing platform including all necessary components for ERG testing.

Larval Zebrafish Testing

1. Using a glass pipette, draw up a single larval zebrafish and place it in a 35 mm petri dish filled with 4.2% TMS for 1 minute.
2. Transfer the fish to a 1 cm x 1 cm piece of filter paper and use forceps to position the fish on its side with one eye pointed upwards.
3. Using forceps, shuttle the filter paper to the testing platform and place on the moistened sponge.

4. Use the micromanipulator aided by a surgical microscope to position the tip of the recording electrode gently on the centre of the cornea (Figure 3.2 a).
5. Insert the prepared testing platform into the Ganzfeld light stimulator and begin the desired testing procedure.
6. Following the test, draw back the recording electrode and use forceps to transfer the filter paper and fish to a petri dish filled with concentrated TMS for euthanasia. Larval test subjects were not maintained because it is relatively simple to obtain 7 dpf zebrafish.

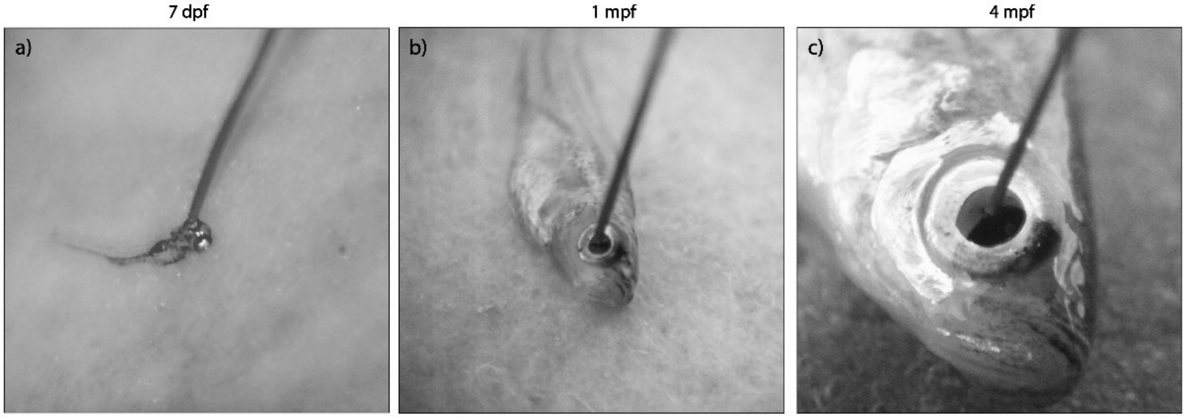

Figure 3.2 – Corneal electrode placement on larval, juvenile, and adult zebrafish. Careful and gentle placement of the recording electrode is essential to obtaining quality ERG traces. Central placement of the recording electrode is shown on a) larval, b) juvenile, and c) adult zebrafish corneas. Note that the magnification of these images is unchanged, highlighting the difficulty in accurate electrode placement on larval fish.

Juvenile & Adult Zebrafish Testing

1. Net a single fish and transfer into a small beaker containing 4.2% TMS. Leave the fish in anesthetic until opercular movements cease (between 2-3 minutes).
2. Use a plastic spoon to transfer the fish directly to the moistened sponge and position the fish on its side with one eye pointed upwards.

3. Follow steps 4 & 5 from the larval zebrafish testing protocol (Figure 3.2 b-c).
4. Following the test, draw back the recording electrode and use a plastic spoon to transfer the fish into a recovery tank.
5. To increase the rate of survival, use a 1 mL syringe to gently pump water past the gills until the fish regains normal swimming behaviour.

Electroretinogram Recording

1. Settings for each electroretinogram recording apparatus will vary; however, the following were used for this system:
    - Dark adapted series of 0.2, 1, and 10 cd·s/m^2, each step consisting of an average of 5 single flashes of white light separated by 5 000 ms.
    - Light adapted flash of 10 cd·s/m^2, also generating an average output of 5 single flashes of white light separated by 5 000 ms.
    - A band-pass filter of 0.3-300 Hz was applied to reduce system noise.

Analysis

1. Each individual waveform was assessed for quality with overt noisy signals being removed so as not to distort the average signal.
2. Waveforms were measured using the software provided with the Diagnosys E3 system as per the 2015 International Society for Clinical Electrophysiology of Vision (ISCEV) Standards. The a-wave amplitude was measured as the absolute value between the baseline and trough of the a-wave, while the b-wave amplitude was measured from the trough of the a-wave to the peak of the b-wave (McCulloch et al., 2015). If the a-wave was absent, as is often the case under scotopic conditions, the b-wave can be measured from the baseline.

3. Measurements were subject to statistical testing using GraphPad Prism 8

Oscillatory Potential Analysis

1. OPs were isolated from waveforms using MATLAB software (R2020a Update) as previously described (Gauthier et al., 2019).
2. A Butterworth filter was applied with the following variables: Order parameter (N) = 2; Bandpass filter (Wn) = [0.15,0.4] (75 Hz – 200 Hz).

Troubleshooting

Problem 1: Noisy high-frequency baseline when recording electrode contacts cornea.

Solution 1: The electrode may be over-chlorided. Sand the silver wire and re-chloride for 5 minutes. Ensure both the recording and reference electrodes have been chlorided. Also ensure the system is properly grounded.

Problem 2: Absent or very small ERG response.

Solution 2: Recording electrodes can corrode over time. Construct a new electrode every few recording sessions to avoid signal attenuation.

Problem 3: Large variation in waveform amplitude within a group.

Solution 3: Ensure the recording electrode is positioned consistently on the centre of the cornea. Placement on the side of the eye will distort the overall waveform and may result in amplitude fluctuation between subjects.

Problem 4: Large spike in either direction at t=0 following the stimuli (photoelectric effect).

Solution 4: Stimulus intensity directly affects both the size and direction of the artefact. Ensure the stimulus intensity is within the range documented here.

3.4 Representative Results

To showcase the utility of our ERG system, wildtype TL zebrafish were tested at three developmental timepoints – larval (7 dpf), juvenile (1 mpf), and adult (4 mpf). The zebrafish were tested under both scotopic (dark adapted) and photopic (light adapted) conditions using the protocols outlined above. As per the 2015 ISCEV Standards for human recordings (McCulloch et al., 2015), fish were adapted to a dark environment for at least 20 minutes before testing. While 20 minutes was found to be sufficient to generate rod responses, it should be noted that there is no accepted minimum time for dark adaptation of zebrafish, and a broad range has been used in the literature (Fleisch et al., 2008; Seeliger et al., 2002; Xie et al., 2019). Dark adapted tests were performed under dim red illumination provided by either red light bulbs or red transparency film fitted over light sources such as the computer screen. Following scotopic tests, light adapted tests commenced after a 10-minute exposure to a rod-desensitizing 30 $cd \cdot s/m^2$ ambient light intensity. Both scotopic and photopic adaptation intervals were achieved using the ambient room lighting while fish were still swimming in a holding tank. This minimized the time out of water, which may have negatively affected ERG quality. Although the a-wave is a measurable feature in these waveforms, my analysis focuses primarily on the b-wave as it is the largest and most frequently assessed component of the ERG. If desired, pharmacological blockage of the b-wave with compounds such as 2-amino-phosphonobutyric acid (APB) and threo-β-benzyloxyaspartic acid (TBOA) have been shown to help resolve the often overshadowed a-wave (Demarco & Powers, 1989; Jardon et al., 1989; Nelson & Singla, 2009; Seeliger et al., 2002; Wong et al., 2004).

3.4.1 Scotopic ERG Recordings Illustrate a Developing Rod System

Assessing the rod system of the retina is achieved by dark-adapting the subject before testing. The dimmest flash initiates the intensity ramp and only activates the highly sensitive rods.

Brighter intensities evoke a cumulative response from both the rod and cone systems. These data show that the dark-adapted ERG output of zebrafish increases as they mature to adulthood. This is manifested as a gradual growth of the b-wave component of the waveform as the subject develops (Figure 3.3). Of note is the relatively undistinguishable ERG waveform elicited by the dimmest stimulus of 0.2 cd·s/m^2 in 7 dpf fish. This finding reflects the inability of the underdeveloped rod system of larval zebrafish to functionally contribute to the ERG until 15 dpf (Branchek, 1984). In all three age groups, ERG waveforms are generated from higher stimulus intensities, reflecting activation of the retinal cone system (Figure 3.3 a-c). Juvenile and adult zebrafish exhibit an increase in b-wave amplitude across the intensity ramp with an overall amplitude increase as the fish matured (Figure 3.3 b-d).

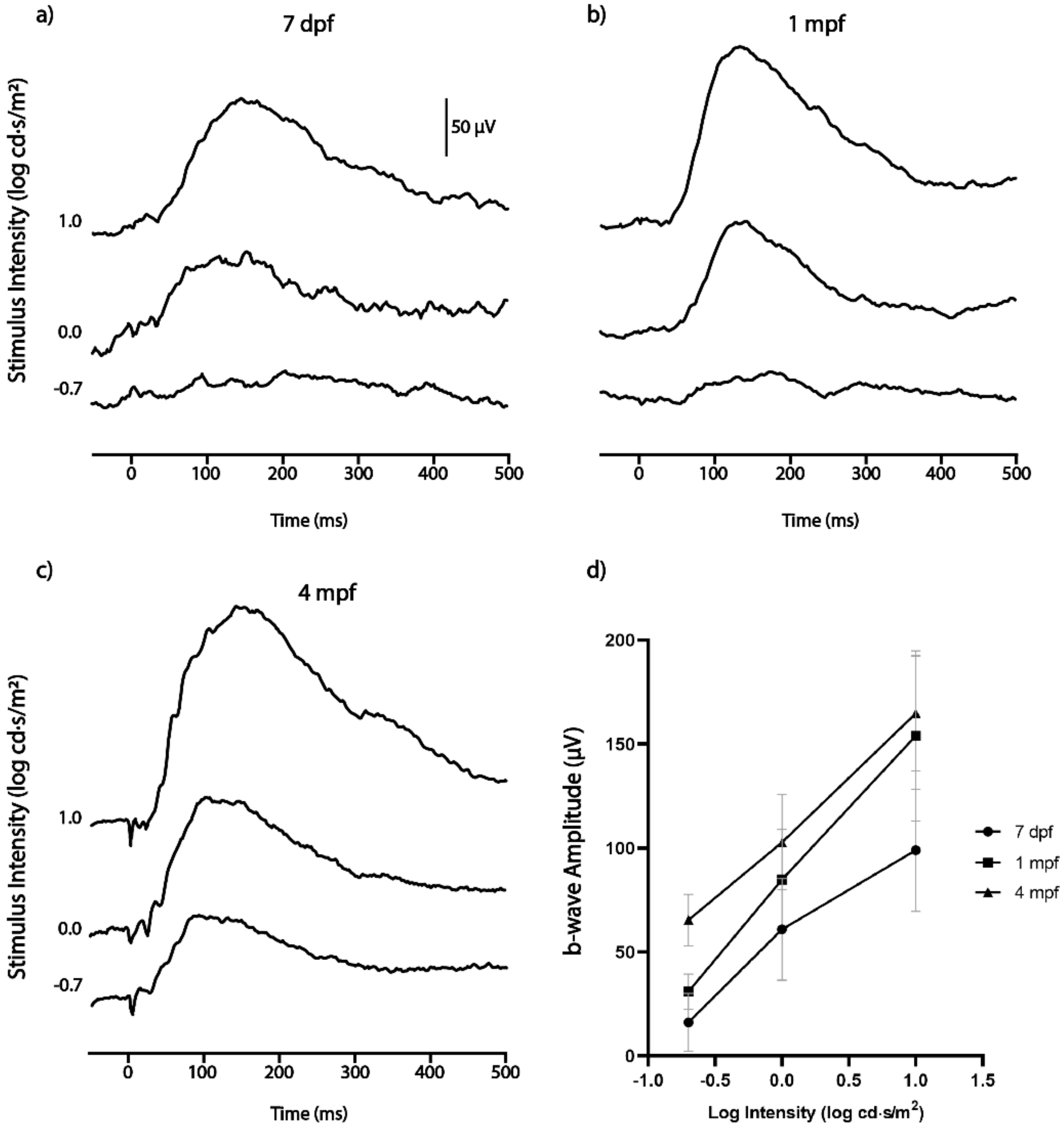

Figure 3.3 – Age differences in scotopic ERG waveforms of larval, juvenile, and adult zebrafish. Representative dark-adapted ERG waveforms elicited by an intensity ramp of -0.7, 0.0, and 1.0 log cd·s/m^2 (0.2, 1, and 10 cd·s/m^2, respectively) in a) larval, b) juvenile, and c) adult zebrafish. Each waveform is an average of five stimuli. d) Scotopic b-wave intensity

response function across development. n=15 for 7 dpf, n=10 for 1 mpf, n=10 for 4 mpf. Error bars are SD.

3.4.2 Photopic ERG Waveforms Indicate Cone System Growth Across the Lifespan

Investigation of the retinal cone system was performed by light-adapting the zebrafish prior to the ERG recordings. Light adaptation desensitizes the rods, resulting in a waveform exclusively produced by cones. White light was used in this experiment to trigger all subtypes of zebrafish cones (red, green, blue, and UV), but it should be noted that stimulus wavelength can be manipulated to activate a specific sub-population if desired. Robust ERG waveforms were observed from each developmental timepoint (Figure 3.4). Light-adapted ERG responses collected from zebrafish presented as having a reduced time-to-peak and an overall 'sharper' profile than scotopic responses at each developmental timepoint. A subtle b-wave amplitude increase only later in development was observed (Figure 3.4 d), which may reflect the faster early development of cones relative to rods (Branchek, 1984).

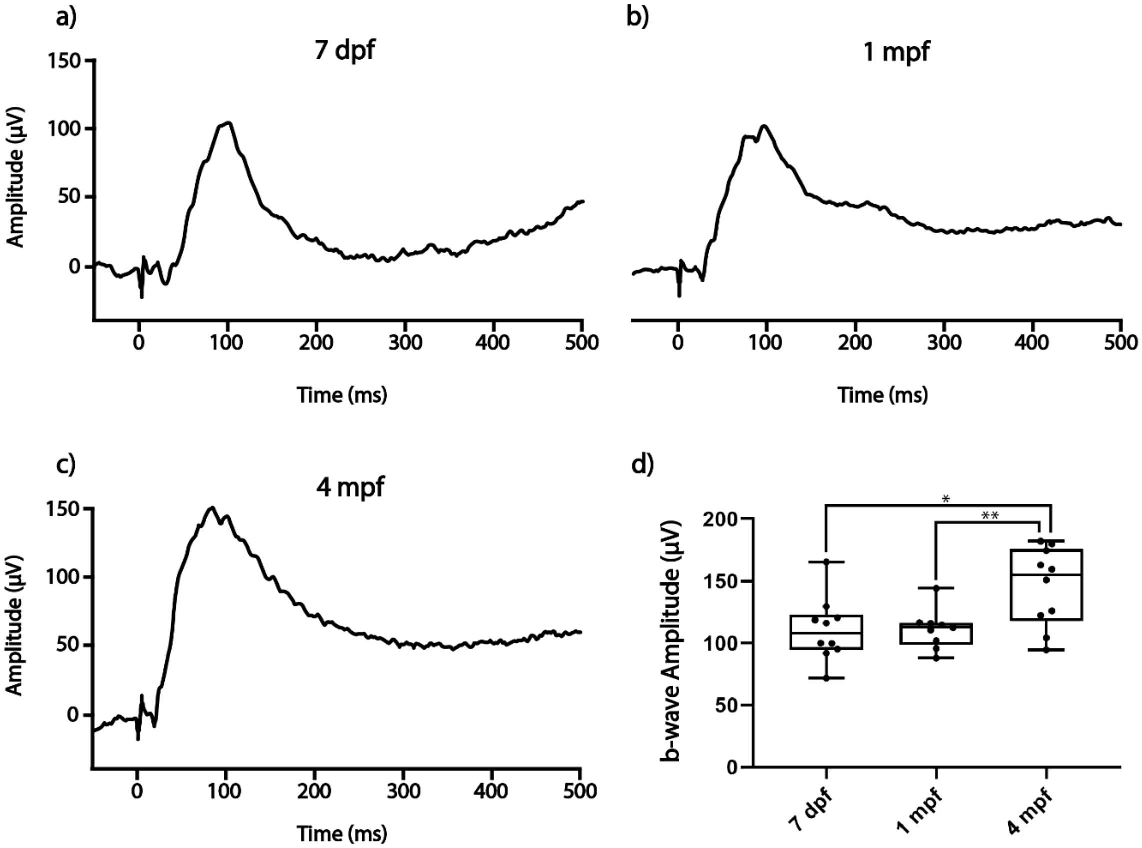

Figure 3.4 – Photopic ERG waveforms from larval, juvenile, and adult zebrafish. Representative light-adapted ERG waveforms elicited by an intensity of 10 cd·s/m^2 in a) larval, b) juvenile, and c) adult zebrafish. Each waveform is an average of five stimuli. d) Photopic b-wave amplitude across development. Boxes extend from the 25-75% percentiles, internal lines represent the median, and whiskers complete the range. n=10 fish per age group. *P<0.05; **P<0.01.

3.4.3 Oscillatory Potentials can be Isolated from ERG Waveforms

Post-processing software can be used to isolate the subtle OPs from the dominant a- and b-waves as previously described for human traces (Gauthier et al., 2019). There are many digital filters that can be applied to the ERG waveforms to isolate OPs, but the Butterworth filter was chosen as it has been shown to consistently produce high-frequency OPs. Other filters such as the Bessel and Chebyshev type 1 filters are also appropriate and isolate OPs with slightly different characteristics (Gauthier et al., 2019).

Application of the filter removes the slow frequency a- and b-waves that often obscure the small OPs. Once filtered out, multiple measurable OPs wavelets can be clearly distinguished from background noise (Figure 3.5). While not all waveforms produced robust OPs, dim scotopic and bright photopic conditions yielded the most consistent OPs. Though the interpretation of OP signal variance is still up for debate, diseases such as diabetic retinopathy are hallmarked by changes to this subtle ERG component (Kizawa et al., 2006) and further add to the utility of the ERG method described here.

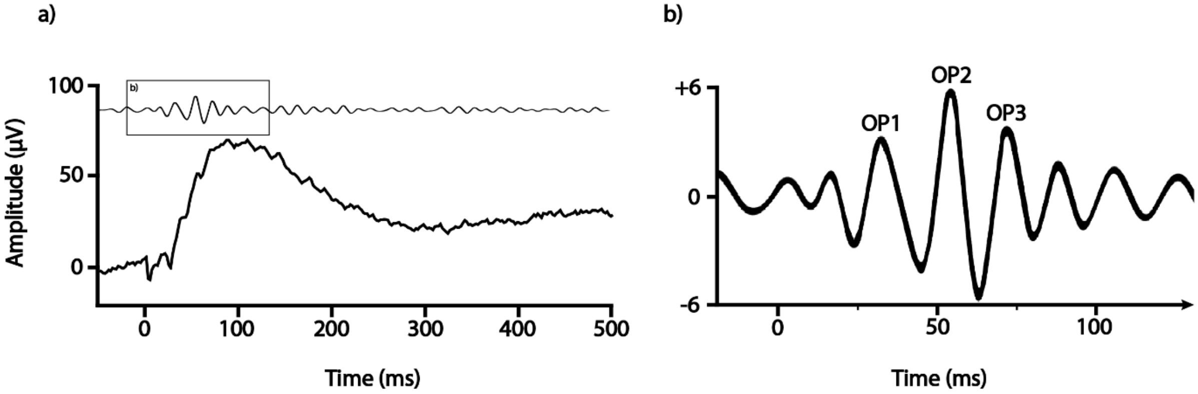

Figure 3.5 – Oscillatory potentials can be isolated from ERG waveforms. Post-processing software was applied to a sample waveform to filter out the slow a- and b- waves. a) Bottom: the pre-filtered waveform from a 4 mpf fish elicited by a 0.2 cd·s/m^2 scotopic stimuli. Indications of OPs can be seen on the ascending limb of the b-wave. Top: the post-filter signal of 75 Hz – 200 Hz reveals OPs corresponding to the ripples below. b) a magnified view of the OPs designating wavelets as OP1, OP2, and OP3.

3.4.4 Stability of Response over Recording Period

One of the challenges of performing ERGs in zebrafish is simply their aquatic habitat, from which the fish must be temporarily removed for recording. Importantly, workflow was optimized in this procedure to minimize the time spent out of the water and have in fact observed >95% survival post recording. Further, note that the ERG waveform is consistent from the first flash of a given stimulus intensity to the fifth and final flash within each cohort (Figure 3.6), which suggests that corneal drying does not skew the average waveform shape.

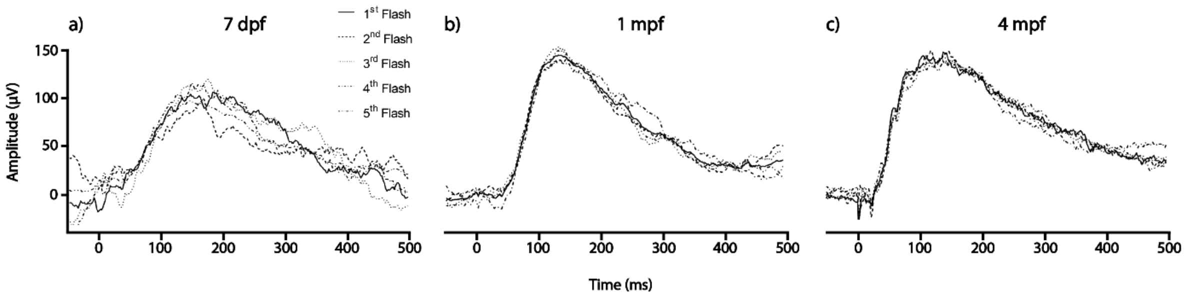

Figure 3.6 – Serial waveform shape across the testing duration of a given stimuli. Individual waveforms resulting from the five individual dark adapted 10 cd·s/m^2 stimuli are superimposed for a) 7 dpf, b) 1 mpf, and c) 4 mpf fish. Each panel is a representative output series for the respective age group. These five waveforms are the basis for the average ERG output for each fish.

3.5 Discussion

This approach represents a simplified and effective method for obtaining ERG recordings in zebrafish at various developmental timepoints. Aside from generating the hallmark a- and b-waves of typical ERGs, this methodology also produces waveforms that can be filtered to reveal subtle changes in OPs. To our knowledge, this is the first instance of OP wavelet isolation from a zebrafish ERG waveform.

Using this protocol, an overall increase in ERG output as subjects aged was observed, reflective of the developing retina. This methodology also records retinal activity from adult zebrafish, a stage that is often not reported. Paired with a high survival rate, this capability facilitates the long-term study of progressive ocular diseases within zebrafish models.

A lack of consistency in experimental set-ups and conditions within the zebrafish ERG community has been previously identified, making data comparisons between groups challenging (Seeliger et al., 2002). The development of accessible, inexpensive, and simple hardware like our 3D printed platform and recording electrode will facilitate the standardization of this methodology within the community.

3.6 Acknowledgements

I would like to thank Dr. Yves Sauvé and Dr. Orson Moritz for sharing their extensive technical skills and knowledge of ERG recordings. I would also like to thank Science Animal Support Services at the University of Alberta for their excellent care of the zebrafish aquatics facility.

CHAPTER 4: CHARACTERIZATION OF *KCNV2* MUTANT ZEBRAFISH

4.1 Introduction

Despite a defined role for Kv8.2 in modifying photovoltage, *KCNV2* retinopathy remains a poorly understood inherited retinal disease. There is no uniform disease manifestation aside from the presence of mutations in the *KCNV2* gene. In general, common *KCNV2* retinopathy electrophysiological features include a reduced and delayed scotopic ERG b-wave that quickly reaches normal/supernormal amplitudes across an intensity series and a severely dystrophic and delayed photopic ERG cone-response (Abdelkader et al., 2020; Michaelides et al., 2005; Robson et al., 2010; Sergouniotis et al., 2012; Vincent et al., 2013; Wissinger et al., 2008; Wu et al., 2006; Zobor et al., 2012). Although the supernormal b-wave was the initial characteristic of *KCNV2* retinopathy, thereby bestowing the name Cone Dystrophy with Supernormal Rod Response (Gouras et al., 1983), subsequent studies have found a variable range of clinical features. Fundoscopy and optical coherence tomography (OCT), common clinical tools for the assessment of retinal structure in *KCNV2* retinopathy, have identified several abnormalities localized to the macula. These include disruption or complete loss of the photoreceptor layer and total retina thinning (Abdelkader et al., 2020; Kiray et al., 2020; Sergouniotis et al., 2012; Vincent et al., 2013; Wissinger et al., 2008; Zobor et al., 2012). Interestingly, abnormalities in the peripheral retina have not been detailed despite the robust scotopic vision deficits observed through ERG assessment. Evidence so far suggests that Kv8.2 functions in both rods and cones (Gayet-Primo et al., 2018), but the two photoreceptor subtypes exhibit very different functional and morphological changes in patients. Therefore, the physiology underlying how non-functional or absent $K_V8.2$ influences photoreceptor dysfunction and morphology is currently unclear.

Animal models serve as a means to investigate the mechanisms of disease pathology. For diseases such as *KCNV2* retinopathy, animal models provide an opportunity to assess clinical features of the disease together with underlying cell biological changes in large subject populations raised under controlled conditions. Insights gained through the investigation of animal models of *KCNV2* retinopathy have tremendous potential to reveal shrouded components of the disease mechanism and may play a critical role in the development of future therapeutic interventions. For these reasons, the development of animal models of *KCNV2* retinopathy is a worthwhile endeavour for the study of this rare disease.

In order to inform health practises, animal models of disease must emulate the human pathology. However, concessions are always made when using animal models, as nothing but the native system itself will ever perfectly recapitulate the physiology of the human system. Therefore, efforts need to be made to select animals that exhibit high levels of similarity to the cell, tissue, or organ affected by the disease of inquiry. For *KCNV2* retinopathy, the prerequisite structure is an animal eye that can imitate both form and function of its human counterpart. Although a mouse model of *KCNV2* retinopathy was recently created (see Section 1.5.4; Hart et al., 2019), the rod-dominated mouse retina is not an ideal system to understand the cone-dominant pathology of the disease. Additionally, only a brief investigation of the histological changes, which may be a key part of the disease, was presented. It is also worthwhile to use a combination of animal models to highlight different components of the complete disease process. We therefore used zebrafish, with its macula-like retina, to create a model of human *KCNV2* retinopathy, which we then examined through both clinical techniques (OCT & ERG) and histological means.

4.2 Mutant Line Validation

4.2.1 HRM Analysis

Zebrafish have two orthologues of *KCNV2*, *kcnv2a* and *kcnv2b*, and we reasoned that an ideal model of KCNV2 retinopathy would require loss-of-function mutations in both genes. In order to confirm DNA cutting and the resulting appearance of CRISPR-induced mutations, pools of injected zebrafish larvae were analyzed by high-resolution melt (HRM) technology.

HRM analysis exploits the electrochemical differences between DNA base pairing by measuring the amount of thermal energy required to separate the double stranded helix of DNA. Strand separation is indirectly measured through an intercalating dye that fluoresces when bound to double stranded DNA. When the hydrogen bonds break and DNA strands separate, the dye dissociates from the double-helix and ceases to fluoresce. The change in fluorescence is measured as the sample temperature is increased incrementally (Słomka et al., 2017). Resulting data points are plotted as ‘melt curves’ such as the ones depicted in Figure 4.1.

Changes to the nucleotide sequence following mutagenesis will cause the HRM melt curves to be shifted or distorted relative to wildtype melt curves. Homozygous deletions reduce the number of total hydrogen bonds holding the two strands of an amplicon together. As a result, the melt curve of a homozygous mutant will be shifted towards lower temperatures relative to wildtype melt curves. Alternatively, melt curves obtained from heterozygous mutations appear distorted and often feature a ‘double-bump’ in the curve. This is due to base mismatching that leads to an unstable heteroduplex with a lower melting threshold than its wildtype counterpart (Słomka et al., 2017).

Zebrafish injected with Cas9 targeted to *kcnv2a* or *kcnv2b* exhibited HRM melt curves that differed from those of their uninjected siblings (Figure 4.1). The shifted melt curves indicated that the particular sgRNAs used for the CRISPR-Cas9 mutagenesis could successfully target the Cas9 endonuclease to the regions of interest, leading to double stranded breaks. Attempts by the cells to repair the cut DNA, thought to be mediated primarily by alternative end-joining (Thyme & Schier, 2016), are often imprecise and can result in single nucleotide polymorphisms, deletions, or insertions. The shifts in HRM curves indicated sequence changes in both *kcnv2* paralogs following CRISPR injection. In the case of *kcnv2a*, all samples from pools of injected embryos displayed distorted curve shapes, suggestive of highly efficient cutting. The remaining injected fish (those not used for HRM analysis) were therefore grown to adulthood as the P0 generation and subsequently bred to wildtype TL fish. Pools of the resulting F1 embryos were analyzed by HRM in order to identify P_0 adults carrying germ-line mutations. gDNA samples that led to deviant HRM curves warranted a more detailed investigation of the sequence variation (see Section 4.2.2).

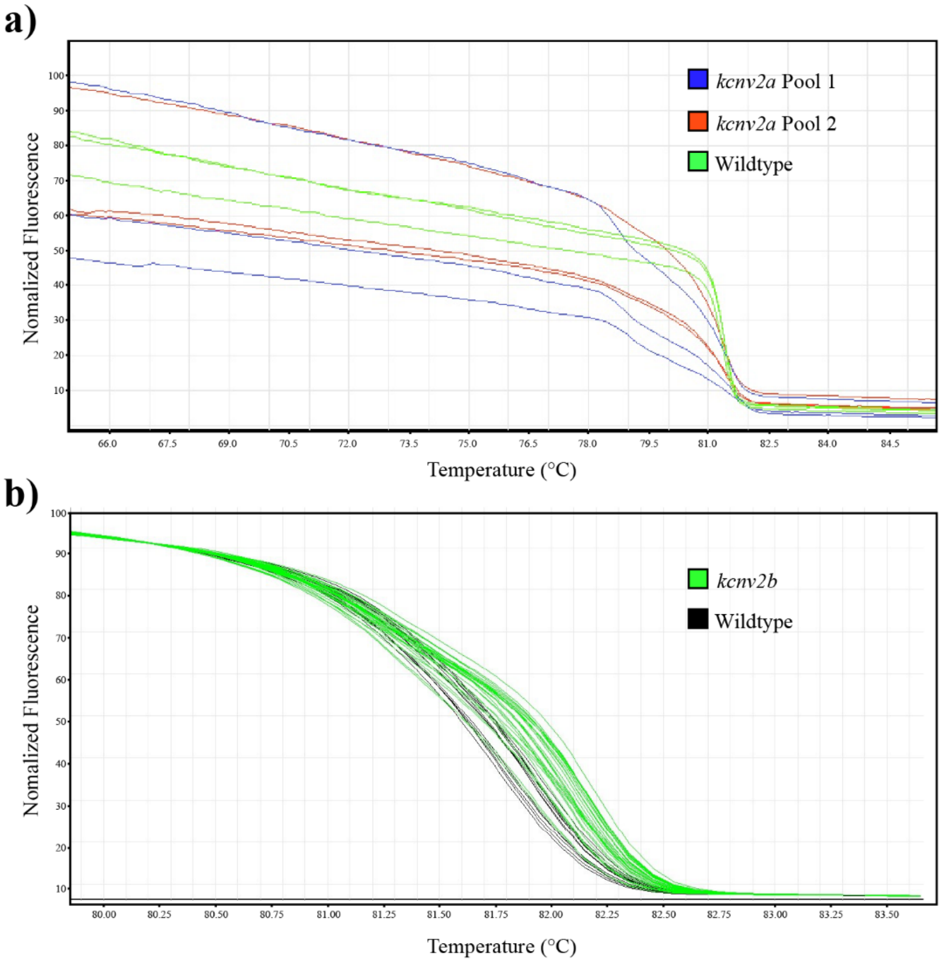

Figure 4.1 – HRM analysis of injected CRISPR zebrafish. Melt curves from a) *kcnv2a* and b) *kcnv2b* CRISPR-Cas9 injected zebrafish. In both cases, melt curves of pools of 10 injected zebrafish display an abnormal shape relative to the sigmoidal curves for control pools.

4.2.2 Sanger Sequencing

While HRM was an efficient tool to identify adult fish carrying germline mutations in *kcnv2a* or *kcnv2b,* it did not reveal the nature of the mutations. Further characterization of the genomic DNA from embryos of the candidate adult P0 fish was accomplished through PCR amplification of the targeted region followed by TOPO cloning and Sanger sequencing. Sequencing provided the exact location and number of nucleotides affected in the mutant zebrafish and allowed for the identification of one fish carrying an 85 bp deletion in *kcnv2a* and another carrying a 2 bp deletion in *kcnv2b* (Figure 4.2 a). As neither of these deletions are multiples of three, which is the length of a codon, they both produced a frameshift mutation in the genetic sequence. Frameshift mutations are particularly valuable in mutant generation due to the high chance of an erroneous and premature stop codon being introduced downstream from the deletion site. Theoretically, the premature stop codon would truncate the protein product and potentially nullify its biological role within the organism. A premature TAG stop codon was located 4 amino acids downstream of the mutation in *kcnv2a* (p.Asp221*) and a TGA stop codon was identified 8 amino acids downstream in *kcnv2b* (p.Cys122*). Figure 4.2 b illustrates both mutation locations transposed onto a schematic of the human K_V8.2 protein product. As noted previously, Cas9 cut sites were targeted upstream of the first TM domain to eliminate the membrane embedding capabilities of K_V8.2a and K_V8.2b.

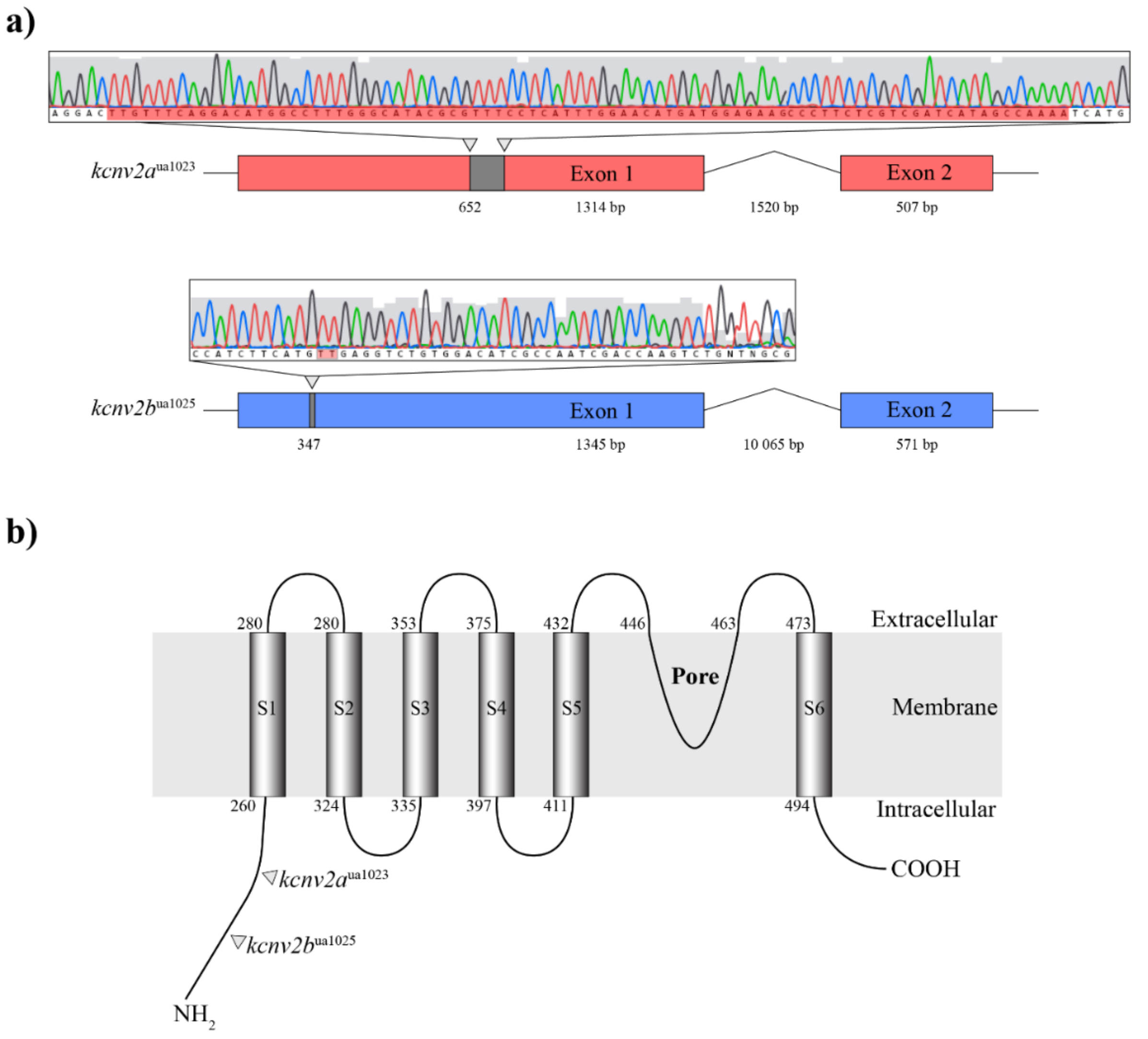

Figure 4.2 – CRISPR-Cas9 induced mutations in the *kcnv2a* and *kcnv2b* genes. a) Illustrations of the nucleotide sequences from regions surrounding the target sites selected for CRISPR-Cas9 mutagenesis. Deleted nucleotides in mutant fish are highlighted in red. An 85 bp and a 2 bp deletion were introduced into the first exon of *kcnv2a* and *kcnv2b*, respectively. b) Deletion locations superimposed onto the human K$_V$8.2. Both deletions were targeted upstream of the first transmembrane domain. Mutations to both genes are predicted to introduce a premature stop codon and lead to a truncated protein product.

4.2.3 PCR Analysis

For *kcnv2a* mutant alleles, a large band shift appeared after running the PCR product on an agarose gel. Wildtype *kcnv2a* amplicons were identified at the predicted size of ~580 bp. Mutant *kcnv2a* bands were located closer to 500 bp, reflective of the 85 bp deletion detected through Sanger sequencing (Figure 4.3 a). Heterozygous *kcnv2a* fish carry both a wildtype and a deletion-containing allele and therefore produced two bands at ~580 and 500 bp, respectively. PCR analysis was used to identify adult F1 zebrafish that were carrying the mutant allele and could then be incrossed to generate a line of homozygous *kcnv2a* mutant zebrafish. As expected, homozygous mutants were identified through PCR genotyping with a single band shifted 85 bp shorter than wildtype *kcnv2a* bands (Figure 4.3 a).

Zebrafish injected with *kcnv2b*-targeted Cas9 were genotyped through an RFLP protocol outlined in Section 2.4.2. The 2 bp deletion created by CRISPR-Cas9 targeting of *kcnv2b* could not reliably be resolved from the 350 bp wildtype band on an agarose gel. Instead, we took advantage of the fact that the 2 bp deletion created a novel cut site for the restriction enzyme, BstXI. PCR amplicons of the wildtype allele produced a band of ~350 bp, which was unchanged following incubation with BstXI. On the other hand, BstXI-digested PCR products from heterozygous *kcnv2b* mutants appeared on the agarose gel as the 350 bp wildtype band plus an additional band at 300 bp representing the truncated mutant amplicon (Figure 4.3 b). *kcnv2b* F1 heterozygotes carrying the 2 bp deletion were bred with one another to generate a homozygous *kcnv2b* line. Homozygous *kcnv2b* zebrafish were identified by BstXI-digested amplicons that appeared on agarose gels as a single band at 300 bp, or ~50 bp shorter than the wildtype *kcnv2b* band (Figure 4.3 b).

Using the two genotyping protocols described above, homozygous *kcnv2a* and *kcnv2b* fish were identified and bred with each other to generate a double heterozygous zebrafish line, *kcnv2a*$^{+/-}$; *kcnv2b*$^{+/-}$. The double heterozygous fish were subsequently identified and incrossed to generate a double homozygous line, *kcnv2a*$^{-/-}$; *kcnv2b*$^{-/-}$. Due to the additional whole genome duplication in teleosts (Glasauer & Neuhauss, 2014), generation of the double mutant line was necessary to best recapitulate the human genotype. Though it is not a perfect genetic match to individuals with *KCNV2* retinopathy, the double knockout zebrafish used in this thesis closely mimics the genetic nature of the human disease.

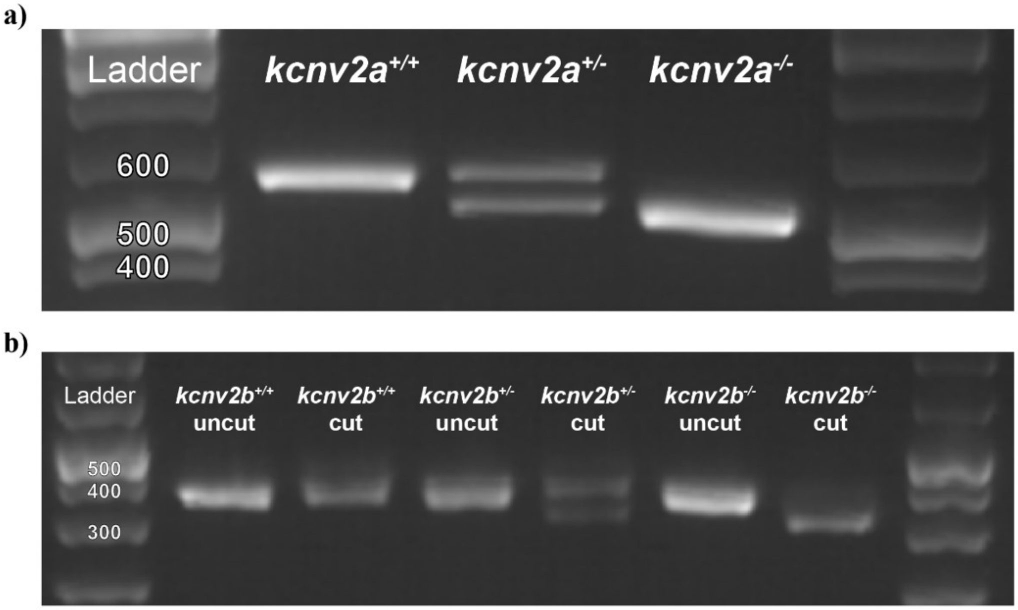

Figure 4.3 – PCR analysis of *kcnv2a* and *kcnv2b* mutant zebrafish. a) Image of 3% SB gel highlighting the 85 bp deletion introduced into *kcnv2a*. b) BstXI restriction enzyme digest of *kcnv2b* PCR products. For both gels, gDNA was obtained from wildtype, heterozygous, and homozygous mutants.

4.2.4 Transcriptional Changes within kcnv2b *Mutant Eyes*

Quantitative PCR (qPCR) was performed on 5 dpf *kcnv2b* homozygous mutants to investigate the effect of the mutation on the levels of *kcnv2* transcripts within the eye. Whole eyes were dissected from 5 dpf *kcnv2b* homozygous single mutants and age-matched control fish and prepared for qPCR experiments as described in Section 2.5. Significant decreases in the levels of *kcnv2b* and *rho* transcripts were detected in *kcnv2b* mutants, while *kcnv2a* and *lws2* transcript levels were unchanged relative to age-matched control fish (Figure 4.4). The reduction in *kcnv2b* transcripts in the mutants indicates that erroneous *kcnv2b* mRNA may be subject to degradation through cellular processes such as nonsense-mediated decay. Conversely, *kcnv2a* transcript levels remain unchanged relative to control fish, revealing no compensatory increase in response to loss of functional K_V8.2b.

rho and *lws2* are genes that encode rod- and red cone-specific opsins, respectively, so changes to opsin transcript quantities can be used as an indirect measure of photoreceptor pathology. The relative reduction in *rho*, but not in *lws2*, suggests a rod-specific pathology at 5 dpf. Interestingly, *kcnv2b* transcripts were not detected in the rod transcriptome (Sun et al., 2018), but were present within the whole eye transcriptome (Nadolski et al., 2020). The nature of the connection between *kcnv2b* mutations and a reduction in *rho* transcription are unclear, but the absence of *kcnv2b* transcripts in rod photoreceptors implies an indirect link. Future qPCR analysis of the recently generated *kcnv2a* homozygous and *kcnv2a*; *kcnv2b* double mutants is needed to more fully explore transcriptional activity within the mutant eye.

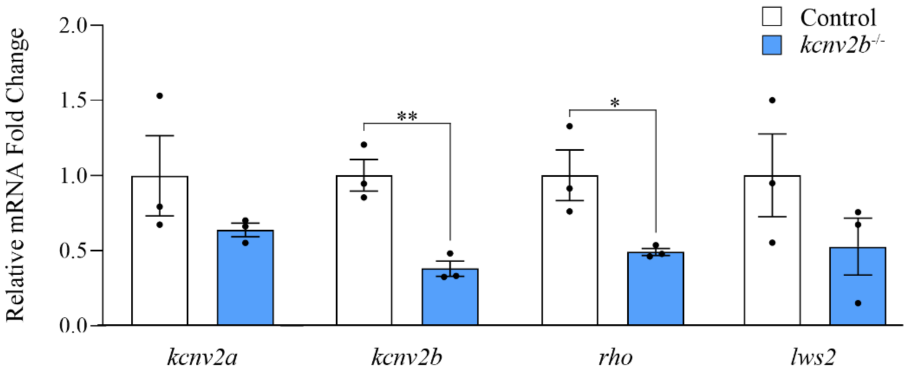

Figure 4.4 – Transcriptional changes in the *kcnv2b*$^{-/-}$ retina. qPCR was performed on pools of 5 dpf *kcnv2b* homozygous mutants and age-matched control fish eyes (50 eyes each). Transcript quantities were compared to a validated endogenous housekeeping gene, *rpl13a*. $^*p<0.05$; $^{**}p<0.01$. Error bars are SEM.

4.2.5 Protein Expression

I performed a series of western blots with monospecific antibodies in an attempt to identify the presence of $K_V8.2a$ and $K_V8.2b$ in wildtype and mutant zebrafish (Figure 4.5). In the mouse, significant Kv8.2 expression was found only in tissues of the heart and eye (Czirjak et al, 2007). We therefore extracted protein from isolated adult eyes to maximize the expected concentration of the proteins in the tissue sample. For each antibody tested, wildtype TL fish and at least one of each homozygous mutant line were included as positive and negative controls, respectively. Blots from all four antibodies produced many bands of variable sizes, indicating a high degree of non-specificity (Figure 4.5). Additionally, zebrafish $K_V8.2a$ and $K_V8.2b$ are expected to be 63 kDa, but no bands of this size were observable in any of the four blots. An antibody for $K_V8.2a$ ($K_V8.2a$ Ab1) produced detectable bands around 57 and 70 kDa, although both bands were consistent across genotypes, including in the *kcnv2a* homozygous mutants (Figure 4.5 a). Likewise, an antibody for $K_V8.2b$ ($K_V8.2b$ Ab1) generated a smaller than expected band at 53 kDa (Figure 4.5 b). Interestingly, this band was diminished in one *kcnv2b* homozygous mutant, but not in a second biological replicate.

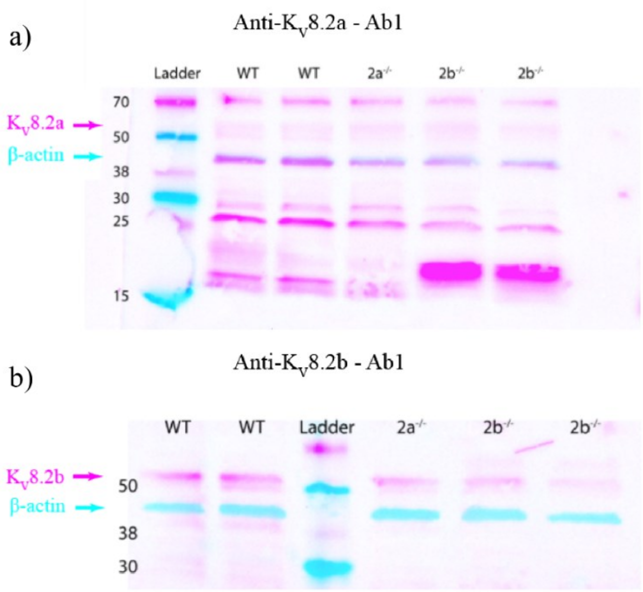

Figure 4.5 – Kv8.2a and Kv8.2b protein identification. Western blot images of proteins extracted from enucleated adult zebrafish eyes probed with an antibody for a) Kv8.2a (Kv8.2a Ab1) and b) Kv8.2b (Kv8.2b Ab1). Wildtype, *kcnv2a*, and *kcnv2b* mutant fish were selected as protein sample donors. β-actin was used as a control antibody in all western blots to ensure similar protein levels were loaded into the gel. β-actin and the presumptive locations of Kv8.2 protein bands are marked as cyan and pink arrows, respectively, on the left of both images.

Early western blots did not definitively identify the presence of Kv8.2a or Kv8.2b; however, the characterization of both proteins in mutant zebrafish remains a central effort for mutant line validation. A variety of factors may have led to the absence of the expected 63 kDa band. First, changes to the protein preparation protocol, specifically to the denaturation boil, may expose the epitope more effectively and facilitate the binding of primary antibodies. Excessive heating increases hydrophobic binding and can lead to the precipitation of membrane proteins

(Sagne et al., 1996). As a result, membrane protein samples in future experiments should only be heated to 65°C for 5 minutes. Next, it is possible that post-translational modifications of the proteins such as glycosylation, lipidation, and/or phosphorylation could have added significant mass to K_V8.2a and K_V8.2b. The potential positive band shift associated with post-translational modifications may have positively shifted the locations of K_V8.2a and K_V8.2b bands on the western blots. Determination of the number of possible sites of modification on *kcnv2a* and *kcnv2b* will be required to assess the maximal degree of band shifting possible. There are many aspects of the western blotting protocol that can be manipulated in the search for K_V8.2a and K_V8.2b in zebrafish. Currently, our lab is also working towards the identification of K_V8.2a and K_V8.2b through immunofluorescence on cryosectioned tissue using the same custom monospecific antibodies. Notably, another laboratory designed custom antibodies against mouse and human K_V8.2 that worked successfully for immunofluorescence, but not for western blotting (Gayet-Primo et al., 2018). Data gathered through immunofluorescence experiments would not only determine the validity of our mutant lines, but also uncover the expression patterns of both paralogs within the zebrafish retina.

4.3 *kcnv2* Mutant Zebrafish Retinal Architecture

4.3.1 Introduction

Optical coherence tomography (OCT) has been the only approach used so far to assess the integrity of the retinal layers in individuals with *KCNV2* retinopathy. For these reasons, we performed both OCT and histology on our *kcnv2a*$^{-/-}$; *kcnv2b*$^{-/-}$ double mutant zebrafish to compare and contrast the insights gained through the two approaches.

4.3.2 OCT Imaging Reveals Retinal Aberrations in kcnv2 *Mutants*

As optical coherence tomography (OCT) is the primary clinical approach for retinal architecture assessment in patients with *KCNV2* retinopathy, it was important to visualize *kcnv2a*$^{-/-}$; *kcnv2b*$^{-/-}$ double mutant zebrafish (hereinafter *kcnv2* mutants unless otherwise stated) with the same technology. OCT is a non-destructive and non-invasive test used to generate 3D images of the retina (Tsang & Sharma, 2018). Like an ultrasound, OCT measures the interference patterns of emitted signals as they reflect off tissue structures. OCT imaging emits long-wavelength, low-coherence light through the pupil onto the retina. Differences in cellular refractive indices relative to a reference light beam reflected off of a mirror produce interference patterns that can be processed into 2D topographic images (a-scans). Several a-scans at different depths can then be combined into a b-scan, revealing a cross-sectional image of the retina (Tsang & Sharma, 2018). Although OCT imagery is a valuable diagnostic tool in the clinical setting, it produces low-resolution images that make identifying subtle physical abnormalities challenging.

OCT examination of 5 mpf zebrafish revealed that *kcnv2* mutants possessed all of the expected retinal layers without any significant disruption; however, an unusual interference signal between the ellipsoid and RPE layers was detected in 5 of the 6 mutants tested (Figure 4.6 a). In wildtype retinae, the ellipsoid layer is characterized by several horizontal rows of reflective punctae that represent the mitochondria-rich regions of photoreceptor inner segments. Similarly, the dense pigment granules within the RPE manifest through OCT imagery as a highly reflective band. Normally, the ellipsoid and RPE layers closely associate with one another, as is shown in the wildtype b-scan in Figure 4.6 a. The additional layer present between the ellipsoid and RPE layers in the *kcnv2* mutants, signified with an asterisk in the mutant b-scan, is an unfamiliar feature of the zebrafish OCT. The cellular changes responsible for this signal are not clear through OCT, but they fall within the region where most photoreceptor outer segments are located. Aside from this additional layer, there were no significant changes to the thickness of the entire retina or any retinal layer in *kcnv2* mutant zebrafish (Figure 4.6 b-e). Distal a-scans that generate a top-down view of the 5 mpf wildtype zebrafish retina demonstrated a highly organized photoreceptor mosaic as has been previously documented (Figure 4.6 f; Allison et al., 2010; Fadool, 2003). Similarly, 5 mpf *kcnv2* mutant retinae displayed a regular spatial arrangement of photoreceptors without any obvious disturbances (Figure 4.6 f).

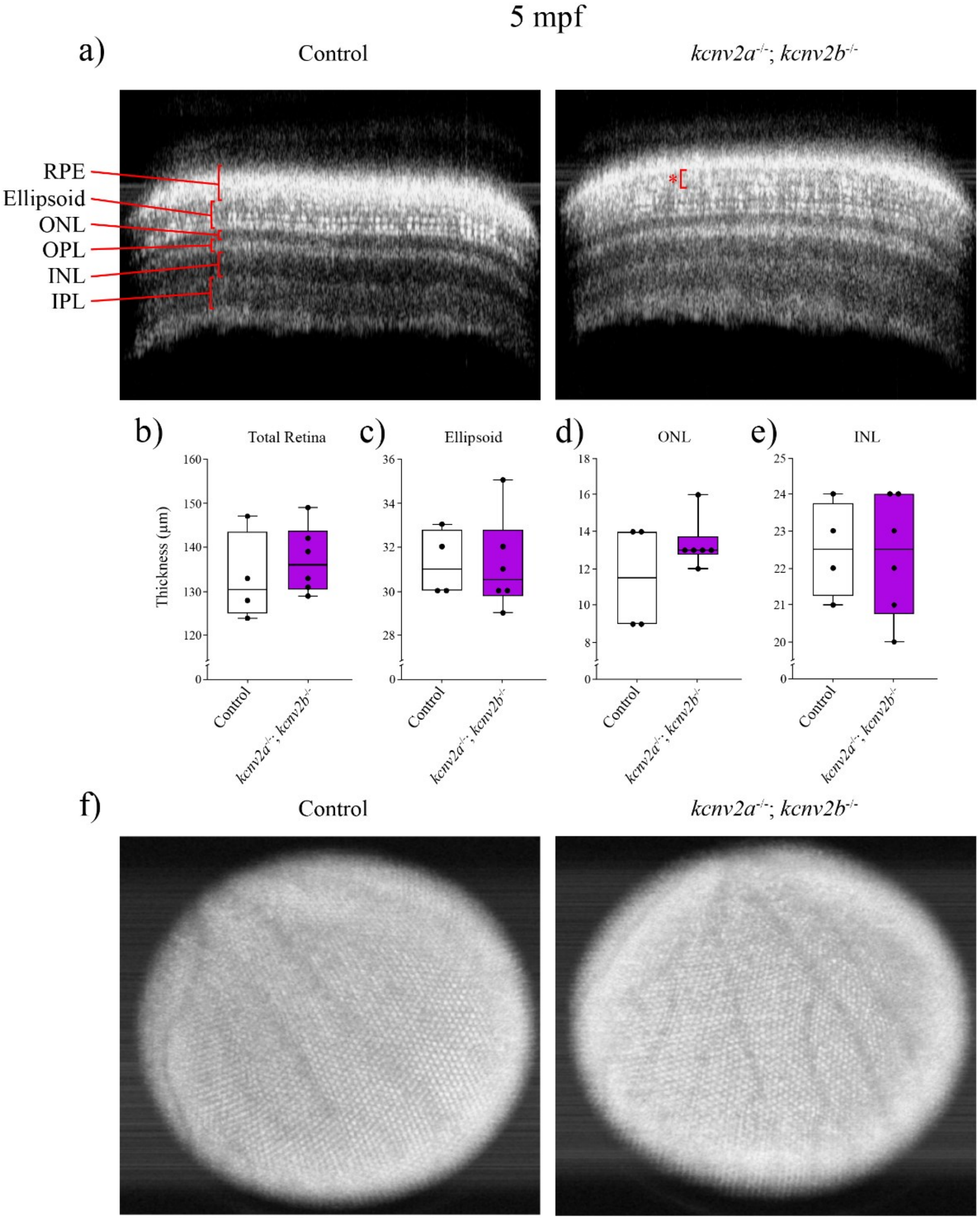

Figure 4.6 – *kcnv2* mutant fish have an abnormal interference signal. a) OCT imagery of 5 mpf *kcnv2* mutant zebrafish reveals an unusual signal (asterisk) between the ellipsoid and RPE layers. b-e) Measurement of total retina and individual retinal layer thickness. *kcnv2* mutant zebrafish retinae thicknesses were not significantly different from age-matched control fish. f) *En face* projections of the retina highlight the highly organized photoreceptor mosaic. Boxes

extend from the 25-75% percentiles, internal lines represent the median, and whiskers complete the range. RPE, retinal pigmented epithelium; ONL, outer nuclear layer; OPL, outer plexiform layer; INL, inner nuclear layer; IPL; inner plexiform layer.

The retinal architecture of 12 mpf *kcnv2b* homozygous mutants was also investigated using OCT technology. The presence of the unusual OCT signal seen in 5 mpf mutant fish was not detectable in 12 mpf mutants (Figure 4.7 a). Instead, large holes were observed in the ellipsoid layer of a small number of mutants (2/14), indicating loss of photoreceptor inner segments (Figure 4.7 a, b). Although the low incidence of retinal holes in mutants make the link between *kcnv2b* mutations and retinal holes weak, it represents an interesting observation that may be connected to the progressive degeneration of photoreceptors. Additionally, the ellipsoid layer was significantly thinner in *kcnv2b* mutant zebrafish relative to age-matched control fish (Figure 4.7 e), representing outer retinal degeneration. Notably, the most proximal ellipsoid punctae, representative of rod photoreceptors, was less reflective in *kcnv2b* mutants compared to control fish (Figure 4.7 a), reflecting a potential rod-photoreceptor dystrophy.

12 mpf *kcnv2b* zebrafish retinae also possessed hyperreflective punctae in the outer nuclear layer, best imaged as an a-scan (Figure 4.7 c, d). There were significantly more hyperreflective spots in the *kcnv2b* mutant outer retina compared to age-matched control fish (Figure 4.7 f). Importantly, hyperreflective punctae were detected in the inner retinae of control fish, indicating that spots observed in the outer retinae of *kcnv2b* mutants may have migrated from the inner retina. The cellular identity of the hyperreflective spots is currently unknown; however, similar punctae have been reported previously in the outer nuclear layer of retinae that are undergoing immune responses following subretinal injections (Dimopoulos et al., 2018). We therefore hypothesize that the hyperreflective spots in the outer nuclear layer of 12 mpf *kcnv2b*

mutants are resident retinal immune cells, microglia, that are removing cellular debris from dead and dying photoreceptors. Together, these data from 12 mpf *kcnv2b* mutant zebrafish demonstrate a progressive retinal degeneration manifested by photoreceptor layer thinning, retinal holes, and hyperreflective punctae migration to the outer nuclear layer

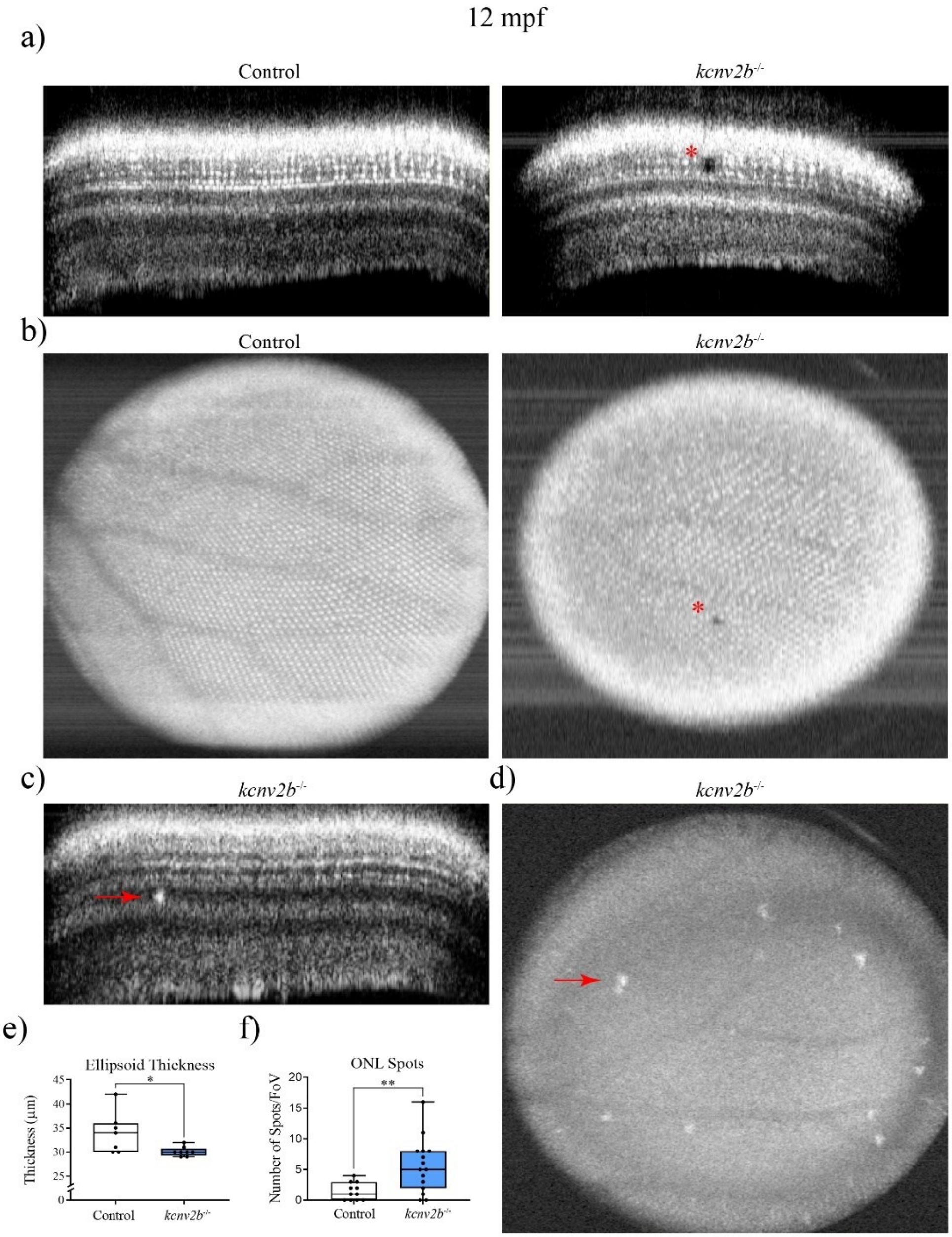

Figure 4.7 – 12 mpf *kcnv2b* mutants exhibit retinal holes and infiltrating hyperreflective punctae. a) Cross sectional and b) *en face* OCT images of 12 mpf control and *kcnv2b* mutant zebrafish retinae. A black spot (red asterisk) can be observed in the same mutant retina from both perspectives. c) Cross sectional and d) *en face* OCT images highlighting hyperreflective spots (red arrows) within the outer nuclear layer of 12 mpf *kcnv2b* mutants. Quantification of e) ellipsoid layer thickness and f) the number of hyperreflective spots observed in the subjects. $*p<0.05$; $**p<0.01$. Boxes extend from the 25-75% percentiles, internal lines represent the median, and whiskers complete the range.

For consistency between OCT experiments and other experiments discussed later in this thesis, the retinae of 1 mpf zebrafish were also examined. Unfortunately, the small eyes on 1 mpf fish produced OCT scans of a resolution that were too low to make accurate measurements of retinal layer thickness (Figure 4.8). We also assessed the retinae of 2 mpf fish with the hopes of generating higher quality OCT scans. While 2 mpf wildtype zebrafish produced higher resolution cross sections of the retina than 1 mpf fish, the image quality was still too poor make accurate assessments of retinal structure (Figure 4.8). In congruence with previous studies (Allison et al., 2010), the photoreceptor mosaic obtained from 2 mpf zebrafish demonstrated a clear transition into a row organization that was not seen in 1 mpf zebrafish (Figure 4.8).

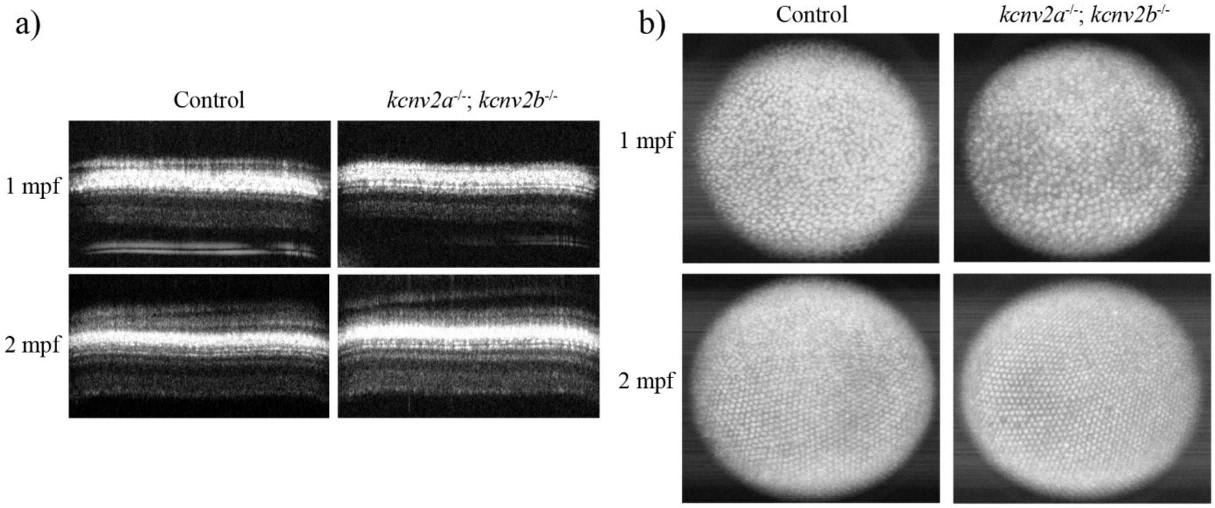

Figure 4.8 – OCT imagery from 1 and 2 mpf *kcnv2* mutant zebrafish. a) OCT b-scans are low resolution and cannot be used to accurately measure retinal layer thicknesses. b) *En face* projections of the photoreceptor mosaics of 1 and 2 mpf *kcnv2* mutant and wildtype zebrafish. A distinct row-based arrangement or photoreceptors is absent in 1 mpf zebrafish but evident at 2 mpf.

4.3.3 kcnv2 *Mutant Retinae have Irregular Pigment Distribution Patterns and Dysmorphic Outer Segments*

Histology was performed on 1 and 5 mpf *kcnv2* mutant zebrafish to obtain a clearer understanding of the retinal architecture in *kcnv2a* and *kcnv2b* mutant zebrafish. Hematoxylin and eosin stains were used to visualize the cellular organization of the retina. Hematoxylin specifically stains nuclei and rough endoplasmic reticulum of cells blue, allowing for the localization and quantification of individual cells (Chan, 2014). Conversely, eosin produces a pink stain on structures such as the cell membrane and mitochondria, informing the general cell shape and organelle distribution (Chan, 2014). Together, hematoxylin and eosin (H&E) staining can reveal a great amount of morphological detail and provide insights into the physiology of the tissue sample being studied.

An alteration in RPE pigment dispersion was evident in sections of 1 mpf *kcnv2* mutants relative to wildtype control zebrafish (Figure 4.9 a). Importantly, although *kcnv2* mutants and control fish were age-matched to 1 mpf, mutant zebrafish were larger than control fish (Figure 4.10 a). This most likely resulted from a discrepancy in fish tank population, whereby wildtype tanks were more crowded. As a result, it is possible that changes between the mutant and wildtype retinae may reflect the overall size difference between the two groups of fish. Regardless, in 60% of the 1 mpf mutants imaged (n=10), the pigment granules were loosely organized unlike the dense band of RPE pigment in control fish (n=10). The remaining four *kcnv2* mutant zebrafish demonstrated a wildtype RPE pigment distribution pattern. H&E staining confirmed that *kcnv2* mutants at 1 mpf possessed all of the expected retinal layers (Figure 4.10 a). In addition, the outer segment layer was significantly thicker in *kcnv2* mutant zebrafish relative to age-matched controls (Figure 4.9 b), perhaps reflecting expansion of the distal photoreceptor outer segments. The inner plexiform layer was also significantly thicker in *kcnv2* mutants, likely contributing with the outer segment expansion to an increase in total retinal thickness relative to wildtype control fish (Figure 4.10 b, e). All other retinal layers were similar between *kcnv2* mutants and control fish (Figure 4.10 c, d). It is difficult to determine if the differences between retinal layer thickness in 1 mpf zebrafish are a result of an overall size difference or due to mutations in both *kcnv2* paralogs. For this reason, conclusions about the mechanism underlying the changes to retinal architecture in 1 mpf *kcnv2* mutants must not be overstated.

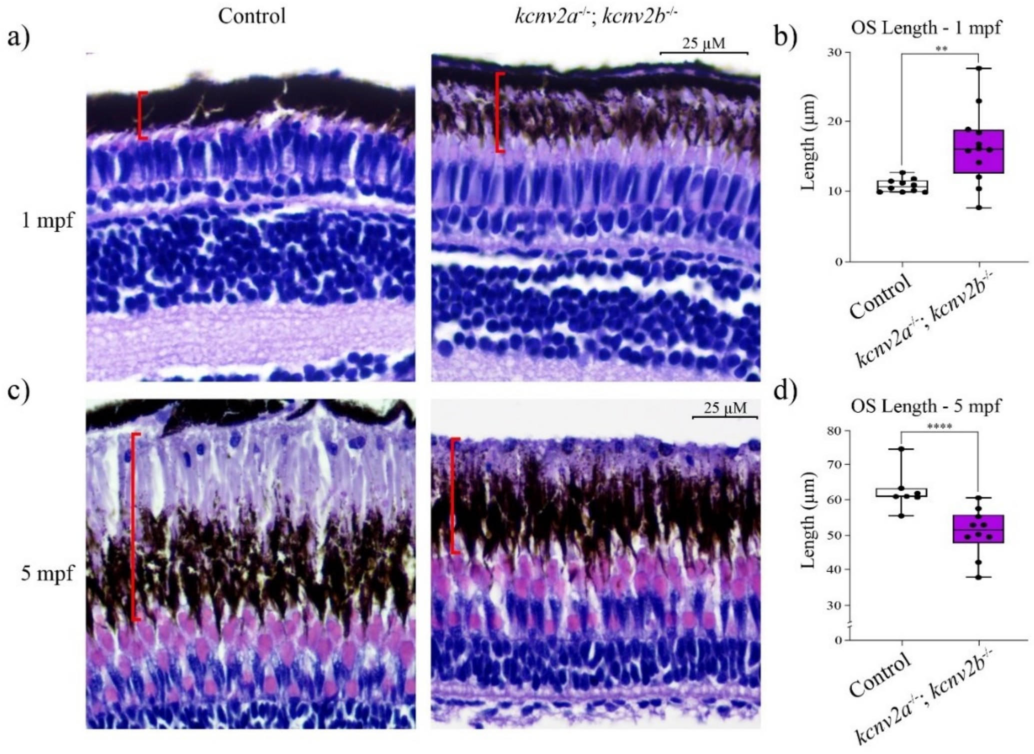

Figure 4.9 – Histological examination of *kcnv2* mutant retinae highlight morphological and pigment dispersion changes. a) H&E staining of 1 mpf wildtype and *kcnv2* mutant zebrafish retinal cross sections. RPE pigment granule distribution is more diffuse and irregular than age-matched control fish. b) Quantification of outer segment length in 1 mpf zebrafish. *kcnv2* mutant fish have longer outer segments than age-matched control fish. c) Retinal cross sections from 5 mpf *kcnv2* mutant zebrafish. Outer segment layer thickness (designated by the red bars) was significantly thinner in mutant retinae relative to control fish. d) Quantification of outer segment layer thickness (n=7 wildtype; n=9 mutant) $^{**}p<0.01$; $^{****}p<0.0001$. Boxes extend from the 25-75% percentiles, internal lines represent the median, and whiskers complete the range.

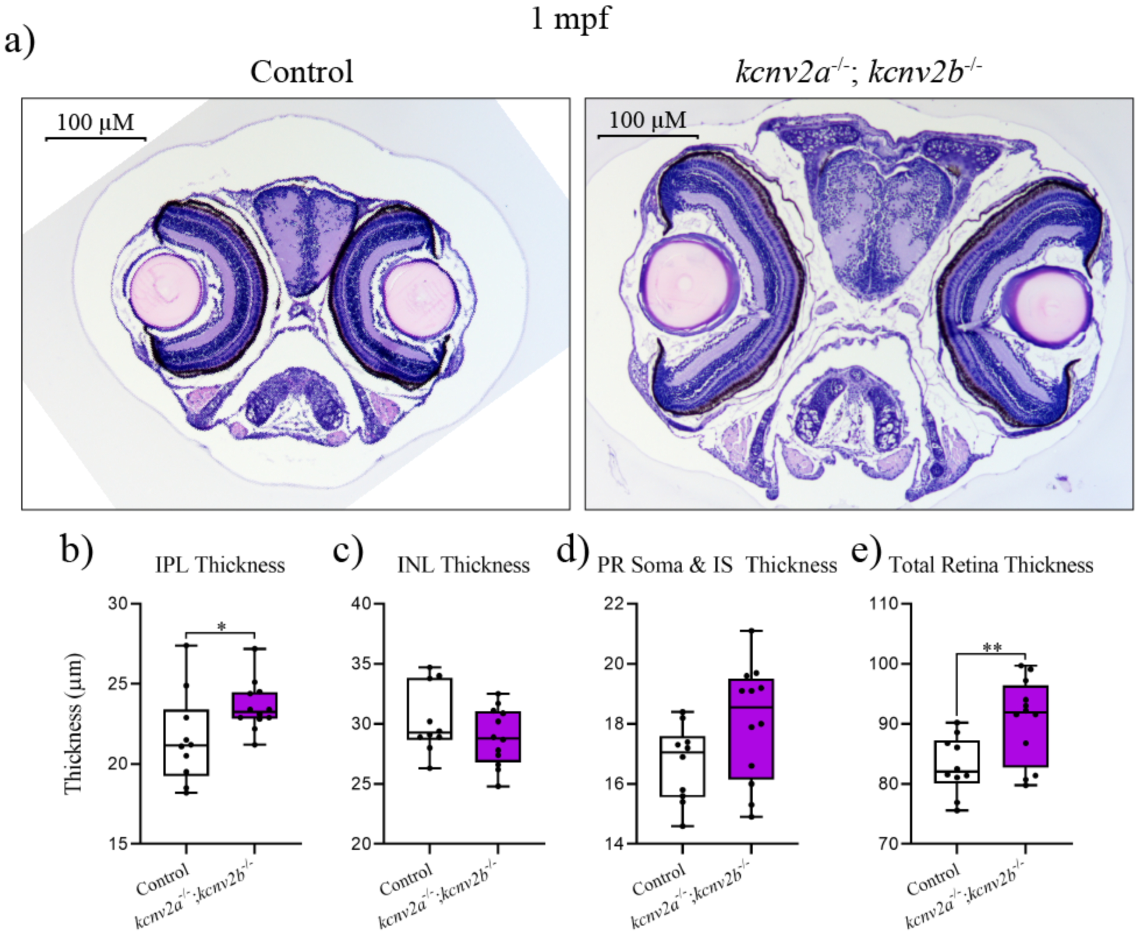

Figure 4.10 – 1 mpf *kcnv2* double mutants are larger than age-matched control fish. a) 20X images comparing the overall size difference of *kcnv2* double mutant zebrafish to age-matched controls. *kcnv2* double mutants are considerably larger, which may be influence the relatively larger photoreceptor outer segments compared to control fish. Aside from the b) inner plexiform layer (IPL), all other retinal layers were statistically similar between the fish (c-d). e) The total retinal thickness was statistically different, most likely due to a thicker IPL and outer segment layer in the mutant zebrafish. $*p<0.05$; $**p<0.01$. INL, inner nuclear layer; IS, inner segment; IPL, inner plexiform layer; PR, photoreceptor. Boxes extend from the 25-75% percentiles, internal lines represent the median, and whiskers complete the range.

RPE pigment dispersion was no longer disrupted in 5 mpf *kcnv2* mutant zebrafish relative to control fish; however, the photoreceptor outer segment layer in mutants was severely dysmorphic (Figure 4.9 c). In contrast to 1 mpf *kcnv2* mutants, the 5 mpf mutant outer segment layer was statistically thinner than that of age-matched controls (n=7) and appeared homogenous without definition between individual cells in 7 of the 10 mutants imaged (Figure 4.9 d). In comparison, wildtype outer segments were long, thin structures that were clearly defined from one another. It should be noted that H&E staining does not allow for the accurate identification of photoreceptor subtypes. Therefore, the outer segments within the outer segment layer quantified here represent many different photoreceptor subtypes. In fact, the outer segments of the most proximal photoreceptors, the UV cones, are not included in this layer. Regardless, there is a clear change to the length and organization of the distal components of photoreceptors in *kcnv2* mutant zebrafish at 5 mpf. The potential photoreceptor outer segment overgrowth followed by dystrophy is a surprising observation. As a result, confirmation of this phenotype through more precise photoreceptor measurements using photoreceptor subtype-specific transgenic lines or immunofluorescent approaches is necessary.

4.4 *kcnv2* Mutant Zebrafish Retinal Function

4.4.1 Scotopic B-Waves are Depressed in Juvenile kcnv2 *Mutant Zebrafish*

To assess visual function, *kcnv2* mutant zebrafish were subject to ERG analysis. Scotopic measurements were obtained through an intensity series ranging from dim (0.2 cd·s/m^2) to intermediate (1.0 and 3.0 cd·s/m^2) to bright (10 cd·s/m^2) stimuli. The intensity range probes all photoreceptor types differently: the dimmest flash intensity selectively stimulates rods while all brighter intensities evoke a mixed rod-cone response.

In 1 mpf mutant fish, the scotopic b-wave amplitude was significantly reduced relative to age-matched controls. This was the case for 1 mpf *kcnv2a* and *kcnv2b* single mutants as well as for *kcnv2a; kcnv2b* double mutants (Figure 4.11 a, d). Surprisingly, although the scotopic b-wave reduction was statistically significant in all 1 mpf mutants, the decrease tended to be more robust in single mutants than in double mutants. These data indicate that mutations in a single homolog of the human *KCNV2* gene are sufficient to diminish the mass retinal response to scotopic stimuli. Interestingly, measurements of the scotopic b-wave amplitude in 5 mpf *kcnv2a; kcnv2b* double mutants did not vary considerably from age-matched control fish (Figure 4.11 g). However, the b-wave amplitude from 5 mpf *kcnv2* mutants was highly variable, not unlike what is observed in the human disease *KCNV2* retinopathy (Abdelkader et al., 2020; Robson et al., 2010; Zobor et al., 2012), and there were a selection of mutants that consistently produced lower amplitudes compared to their cohort. A more detailed analysis of the low-amplitude mutants will be covered in Section 4.5.

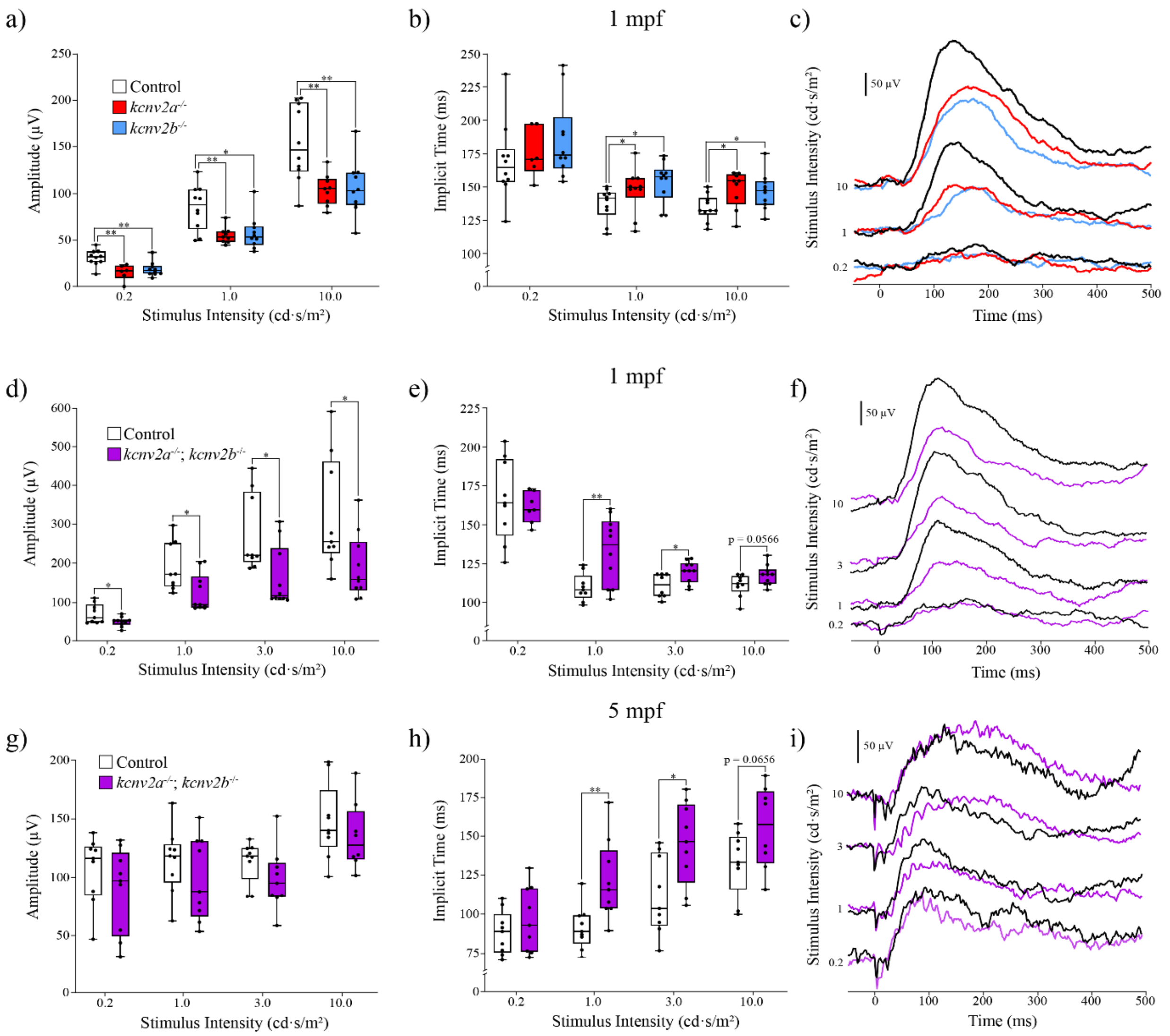

Figure 4.11 – Scotopic ERG responses from *kcnv2* mutant zebrafish are diminished and slow. Quantification of the b-wave amplitude, implicit time, and representative waveforms across the scotopic stimulus intensity series for a-c) *kcnv2a* and *kcnv2b* single homozygous mutant zebrafish (n=10 wildtype; n=9 *kcnv2a*$^{-/-}$; n=9 *kcnv2b*$^{-/-}$), d-f) 1 mpf *kcnv2* double mutant zebrafish (n=9 wildtype; n=10 *kcnv2* mutant), and g-i) 5 mpf *kcnv2* double mutant zebrafish (n=9 wildtype; n=8 *kcnv2* mutant). *p<0.05; **p<0.01. Boxes extend from the 25-75% percentiles, internal lines represent the median, and whiskers complete the range.

4.4.2 Scotopic B-Wave Time-to-Peak was Delayed in kcnv2 *Mutant Zebrafish*

A consistent finding in the ERG waveforms of human *KCNV2* retinopathy is a delayed b-wave (Fujinami et al., 2013; Gouras et al., 1983; Hood et al., 1996; Michaelides et al., 2005; Robson et al., 2010; Sergouniotis et al., 2012; Vincent et al., 2013; Wissinger et al., 2008; Zobor et al., 2012). ERG assessment of *kcnv2* mutants revealed that the b-wave implicit time was delayed at most, but not all, stimulus intensities (Figure 4.11 b, e, h.). Under scotopic conditions, intermediate stimuli reliably evoked b-waves that were significantly delayed relative to age-matched control fish. This feature was present in 1 mpf *kcnv2a* and *kcnv2b* single mutants and double mutants, as well as in 5 mpf double mutants. Unlike the juvenile scotopic b-wave amplitude reduction, the delayed intermediate b-wave persisted even as mutant fish matured in adulthood. As stimulus brightness was increased to the high-end of the intensity ramp, only *kcnv2a* and *kcnv2b* single mutant zebrafish produced significantly delayed b-waves. While 1 and 5 mpf double mutant b-waves did not meet the statistical significance threshold, the data distribution trended towards a delay (Figure 4.11 b, e, h). Importantly, neither single nor double *kcnv2* mutant zebrafish produced a significantly delayed b-wave in response to the dimmest stimuli, in contrast to it being a common finding in clinical assessments of human patients. Overall, results obtained through the scotopic ERG assessment of *kcnv2* mutants point to a persistent photoresponse timing defect whereby the mutant signal transmission speed is reduced.

4.4.3 Photopic Waveforms are Robust, but Delayed in kcnv2 Mutant Zebrafish

A reduced and delayed photopic b-wave, reflective of a dystrophic cone system, is among the most common ERG features of *KCNV2* retinopathy (Fujinami et al., 2013; Gouras et al., 1983; Hood et al., 1996; Michaelides et al., 2005; Robson et al., 2010; Sergouniotis et al., 2012; Vincent et al., 2013; Wissinger et al., 2008; Zobor et al., 2012). Light-adapted ERGs of 1 and 5 mpf *kcnv2* double mutant zebrafish revealed a strong but slow waveform (Figure 4.12 d-i). B-wave amplitudes under light-adapted conditions were similar to age-matched controls at both 1 and 5 mpf; however, a significant delay relative to the control b-wave was evident at both developmental timepoints. Notably, 1 mpf *kcnv2a* and *kcnv2b* single mutants generated photopic ERGs indistinguishable from age-matched controls (Figure 4.12 a-c), demonstrating that disruption of both zebrafish homologs is necessary to delay the photopic response.

As a final note, the a-wave observed in ERG waveforms was highly variable and often absent, even within control cohorts. As a result of the excessive variability, we have not presented here a statistical analysis of the a-waves. Notably, an identified feature of zebrafish ERG analysis is the ability of the b-wave to overwhelm the a-wave signal (Saszik & Bilotta, 1999; Seeliger et al., 2002; Xie et al., 2019).

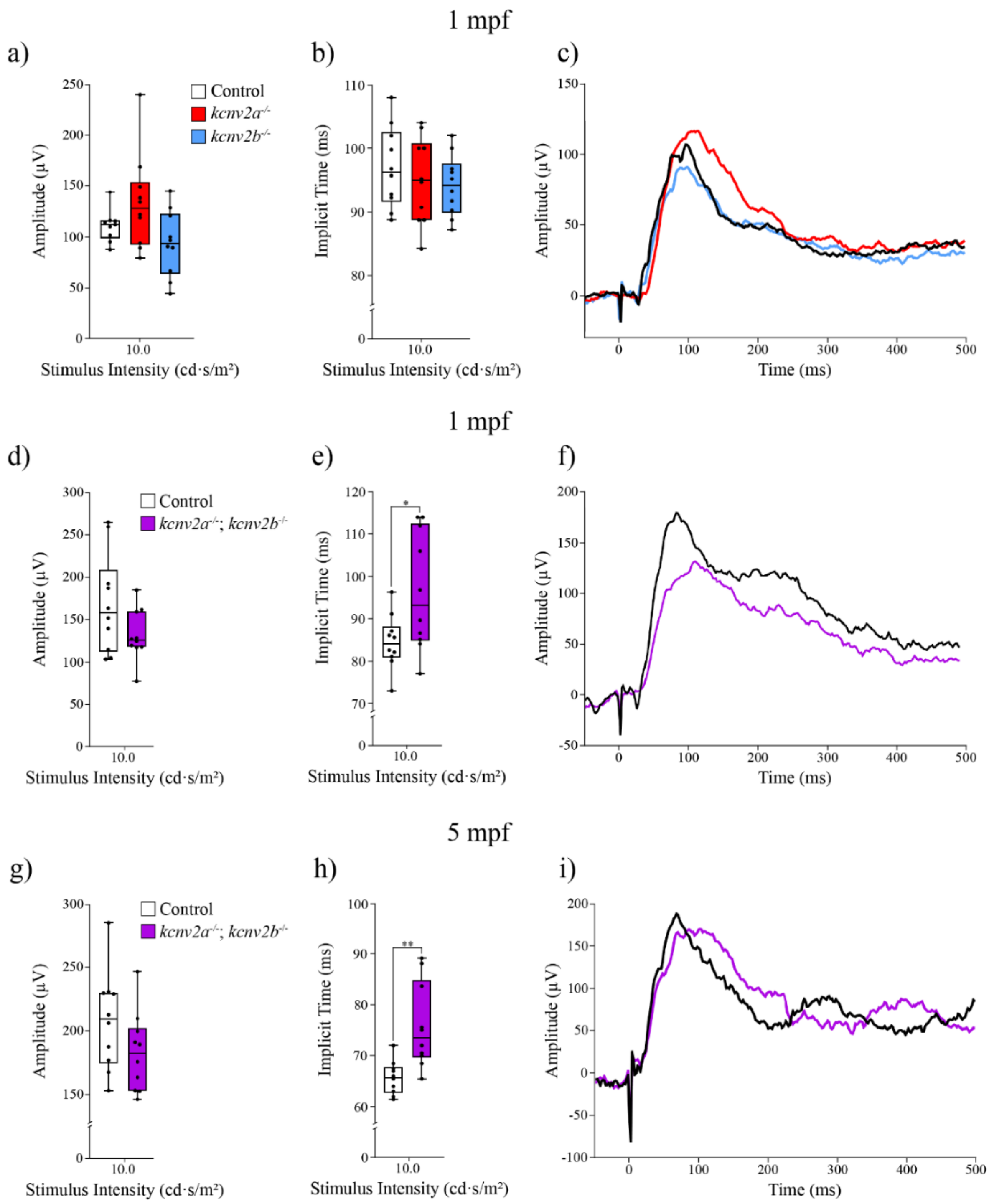

Figure 4.12 – Photopic ERG waveforms in *kcnv2* double mutants have increased b-wave implicit times. Quantification of the photopic b-wave amplitude, implicit time, and

representative waveforms from a-c) 1 mpf *kcnv2a* and *kcnv2b* single mutant zebrafish (n=9 wildtype; n=10 *kcnv2a*$^{-/-}$; n=10 *kcnv2b*$^{-/-}$), d-f) 5 mpf *kcnv2* double mutant zebrafish (n=10 wildtype; n=9 *kcnv2* mutant), and g-i) 5 mpf *kcnv2* double mutant zebrafish (n=10 wildtype; n=10 *kcnv2* mutant). Photopic stimulus intensity was 10 cd·s/m^2 in all panels. *p<0.05; **p<0.01. Boxes extend from the 25-75% percentiles, internal lines represent the median, and whiskers complete the range.

4.5 Correlations Between Morphology and Function in *kcnv2* Mutants

5 mpf *kcnv2* mutant zebrafish were used to investigate a potential connection between retinal architecture and functional output. To do this, mutant zebrafish were designated an identifying number and tracked as they progressed through a series of analyses: ERG, OCT, and histology. In total, a group of 5 *kcnv2* mutant zebrafish were subjected to the entire testing array. Although the previous sections illustrated variation in phenotypic features of 5 mpf *kcnv2* mutant zebrafish, two mutants exhibited irregular features in all three tests: Mutant 3 and Mutant 5 (Figure 4.13).

ERG waveforms from Mutant 3 and Mutant 5 show a reduction in scotopic dim stimuli amplitudes relative to age-matched wildtype controls (Figure 4.13 a). The development of a broad and late scotopic b-wave was also evident in both mutants as stimulus intensity increased to intermediate and high levels. A rapid increase in b-wave amplitude from sub-normal to wildtype levels across the stimulus intensity series was demonstrated by both mutants, a common finding in human *KCNV2* retinopathy patients (Abdelkader et al., 2020; Robson et al., 2010; Zobor et al., 2012).

Histological examination of the retinae of Mutant 3 and Mutant 5 reveal a dystrophic outer segment layer (Figure 4.13 b). Outer segments in the two mutants were difficult to resolve from one another, unlike the thin and long outer segments in the wildtype controls (Figure 4.9). An average of three measurements per mutant retinae revealed outer segment layer thicknesses of 49.7 µm and 53.1 µm for Mutant 3 and Mutant 5, respectively, both thin relative to the average thickness of 63.0 µm in age-matched wildtype control fish (Figure 4.9 c). Finally, the presence of the additional abnormal OCT signal between the ellipsoid and RPE layers was also identified in OCT images of Mutant 3 and Mutant 5.

Taken together, there is an apparent correlation between the morphology of the outer segments in *kcnv2* mutants and their performance in tests of visual function. It is important to mention that although this finding fits well with the phenotype of *KCNV2* retinopathy, it was made within a very small subject sample size. As such, confidence in the correlation between form and function in *kcnv2* mutant zebrafish must be tempered. Regardless, these data warrant further investigation into the interplay between outer segment morphology and functional output.

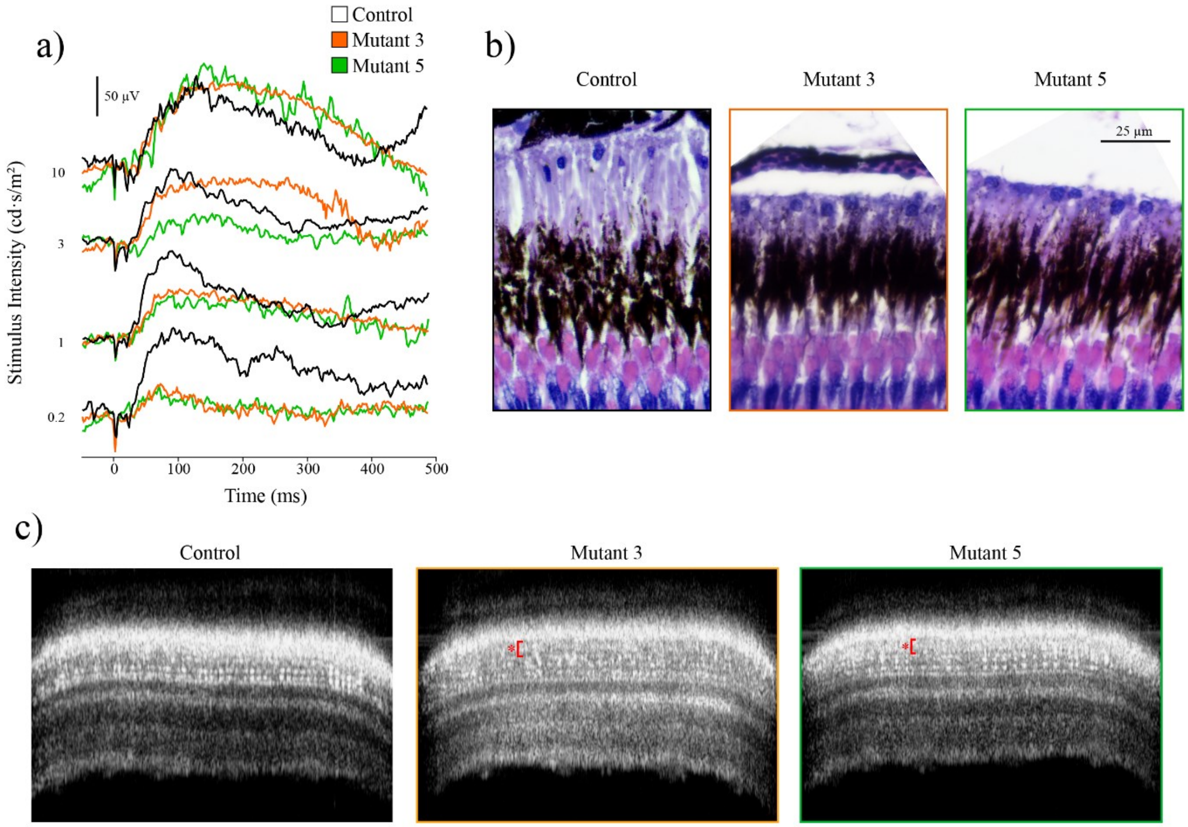

Figure 4.13 – Two 5 mpf *kcnv2* double mutant zebrafish have disturbed retinal architecture, an abnormal OCT signal, and reduced and late scotopic ERG output. a) Representative scotopic ERG waveforms from Mutant 3 and Mutant 5 compared to an age-matched wildtype fish. Both mutants featured reduced dim intensity b-waves that rapidly reached wildtype levels through intermediate and high intensity stimuli. b) Histological examination of the retinal structure of Mutant 3 and Mutant 5 reveal shortened and dysmorphic photoreceptor outer segment layers relative to an age-matched control cohort. c) OCT imagery of Mutant 3 and Mutant 5 demonstrates the presence of an abnormal signal between the ellipsoid and RPE layers.

CHAPTER 5: DISCUSSION AND FUTURE DIRECTIONS

5.1 Introduction

The goal of this work was to develop a zebrafish model of the human ocular disease *KCNV2* retinopathy to gain a better sense of the disease process and structural changes that follow the absence of the $K_V8.2$ subunit. *KCNV2* retinopathy is a rare inherited retinal disorder characterized by abnormal ERG recordings and mutations in the gene *KCNV2*. Patients diagnosed with *KCNV2* retinopathy often experience many symptoms of degenerated visual function, including reduced visual acuity, night vision, and colour vision along with photophobia, myopia, and a central blind spot. $K_V8.2$, the protein product of *KCNV2,* is involved in maintaining the resting membrane potential of photoreceptors and shaping the photoresponse to light. The underlying disease mechanism of *KCNV2* retinopathy is currently unknown, although the involvement of $K_V8.2$ suggests that misregulation of cellular voltage may be a factor. Fundoscopy and optical coherence tomography (OCT) on humans with *KCNV2* retinopathy has suggested that deterioration of visual function in the disease is correlated to retinal cell degeneration (Abdelkader et al., 2020; Kiray et al., 2020; Robson et al., 2010; Sergouniotis et al., 2012; Vincent et al., 2013; Wissinger et al., 2008; Zobor et al., 2012); however, limitations to *in vivo* assessments of the human retina leave many unanswered questions about the cell types involved and the progression of degeneration. We intended to use our zebrafish model of *KCNV2* retinopathy to characterize progressive changes to the morphological and functional features of the retina resulting from the loss of $K_V8.2$.

We used CRISPR-Cas9 mutagenesis to introduce frameshift mutations into *kcnv2a* and *kcnv2b*, the two zebrafish homologs of the human gene *KCNV2*. Mutations in *KCNV2* have been exclusively linked to *KCNV2* retinopathy (Wissinger et al., 2008), so we hypothesized that *kcnv2* double mutant zebrafish (*kcnv2a*$^{-/-}$; *kcnv2b*$^{-/-}$) would recapitulate many aspects of the phenotypes observed in affected humans. *kcnv2* mutant zebrafish were subjected to a battery of tests including the electroretinogram (ERG), OCT, and histology. In human patients with *KCNV2* retinopathy, the ERG and OCT are common assessments of visual function and structure, respectively. Therefore, we could use ERG and OCT results from humans with *KCNV2* retinopathy as a reference for shared disease features of our *kcnv2* mutant zebrafish. Histology, however, has never been performed on the retinal tissue of human *KCNV2* retinopathy patients, so this approach gave us an opportunity to investigate retinal changes in *kcnv2* mutant zebrafish at the cellular level. Through these functional and structural assessments, *kcnv2* mutant zebrafish were methodically characterized and compared to the human *KCNV2* retinopathy phenotype.

5.2 Retinal Dysfunction in *kcnv2* Mutants

Zebrafish have roughly equal rod and cone photoreceptor representation across their retinae (Richardson et al., 2017); therefore we expected *kcnv2* mutant zebrafish to exhibit impaired scotopic and photopic ERG waveforms resembling those produced by humans with *KCNV2* retinopathy. Specifically, in response to dim scotopic stimuli, we suspected that *kcnv2* mutant zebrafish would generate significantly delayed and subnormal or even absent ERG b-waves compared to wildtype control fish. In addition, we anticipated a rapid amplitude increase that achieved normal or supernormal levels in response to the rising intensity series. In response to photopic stimuli, we predicted that *kcnv2* mutant zebrafish would generate substantially delayed and reduced or altogether eliminated waveforms relative to control fish.

As hypothesized, ERG assessment of *kcnv2* mutant zebrafish revealed functional impairment of both photopic and scotopic vision; however, factors such as age and genotype were found to influence the degree of similarity to the human *KCNV2* retinopathy phenotype. The scotopic b-wave amplitude was of particular interest for our study, as *KCNV2* retinopathy was initially characterized by a reduced scotopic b-wave amplitude in response to dim stimuli that rapidly increased to supernormal levels across an intensity series (Gouras et al., 1983). After subjecting 1 mpf *kcnv2* single mutants (*kcnv2a*$^{-/-}$ and *kcnv2b*$^{-/-}$) and double mutants (*kcnv2a*$^{-/-}$; *kcnv2b*$^{-/-}$) to a scotopic intensity series, we found that all three genotypes generated the expected subnormal b-wave in response to dim stimuli (0.2 cd·s/m^2; Figure 4.9 a, d). However, the reduced b-wave in both *kcnv2* single and double 1 mpf mutants persisted across the intensity series (Figure 4.9 a, d), suggesting that the mechanism responsible for the rapid increase in scotopic b-wave amplitude in *KCNV2* retinopathy may be absent in 1 mpf *kcnv2* mutant zebrafish.

Given the persistent b-wave amplitude reduction in 1 mpf *kcnv2* mutants, we refined our expectation for the scotopic ERG output from the older 5 mpf *kcnv2* double mutants such that the reduced b-wave would be maintained or even worsened in mature mutant fish. However, the average b-wave amplitude from the 5 mpf *kcnv2* mutants was comparable to age-matched control fish at all intensities (Figure 4.9 g). It is unclear how the significant b-wave amplitude deficiency observed in 1 mpf *kcnv2* mutants can be suddenly rectified, especially since *KCNV2* retinopathy has a progressive nature. Regardless, future ERG experiments will focus on the visual function of even older *kcnv2* mutants and will bring more clarity to these puzzling data. Overall, it is important to note that I did not observe scotopic supernormal b-wave responses at any stimulus intensity or developmental timepoint, consistent with findings from the mouse model of *KCNV2* retinopathy (Hart et al., 2019). While supernormal b-waves have certainly been identified in humans with *KCNV2* retinopathy, these data presented here add further support to the notion that the supernormal b-wave should not be considered a ubiquitous feature of the disease.

While there were substantial inconsistencies between the nature of the scotopic b-wave amplitude of *kcnv2* mutant zebrafish and humans with *KCNV2* retinopathy, an ERG feature that united the two was a significantly delayed b-wave under scotopic conditions (Figure 4.9 b, e, h). Surprisingly, the dimmest scotopic stimulus that generally evoked the most delayed b-wave in humans and $K_V8.2$ knockout mice (Hart et al., 2019) did not have a similar effect in *kcnv2* mutant zebrafish, and instead evoked responses that fell within normal limits (0.2 $cd{\cdot}s/m^2$; Figure 4.9 b, e, h). As the scotopic intensity series increased, however, a significant b-wave delay relative to age-matched control fish was observed in all *kcnv2* mutant cohorts tested. The brightest scotopic flash (10 $cd{\cdot}s/m^2$) produced a b-wave in *kcnv2* double mutants that was not statistically different from control fish, but trended towards a delay (Figure 4.9 e, h).

Notably, two 5 mpf *kcnv2* mutant fish, Mutant 3 and Mutant 5, demonstrated the initially anticipated scotopic b-wave amplitude reduction in response to the dim stimuli that rapidly increased with the intensity series, a consistent finding in human patients with *KCNV2* retinopathy (Figure 4.11 a; Abdelkader et al., 2020; Robson et al., 2010; Zobor et al., 2012). Moreover, at higher stimulus intensities, the scotopic b-wave was significantly delayed and broadened relative to age-matched control fish. Curiously, the abnormal high intensity ERG waveforms from Mutant 3 and Mutant 5 were similar to those generated by HCN channel knockout mice that lacked I_h in response to a 3 $cd{\cdot}s/m^2$ scotopic stimulus (Seeliger et al., 2011). As I_h and I_{kx} both regulate the temporal resolution of photoreceptor function (Barnes, 1994), the delayed b-waves may result from a shared pathology. Specifically, Seeliger et al. (2011) determined that the delayed b-wave was correlated to interference between the rod and cone photoresponses that share a common bipolar cell pathway. They found that uncoupling the I_h-deficient rod and cone systems through ablation of Cx36 gap junctions restored the b-wave implicit time to normal levels (Seeliger et al., 2011). Importantly, the authors used a 3 cd·s/m^2 stimulus to evoke the delayed b-wave in I_h-deficient mice, a *mesopic* intensity at which both the rod and cone systems contribute to the photoresponse. Conversely, the dimmest scotopic intensity in our functional experiments, 0.2 cd·s/m^2, evokes a rod-only response. For this reason, the absence of rod and cone signal integration following the dimmest scotopic stimuli in *kcnv2* mutants may account for the lack of a delay in the b-wave. It would be very interesting to perform our scotopic intensity series on *kcnv2* mutant zebrafish crossed to a Cx35.4-deficient line (homologous to human Cx36; Li et al., 2009). The uncoupling of the rod and cone systems within *kcnv2* zebrafish might rescue the delayed scotopic b-wave, as was shown in I_h-deficient mice (Seeliger et al., 2011). Admittedly, this mechanism is less likely to be the case for human *KCNV2* retinopathy, as affected individuals *do* have a delayed scotopic b-wave. Regardless, the similar waveforms between *kcnv2* mutant zebrafish and I_h-deficient mice is interesting and provides an avenue for future investigations. Our *kcnv2* mutant zebrafish can therefore serve as experimental models of delayed b-waves, a common diagnostic marker of ocular disease without a clear physiological basis.

Photopic ERG assessment of cone photoreceptors within *kcnv2* mutant zebrafish revealed a surprisingly intact cone response. Light-adapted b-wave amplitudes within *kcnv2* single and double mutants were equivalent to wildtype fish (Figure 4.10), which contrasts with the severely dysfunctional photopic response in human *KCNV2* retinopathy, often featuring distorted and diminished photopic b-waves (Robson et al., 2010; Vincent et al., 2013; Wissinger et al., 2008; Wu et al., 2006). Interestingly, the photopic b-wave was delayed in only the *kcnv2* double mutants, but not in the single mutants. While single mutants exhibited a robust increase in scotopic b-wave implicit times, these photopic data demonstrate that both paralogs may need to be disrupted to delay the cone-driven b-wave. Importantly, I_{kx} in macaque cones is roughly 5 times greater than in rods (Gayet-Primo et al., 2018), and therefore single *kcnv2* mutations (*kcnv2a*$^{-/-}$ or *kcnv2a*$^{-/-}$) may not sufficiently retard the cone response so as to cause significant signal interference. Again, we do not know the expression patterns of $\mathrm{K_V}$8.2a or $\mathrm{K_V}$8.2b in the zebrafish retina, so claims of subfunctionalization or cooperative association between the two paralogs must be tempered.

Despite prior light adaption, a small number of rod photoreceptors were stimulated by the single flash photopic ERG used in our experiments (McCulloch et al., 2015). Consequently, rod and cone signal interference may also contribute to the delayed photopic b-wave seen in *kcnv2* double mutants. It would be of interest to test the photopic 30 Hz flicker response of *kcnv2* double mutant zebrafish, as stimuli exposure at this frequency evokes a cone-only response that does not feature rod and cone signal integration. We anticipate that the delayed b-wave would be rectified in *kcnv2* double mutants exposed to a flicker series, as only the cone response is transmitted and therefore cannot produce interference with the absent rod signal. Regardless, the physiologic basis underlying the reduced time-to-peak in human *KCNV2* retinopathy may have similar origins within the zebrafish animal model, making it a promising focus for future research.

The non-invasive nature of the ERG makes it a very useful diagnostic measure of overall retinal function in the clinical setting; however, concessions are made in the interpretation of the waveform. Our characterization of visual function of *kcnv2* mutant zebrafish solely focused on the b-wave, a component of the ERG thought to represent ON bipolar cell depolarization.

Importantly, inner segment modulation of the photowaveform occurs after the peak of the a-wave (post-phototransduction cascade), making the b-wave a relevant measurement for our studies. However, the visual information transmitted to bipolar cells is complex and cryptic. For example, cone ON bipolar cells integrate visual information from both rods and cones through gap junctions that connect photoreceptors and also through amacrine cells that bridge rod and cone bipolar cells (Seeliger et al., 2011). Additionally, bipolar and photoreceptor cell activity is constitutively modulated by horizontal cells through the process of lateral inhibition (Chaya et al., 2017; Wen & Thoreson, 2019). The functional deficit observed in the *kcnv2* mutant b-wave may be secondary to dysfunction in other retinal cell populations such as Müller glia or the RPE. Although the ERG b-wave is an excellent indicator of general retinal function through bipolar cell activity, the extensive influence of other retinal processes on bipolar cell function disguises the culprit cell population.

One avenue we have not explored yet is the use of drug treatments to further dissect the ERG response. Pharmacological inhibitors such as 2-amino-phosphonobutyric acid (APB) and threo-β-benzyloxyaspartic acid (TBOA) can be used to help resolve the outer segment-driven a-wave by eliminating the large b-wave from the waveform (Demarco & Powers, 1989; Jardon et al., 1989; Nelson & Singla, 2009; Seeliger et al., 2002). Removal of the obstructive b-wave will enable a more detailed analysis of the role photoreceptors have in *kcnv2* mutant visual dysfunction. While the initial slope of the a-wave is driven by closure of the CNG channels in the outer segment, inner segment currents may limit its amplitude and duration through their modification of the photovoltage (Barrow & Wu, 2009b, 2009a; Beech & Barnes, 1989; Santina et al., 2012). Further, the magnitude and dynamics of the a-wave could be disrupted by changes to outer segment morphology or cell degeneration. Importantly, a delayed and broadened a-wave is a common feature in human *KCNV2* retinopathy (Fujinami et al., 2013; Robson et al., 2010; Vincent et al., 2013; Zobor et al., 2012), so the assessment of the *kcnv2* mutant a-wave is a vital step in validating the suitability of our zebrafish model of *KCNV2* retinopathy.

Previous electrophysiological recordings of isolated photoreceptors or photoreceptors in retinal slice tissue have provided key insights into the functions of I_{kx} (Beech & Barnes, 1989; Czirják et al., 2007; Gayet-Primo et al., 2018; Smith et al., 2012). However, it is unclear how the rod and cone electrophysiology would change when the photoreceptors develop without the Kv2/Kv8.2 channel, and how those alterations would correlate with an abnormal ERG response. In theory, loss of Kv8.2 could lead to a substantial depolarization of the resting membrane potential due to loss of the sustained K^+ efflux. As a result, a larger stimulus may be necessary to hyperpolarize the photoreceptor to the threshold required for cessation of synaptic release of glutamate. Consequently, the influence of the I_h current in photoreceptor recovery may be reduced, as the mutant photoreceptor's operating range would be shifted to depolarized potentials. Electrophysiological experiments on *kcnv2* mutant zebrafish could therefore better define the individual cellular changes that underlie the observed whole retina dysfunction.

Although the photoreceptors demonstrate significant degeneration, other retinal cells such as the metabolically supportive RPE or Müller glia may be the primary site of dysfunction. An interesting approach that would help resolve this quandary is through the interrogation of electrical properties of individual retinal cells. Specifically patch clamp electrophysiology on zebrafish retinal slices (as described in Section 1.3.2), would reveal valuable cell type-specific insights into how changes in cellular membrane potential are altered in the mutant state. Single cell recordings from retinal slices would be an effective approach to probe the photoresponse of all resident cell populations of the retina including cell subpopulations such as rods and cones.

Importantly, as I_{kx} is a critical regulator of the resting membrane potential of photoreceptors, the investigation into the resting membrane potential of *kcnv2* mutant photoreceptors is an exciting prospect. As mentioned above, we would expect that photoreceptors in *kcnv2* mutants would have a more depolarized resting membrane potential relative to control photoreceptors. A combination of electrophysiological approaches will likely be used in future experiments with the ultimate goal of identifying the cellular population underlying visual dysfunction observed in *kcnv2* mutant zebrafish. While we have not yet characterized the molecular or cellular basis of our functional findings, we have identified a fundamental link between the two zebrafish *kcnv2* paralogs and visual function.

5.3 Changes to retinal architecture in *kcnv2* mutants

In addition to functional deficits, we predicted that there would be associated changes to the retinal structure of *kcnv2* mutant zebrafish. The zebrafish retina has a rod:cone ratio similar to that of the human macula (Richardson et al., 2017), and since many of the OCT abnormalities identified in patients with *KCNV2* retinopathy are localized to the macula, we expected to observe similar aberrations in *kcnv2* mutant zebrafish. Specifically, we anticipated partial or complete loss of the ellipsoid layer and/or a degree of retinal thinning as both findings have been documented in the maculae of human patients (Abdelkader et al., 2020; Kiray et al., 2020; Sergouniotis et al., 2012; Vincent et al., 2013; Wissinger et al., 2008; Zobor et al., 2012). Importantly, the use of an animal model of *KCNV2* retinopathy created the opportunity to dissect and investigate the diseased retinal architecture at the cellular level through histology. The lack of careful examination of retinal cell morphology in affected humans and animal models is a significant gap in our current understanding of *KCNV2* retinopathy. We expected that histology of *kcnv2* mutants would reveal significant changes to retinal structure, particularly within the photoreceptors, that are too subtle to detect through OCT.

OCT analysis revealed that 5 mpf *kcnv2* double mutants had retinae that were largely similar to those of age-matched control fish. All retinal layers were intact, with no significant differences in the thickness of the total retina or any specific layer (Figure 4.6 a-e). We carefully inspected the ellipsoid layer (representative of the mitochondria-rich region of photoreceptor inner segments) of the mutant OCT scans, as it was frequently disrupted in human cases of *KCNV2* retinopathy, suggestive of photoreceptor death (Abdelkader et al., 2020; Kiray et al., 2020; Sergouniotis et al., 2012; Vincent et al., 2013; Wissinger et al., 2008; Zobor et al., 2012); however, the ellipsoid layer was intact and unchanged compared to wildtype control fish (Figure 4.6 a, c).

An alteration to the retinae of multiple 5 mpf *kcnv2* mutants was the presence of an unusual OCT signal between the ellipsoid layer and the RPE (marked with an asterisk in Figure 4.6 a) that was absent in all control fish imaged (n=3). Rare instances of 'optical gaps' and unilateral retinal detachment which also occur between the ellipsoid and RPE layers have been reported in individuals with *KCNV2* retinopathy (Michaelides et al., 2005; Vincent et al., 2013); however, unlike these human retinal abnormalities, the signal in *kcnv2* mutant zebrafish did not represent a void. Instead, the abnormal layer appeared to be continuous with ellipsoid layer but lacked the hyperreflective mitochondrial punctae of the ellipsoid region. As the total retinal thickness between *kcnv2* mutants and wildtype fish was not different, the novel OCT signal may result from native tissue normally obscured by the hyperreflective RPE layer.

Histological examination of the zebrafish retina highlighted significant changes to the photoreceptor outer segments of 5 mpf *kcnv2* double mutants. Although the measurement of photoreceptor outer segment layer thickness used in our analyses does not resolve different photoreceptor subtypes from one another, it can serve as an indication of general outer segment morphology. Interestingly, outer segments in 5 mpf mutants were significantly shorter than wildtype control fish (Figure 4.8 c, d), possibly reflecting photoreceptors in the process of degeneration. In addition, outer segments in 5 mpf *kcnv2* mutants were undefined and packed tightly together, unlike wildtype outer segments that had clear borders with substantial spaces separating them from one another. Given the location of this abnormality, we suspect that the novel signal observed in OCT images of the 5 mpf mutant retina is correlated to the dysmorphic outer segments identified here. In fact, all five mutants that presented with the unusual OCT signal also had dysmorphic photoreceptor outer segments, while the final remaining fish possessed an ordinary OCT scan and typical outer segments. Importantly, the same 5 mpf *kcnv2* mutants that possessed substantial dysfunctional similarity to human *KCNV2* retinopathy, Mutant 3 and Mutant 5, also exhibited OCT abnormalities and a severely dysmorphic photoreceptor outer segment layer (Figure 4.11 b, c). These mutants highlight a potential correlation between the visual function and retinal cell morphology in these mutants.

Curiously, histology of younger 1 mpf *kcnv2* double mutant zebrafish revealed a thicker photoreceptor outer segment layer relative to age-matched control fish (Figure 4.8 a, b). It is important to note that although the *kcnv2* mutants and control fish are age-matched, *kcnv2* mutants was considerably larger than control fish (Supplemental Figure 4.2 a). Aside from the photoreceptor outer segment layer and the inner plexiform layer, all retinal layers were statistically similar between *kcnv2* mutant and control fish (Supplementary Figure 4.2 b-e). Although changes to the photoreceptors may be a result of the overall size increase in *kcnv2* mutants, it is notable that the 1 mpf photoreceptor outer segments are expanded relative to control zebrafish. In addition, RPE pigment granules in *kcnv2* mutants were distributed more sparsely throughout the outer segments compared to the dense band of pigment observed in control fish (Figure 4.8 a, b). The nature of RPE pigment granule dispersion and outer segment length in 1 mpf *kcnv2* mutants are difficult to rectify, as 5 mpf *kcnv2* mutants no longer displayed abnormal pigment granule dispersion and outer segments are significantly shorter. However, it is plausible that photoreceptors undergo early outer segment expansion before eventually degenerating at 5 mpf.

Photoreceptors are dynamic cells that can actively modulate their cellular properties in response to light exposure. For example, zebrafish rod and cone inner segments elongate and contract in opposition following light and dark exposure through a mechanism known as retinomotor movement (Menger et al., 2005). In addition to inner segment elongation and contraction, the complementary movement of pigment granules in and out of the RPE microvilli in response to light are another critical component of the retinomotor movement. Disruptions to the light/dark cycle change retinomotor movements, highlighting an intimate connection between the photoreceptor morphology and light exposure (Menger et al., 2005). Additionally, the outer segment itself can change shape during development depending on the amount of light it is exposed to. Specifically, zebrafish photoreceptors that undergo early development in complete darkness generate expanded outer segments relative to those that develop in typical light/dark cycles (Crespo & Knust, 2018). As photoreceptors are the primary light detecting cells in the retina, it is likely that retinomotor movement and outer segment expansion are a direct result of photon detection in the outer segment. However, changes to photoreceptor morphology may be secondary to activity of other light detecting retinal cells such as intrinsically photosensitive retinal ganglion cells. Regardless, it is reasonable to view these examples as attempts to optimize the photoreceptors' ability to detect light by actively changing their morphology.

We speculate that the unusual changes to photoreceptor morphology in *kcnv2* mutant zebrafish may result from dysfunctional light-detecting capabilities. 1 mpf *kcnv2* mutants had an increased outer segment layer thickness, reflecting an increased growth rate relative to age-matched control fish. Similar to photoreceptor cells that develop in darkness (Crespo & Knust, 2018), dysfunctional rods and cones within 1 mpf *kcnv2* mutants may expand their outer segments in an attempt to capture light more effectively. At 5 mpf, the photoreceptor outer segment layer is significantly reduced relative to control fish, possibly reflecting dystrophic outer segments. It is conceivable that the photoreceptors actively undergo progressive degeneration following a chronic light detection deficit.

Interestingly, rod photoreceptors in *gdf6a* mutant zebrafish undergo early outer segment expansion in a similar manner to the 1 mpf *kcnv2* mutant fish documented here (Nadolski et al., 2020). Gdf6a is a morphogen expressed in the dorsal zebrafish optic cup that works to orchestrate retinal patterning during eye development. Investigation of the 5 dpf *gdf6a*$^{-/-}$ retinal transcriptome at the time of rod outer segment expansion revealed a significant and massive reduction in *kcnv2b* transcripts (~32-fold). *kcnv2a* transcripts, in contrast, showed an almost 2-fold upregulation, but the difference was not significant (Nadolski et al., 2020). Importantly, rod outer segment morphology eventually aligned with wildtype control outer segments as *gdf6a* mutant fish matured. The correlation between *kcnv2* transcript misregulation and abnormal photoreceptor outer segment morphogenesis in *gdf6a* mutant fish is exciting; however, the two phenotypes are far from identical. For example, rod outer segments in 14 dpf *gdf6a* mutant fish are not significantly different in size from control fish (Nadolski et al., 2020), whereas outer segments in *kcnv2* mutants are significantly larger at 1 mpf. Additionally, rod outer segments in *gdf6a* mutant do not progressively degenerate as may be happening in *kcnv2* mutants. Finally, cone photoreceptors in *gdf6a* mutants were also dysmorphic, whereby outer segments were consistently reduced in size compared to wildtype zebrafish (Nadolski et al., 2020). Histology performed on *kcnv2* mutants in this thesis is limited as it does not permit the identification of photoreceptor subtypes. Although there are several inconsistencies between the photoreceptor phenotypes of *gdf6a* and *kcnv2* mutants, it is possible that they share physiological processes that result in abnormal outer segment growth and maintenance.

Clinical features of *KCNV2* retinopathy are progressive, whereby functional output and retinal structure gradually deteriorates with time (Gouras et al., 1983; Michaelides et al., 2005; Robson et al., 2010; Sergouniotis et al., 2012; Vincent et al., 2013). While we have not yet fully characterized *kcnv2* double mutants at ages past 5 mpf, we did assess 12 mpf *kcnv2b*$^{-/-}$ single mutants through OCT imagery. The aged retina of 12 mpf *kcnv2b* single mutants displayed features suggestive of a later stage of retinal degeneration compared to 5 mpf *kcnv2* double mutants (Figure 4.7). Of particular interest was the appearance of large holes in the photoreceptor layer of several *kcnv2b* mutant fish (Figure 4.7 a, b). The retinal holes may represent spaces where degenerated photoreceptor cells once resided. Further support of retinal degeneration in 12 mpf *kcnv2b* mutant zebrafish was the significant thinning of the photoreceptor layer relative to age-matched control fish (Figure 4.7 e). Additionally, hyperreflective spots were observed in the outer retinae of all 12 mpf *kcnv2b* homozygous mutants (Figure 4.7 c, d, f). A comparable number of hyperreflective spots were identified in control fish; however, they were restricted to the inner retina. We suspect that these hyperreflective punctae represent microglia, the resident immune cells of the retina. Microglia have been shown to migrate from the inner retina to the outer retina where they coordinate and contribute to phagocytosis of non-apoptotic photoreceptors (Okunuki et al., 2018; Zhao et al., 2015). Similar hyperreflective spots have been documented in the retina of an individual experiencing a severe immune reaction following a subretinal injection (Dimopoulos et al., 2018), so it is possible that these signatures share a common cellular identity. The retinae of 12 mpf *kcnv2b* single mutant zebrafish exhibit structural markers and a cellular response indicative of degeneration; however, due to their different genotypes, retinae of *kcnv2b* single mutants are not directly comparable to those of *kcnv2* double mutants. For this reason, future OCT experiments will examine the retinae of 12 mpf *kcnv2* double mutants and contrast the structural appearance to 5 mpf *kcnv2* double mutants. The data gathered from 5 and 12 mpf *kcnv2* double mutant OCT will enable us to make a more informed conclusion about the progressive nature of *kcnv2* mutations in zebrafish.

Since the outset of this thesis work, we have been interested in the apparent discrepancy in the degree of degeneration between the cone-dominated central retinae and the rod-dominated peripheral retinae of humans with *KCNV2* retinopathy. Many reports have identified tissue disruptions localized to the central retina through OCT and fundoscopy (Abdelkader et al., 2020; Kiray et al., 2020; Sergouniotis et al., 2012; Vincent et al., 2013; Wissinger et al., 2008; Zobor et al., 2012); however, there have not been accounts of any structural changes to the peripheral retina of affected individuals. This is particularly puzzling due to the robust rod-driven scotopic shortcomings of patients with *KCNV2* retinopathy. While zebrafish do not possess comparable retinal regions to those present in human eyes, they do offer an opportunity to investigate, in higher detail than what is possible in humans, the effect of *kcnv2* mutations on photoreceptor subtypes. The photoreceptors of 5 mpf *kcnv2* double mutants exhibited only subtle changes detectable through OCT (Figure 4.6 a); however, striking changes to the very same mutant retinae were observed through histology (Figure 4.8 c, d). The global change to photoreceptor outer segments suggests that both rods and cones are dysmorphic in *kcnv2* double mutant zebrafish, which coincides with the functional deficits observed through scotopic and photopic ERG examination, although the morphological deficit is in fact worse than would be expected from the ERG results (Figure 4.9; Figure 4.10). Although the peripheral retina appears intact in human patients with *KCNV2* retinopathy, there may be subtle changes too difficult to detect with OCT. Therefore, the use of our *kcnv2* mutant zebrafish to study the survival of both photoreceptor subtypes may inform the cellular basis for the scotopic functional deficit seen in humans.

Many questions regarding the survival and morphology of photoreceptor cells will be the motivation for future experiments in *kcnv2* mutant zebrafish. Transgenic zebrafish lines featuring fluorescent photoreceptors are currently being crossed with *kcnv2* mutants. Specifically, Rho:GFP and UV:GFP zebrafish lines express green fluorescent protein (GFP) under the rod-specific *rho* promotor and UV cone-specific promotor *sws1*, respectively. Imaging of the individual GFP-labelled rods and cones in progeny of transgenic and *kcnv2* mutant in-crosses will highlight changes in cell morphology, quantity, and health in the absence of Kv8.2. Additionally, transmission electron microscopy will be a useful approach to analyse the dysmorphic outer segments of 5 mpf *kcnv2* mutants. Electron microscopy enables the visualization of subcellular features, such as the structure and organization of photoreceptor outer segment disks. Given the abnormal arrangement and appearance of 5 mpf *kcnv2* mutant outer segments, a closer evaluation of the microanatomy may reveal alterations that shed light on the disease process within both our *kcnv2* mutant fish and *KCNV2* retinopathy. Finally, we will continue our efforts to characterize the expression patterns of K_V8.2a and K_V8.2b within wildtype and mutant zebrafish. Nothing is currently known about the location of either paralog within the zebrafish retina, but functional data from *kcnv2* single mutants in this thesis demonstrates a role for both K_V8.2a and K_V8.2b in vision. Although the presence of two paralogs of *kcnv2* is unique to zebrafish, there is still interesting biology to be explored through the investigation of K_V8.2a and K_V8.2b.

In conclusion, the purpose of this work was to develop an animal model that could be used to help build our understanding of the disease process underlying *KCNV2* retinopathy. Through extensive functional and morphological assessments, I have identified several features of *kcnv2* mutant fish that are consistent with the human phenotype. The specific pathology of human photoreceptors in *KCNV2* retinopathy is not yet known, but the cellular processes and morphological changes occurring within *kcnv2* mutant zebrafish photoreceptors may be shared in the human disease. The work in this thesis is by no means complete or exhaustive, and we intend to continue characterizing *kcnv2* mutant zebrafish in the future. I believe that important insights into both photoreceptor biology and the enigmatic disease mechanism of *KCNV2* retinopathy will be made through the use of *kcnv2* mutant zebrafish.

REFERENCES

Abdelkader, E., Yasir, Z. H., Khan, A. M., Raddadi, O., Khandekar, R., Alateeq, N., Nowilaty, S., AlShahrani, N., & Schatz, P. (2020). Analysis of retinal structure and function in cone dystrophy with supernormal rod response. *Doc Ophthalmol.*, *141*, 23–32. https://doi.org/10.1007/s10633-020-09748-1

Alexander, K. R., & Fishman, G. A. (1984). Supernormal scotopic ERG in cone dystrophy. *Brit J Ophthalmol.*, *68*, 69–78.

Allison, W. T., Barthel, L. K., Skebo, K. M., Takechi, M., Kawamura, S., & Raymond, P. A. (2010). Ontogeny of cone photoreceptor mosaics in zebrafish. *J Comp Neurol.*, *518*(20), 4182–4195. https://doi.org/10.1002/cne.22447

Armstrong-Gold, C. E., & Rieke, F. (2003). Bandpass filtering at the rod to second-order cell synapse in salamander (Ambystoma tigrinum) retina. *J Neurosci.*, *23*(9), 3796–3806. https://doi.org/10.1523/JNEUROSCI.23-09-03796.2003

Attwell, D., Werblin, F. S., & Wilson, M. (1982). The properties of single cones isolated from the tiger salamander retina. *J Physiol.*, *328*, 259–283.

Bader, C. R., Macleish, P. R., & Schwartz, E. A. (1978). Responses to light of solitary rod photoreceptors isolated from tiger salamander retina (cell culture/electrical coupling/reversal potential/current-voltage relationship). *PNAS*, *75*(7), 3507–3511.

Balasubramanian, R., & Gan, L. (2014). Development of retinal amacrine cells and their dendritic stratification. *Curr Ophthalmol.*, *2*(3), 1–11. https://doi.org/10.1007/s40135-014-0048-2

Balay, S. D. (2018). *Cryptochrome expression in the zebrafish retina: Potential implications for magnetoreception*. University of Alberta, Edmonton, AB, Canada.

Barnes, S. (1994). After transduction: Response shaping and control of transmission by ion channels of the photoreceptor inner segment. *Neuroscience*, *58*(3), 447–459. https://doi.org/10.1016/0306-4522(94)90072-8

Barrow, A. J., & Wu, S. M. (2009a). Complementary conductance changes by Ikx and Ih contribute to membrane impedance stability during the rod light response. *Channels*, *3*(5), 301–307.

Barrow, A. J., & Wu, S. M. (2009b). Low-conductance HCN1 ion channels augment the frequency response of rod and cone photoreceptors. *J Neurosci.*, *29*(18), 5841–5853. https://doi.org/10.1523/JNEUROSCI.5746-08.2009

Baylor, D. A., Fuortes, M. G. F., & O'Bryan, P. M. (1971). Receptive fields of cones in the retina of the turtle. *J. Physiol*, *214*, 265–294.

Baylor, D. A., & Nunn, B. J. (1986). Electrical properties of the light-sensitive conductance of rods of the salamander Ambystoma tigrinum. *J Physiol.*, *371*, 115–145.

Beech, D. J., & Barnes, S. (1989). Characterization of a voltage-gated K^+ channel that accelerates the rod response to dim light. *Neuron*, *3*, 573–581.

Biel, M. (2009). Cyclic nucleotide-regulated cation channels. *JBC*, *284*(14), 9017–9021. https://doi.org/10.1074/jbc.R800075200

Biel, M., Wahl-Schott, C., Michalakis, S., & Zong, X. (2009). Hyperpolarization-activated cation channels: From genes to function. *Physiol Rev.*, *89*, 847–885.

https://doi.org/10.1152/physrev.00029.2008

Branchek, T. (1984). The development of photoreceptors in the zebrafish, Brachydanio rerio. *J Comp Neurol.*, *224*(1), 116–122. https://doi.org/10.1002/cne.902240110

Brody, J. R., & Kern, S. E. (2004). Sodium boric acid: A tris-free, cooler conductive medium for DNA electrophoresis. *BioTechniques*, *36*, 214–216.

Brown, H. F., DiFrancesco, D., & Noble, S. J. (1979). How does adrenaline accelerate the heart? *Nature*, *280*, 235–236.

Brown, K. T. (1967). The electroretinogram: Its components and their origins. *Vision Res.*, *8*, 633–677.

Bruening-Wright, A., & Larsson, H. P. (2007). Slow conformational changes of the voltage sensor during the mode shift in hyperpolarization-activated cyclic-nucleotide-gated channels. *J Neurosci.*, *27*(2), 270–278. https://doi.org/10.1523/JNEUROSCI.3801-06.2007

Bustin, S. A., Benes, V., Garson, J. A., Hellemans, J., Huggett, J., Kubista, M., Mueller, R., Nolan, T., Pfaffl, M. W., Shipley, G. L., Vandesompele, J., & Wittwer, C. T. (2009). The MIQE guidelines: Minimum information for publication of quantitative real-time PCR experiments. *Clin Chem.*, *55*(4), 611–622. https://doi.org/10.1373/clinchem.2008.112797

Capera, J., Serrano-Novillo, C., Navarro-Pérez, M., Cassinelli, S., & Felipe, A. (2019). The potassium channel odyssey: Mechanisms of traffic and membrane arrangement. *Int J Mol Sci.*, *20*(734), 1–20. https://doi.org/10.3390/ijms20030734

Chan, J. K. C. (2014). The wonderful colors of the hematoxylin-eosin stain in diagnostic surgical pathology. *Int J Surg Pathol.*, *22*(1), 12–32. https://doi.org/10.1177/1066896913517939

Chaya, T., Matsumoto, A., Sugita, Y., Watanabe, S., Kuwahara, R., Tachibana, M., & Furukawa, T. (2017). Versatile functional roles of horizontal cells in the retinal circuit. *Nature*, *7*, 1–15. https://doi.org/10.1038/s41598-017-05543-2

Chen, S.-K., Badea, T. C., & Hattar, S. (2011). Photoentrainment and pupillary light reflex are mediated by distinct populations of ipRGCs. *Nature*, *476*, 92–95. https://doi.org/10.1038/nature10206

Crespo, C., & Knust, E. (2018). Characterisation of maturation of photoreceptor cell subtypes during zebrafish retinal development. *Biol Open*, *7*(11), 1–13. https://doi.org/10.1242/bio.036632

Czirják, G., Tóth, Z. E., & Enyedi, P. (2007). Characterization of the heteromeric potassium channel formed by Kv2.1 and the retinal subunit Kv8.2 in Xenopus oocytes. *J Neurophysiol.*, *98*(3), 1213–1222. https://doi.org/10.1152/jn.00493.2007

Dai, J., He, J., Wang, G., Wang, M., Li, S., & Yin, Z. Q. (2017). Contribution of GABAa, GABAc and glycine receptors to rat dark-adapted oscillatory potentials in the time and frequency domain. *Oncotarget*, *8*(44), 77696–77709.

DelMonte, D. W., & Kim, T. (2011). Anatomy and physiology of the cornea. *J Cataract Refr Surg.*, *37*(3), 588–598. https://doi.org/10.1016/j.jcrs.2010.12.037

Demarco, P. J., & Powers, M. K. (1989). Sensitivity of ERG components from dark-adapted goldfish retinas treated with APB. *Brain Res.*, *482*, 317–323.

Demontis, G. C., Longoni, B., Barcaro, U., & Cervetto, L. (1999). Properties and functional roles of hyperpolarization-gated currents in guinea-pig retinal rods. *J Physiol.*, *515*(3), 813–828.

https://doi.org/10.1111/j.1469-7793.1999.813ab.x

Dick, E., & Miller, R. F. (1985). Extracellular K+ activity changes related to electroretinogram components I. Amphibian (I-type) retinas. *J Gen Physiol.*, *85*, 885–909.

Dimopoulos, I. S., Hoang, S. C., Radziwon, A., Binczyk, N. M., Seabra, M. C., MacLaren, R. E., Somani, R., Tennant, M. T. S., & MacDonald, I. M. (2018). Two-year results after AAV2-mediated gene therapy for choroideremia: The Alberta experience. *Am J Ophthalmol.*, *193*, 130–142. https://doi.org/10.1016/j.ajo.2018.06.011

Doyle, D. A., Cabral, J. M., Pfuetzner, R. A., Kuo, A., Gulbis, J. M., Cohen, S. L., Chait, B. T., & MacKinnon, R. (1998). The structure of the potassium channel: Molecular basis of K+ conduction and selectivity. *Science*, *280*(5360), 69–77. https://doi.org/10.1126/science.280.5360.69

Enyedi, P., & Czirják, G. (2010). Molecular background of leak K+ currents: Two-pore domain potassium channels. *Physiol Rev.*, *90*, 559–605. https://doi.org/10.1152/physrev.00029.2009

Fadool, J. M. (2003). Development of a rod photoreceptor mosaic revealed in transgenic zebrafish. *Dev Biol.*, *258*(2), 277–290. https://doi.org/10.1016/S0012-1606(03)00125-8

Fan, S., & Yazulla, S. (1997). Electrogenic hyperpolarization-elicited chloride transporter current in blue cones of zebrafish retinal slices. *J Neurophysiol.*, *77*, 1447–1459.

Fernald, R. D. (1997). The evolution of eyes. *Brain Behav Evolut.*, *50*(4), 253–259. https://doi.org/10.1159/000113339

Fleisch, V. C., Jametti, T., & Neuhauss, S. C. F. (2008). Electroretinogram (ERG) measurements in larval zebrafish. *Cold Spring Harb Protoc.*, *3*(3), 1–6.

https://doi.org/10.1101/pdb.prot4973

Forrester, J. V., Dick, A. D., McMenamin, P. G., Roberts, F., & Pearlman, E. (2016). Anatomy of the eye and orbit. In J. V. Forrester (Ed.), *The eye: Basic sciences in practise* (4th ed., pp. 1–102). Elsevier. https://doi.org/10.1016/b978-0-7020-5554-6.00001-0

Frech, G. C., VanDongen, A. M. J., Schuster, G., Brown, A. M., & Joho, R. H. (1989). A novel potassium channel with delayed rectifier properties isolated from rat brain by expression cloning. *Nature*, *340*(6235), 642–645. https://doi.org/10.1038/340642a0

Fujinami, K., Tsunoda, K., Nakamura, N., Kato, Y., Noda, T., Shinoda, K., Tomita, K., Hatase, T., Usui, T., Akahori, M., Itabashi, T., Iwata, T., Ozawa, Y., Tsubota, K., & Miyake, Y. (2013). Molecular characteristics of four Japanese cases with KCNV2 retinopathy: Report of novel disease-causing variants. *Mol Vis.*, *19*, 1580–1590.

Gagnon, J. A., Valen, E., Thyme, S. B., Huang, P., Ahkmetova, L., Pauli, A., Montague, T. G., Zimmerman, S., Richter, C., & Schier, A. F. (2014). Efficient mutagenesis by Cas9 protein-mediated oligonucleotide insertion and large-scale assessment of single-guide RNAs. *PLoS ONE*, *9*(5). https://doi.org/10.1371/journal.pone.0098186

Gauthier, M., Gauvin, M., Lina, J. M., & Lachapelle, P. (2019). The effects of bandpass filtering on the oscillatory potentials of the electroretinogram. *Doc Ophthalmol.*, *138*(3), 247–254. https://doi.org/10.1007/s10633-019-09683-w

Gayet-Primo, J., Yaeger, D. B., Khanjian, R. A., & Puthussery, T. (2018). Heteromeric KV2/KV8.2 channels mediate delayed rectifier potassium currents in primate photoreceptors. *J Neurosci.*, *38*(14), 3414–3427. https://doi.org/10.1523/JNEUROSCI.2440-17.2018

Ghasemi, A., & Zahediasl, S. (2012). Normality tests for statistical analysis: A guide for non-statisticians. *Int J Endocrinol Metab.*, *10*(2), 486–489. https://doi.org/10.5812/ijem.3505

Ginzinger, D. G. (2002). Gene quantification using real-time quantitative PCR: An emerging technology hits the mainstream. *Exp Hemotol.*, *30*(6), 503–512. https://doi.org/10.1016/S0301-472X(02)00806-8

Glasauer, S. M. K., & Neuhauss, S. C. F. (2014). Whole-genome duplication in teleost fishes and its evolutionary consequences. *Mol Genet Genomics*, *3*, 1045–1060. https://doi.org/10.1007/s00438-014-0889-2

Gouras, P., Eggers, H. M., & Mackay, C. J. (1983). Cone dystrophy, nyctalopia, and supernormal rod Responses: A new retinal degeneration. *Arch Ophthalmol.*, *101*(5), 718–724. https://doi.org/10.1001/archopht.1983.01040010718003

Guimaraes, T. A. C. De, Georgiou, M., & Robson, A. G. (2020). KCNV2 retinopathy : clinical features, molecular genetics and directions for future therapy. *Ophthalmic Genet.*, *41*(3), 208–215. https://doi.org/10.1080/13816810.2020.1766087

Haider, N. B., Jacobson, S. G., Cideciyan, A. V, Swiderski, R., Streb, L. M., Searby, C., Beck, G., Hockey, R., Hanna, D. B., Gorman, S., Duhl, D., Carmi, R., Bennett, J., Weleber, R. G., Fishman, G. A., Wright, A. F., Stone, E. M., & Sheffield, V. C. (2000). Mutation of a nuclear receptor gene, NR2E3, causes enhanced S cone syndrome, a disorder of retinal cell fate. *Nat Genet.*, *24*, 127–131.

Halliwell, J. V, & Adams, P. R. (1982). Voltage-clamp analysis of muscarinic excitation in hippocampal neurons. *Brain Res.*, *250*, 71–92.

Hart, N. S., Mountford, J. K., Voigt, V., Fuller-Carter, P., Barth, M., Nerbonne, J. M., Hunt, D. M., & Carvalho, L. S. (2019). The role of the voltage-gated potassium channel proteins Kv8.2 and Kv2.1 in vision and retinal disease: Insights from the study of mouse gene knock-out mutations. *ENeuro*, *6*(1), 1–13. https://doi.org/10.1523/ENEURO.0032-19.2019

Hattar, S., Liao, H.-W., Takao, M., Berson, D. M., & Yau, K.-W. (2002). Melanopsin-containing retinal ganglion cells: Architecture, projections, and intrinsic photosensitivity. *Science*, *295*(5557), 1065–1070. https://doi.org/10.1126/science.1069609

Heginbotham, L., Lu, Z., Abramson, T., & Mackinnon, R. (1994). Mutations in the K+ channel signature sequence. *Biophys J.*, *66*, 1061–1067.

Hibino, H., Inanobe, A., Furutani, K., Murakami, S., Findlay, I., & Kurachi, Y. (2010). Inwardly rectifying potassium channels: Their structure, function, and physiological roles. *Physiol Rev.*, *90*, 291–366. https://doi.org/10.1152/physrev.00021.2009

Hood, D. C., Cideciyan, A. V., Halevy, D. A., & Jacobson, S. G. (1996). Sites of disease action in a retinal dystrophy with supernormal and delayed rod electroretinogram b-waves. *Vision Res.*, *36*(6), 889–901. https://doi.org/10.1016/0042-6989(95)00174-3

Howe, K., Clark, M. D., Torroja, C. F., Torrance, J., Berthelot, C., Muffato, M., Collins, J. E., Humphray, S., McLaren, K., Matthews, L., McLaren, S., Sealy, I., Caccamo, M., Churcher, C., Scott, C., Barrett, J. C., Koch, R., Rauch, G.-J., White, S., … By, coordinated J. (2013). The zebrafish reference genome sequence and its relationship to the human genome. *Nature*, *496*(7446), 498–503. https://doi.org/10.1038/nature12111

Ingram, N. T., Sampath, A. P., & Fain, G. L. (2020). Membrane conductances of mouse cone photoreceptors. *J Gen Physiol.*, *152*(3), 1–11. https://doi.org/10.1085/JGP.201912520

Jardon, B., Yiicel, H., & Bonaventure, N. (1989). Glutamatergic separation of ON and OFF retinal channels: possible modulation by glycine and acetylcholine. *Eur J Pharmacol.*, *162*, 215–224.

Jeon, C.-J., Strettoi, E., & Masland, R. H. (1998). The major cell populations of the mouse retina. *J Neurosci.*, *18*(21), 8936–8946.

Jiang, F., & Doudna, J. A. (2017). CRISPR-Cas9 Structures and Mechanisms. *Annue Rev Biophys.*, *46*, 505–529. https://doi.org/10.1146/annurev-biophys

Kibelbek, J., Mitchell, D. C., Beach, J. M., & Litman, B. J. (1991). Functional equivalence of metarhodopsin II and the Gt-activating form of photolyzed bovine rhodopsin. *Biochemistry*, *30*, 6761–6768.

Kim, D. M., & Nimigean, C. M. (2016). Voltage-gated potassium channels: A structural examination of selectivity and gating. *Cold Spring Harb Perspect Biol.*, *8*, 1–19. https://doi.org/10.1101/cshperspect.a029231

Kiray, G., Rapata, M., Sharp, D., & Vincent, A. L. (2020). Pseudodominance in two families with KCNV2 related retinopathy. *Am J Ophthalmol*, *18*, 1–5. https://doi.org/10.1016/j.ajoc.2020.100625

Kizawa, J., Machida, S., Kobayashi, T., Gotoh, Y., & Kurosaka, D. (2006). Changes of oscillatory potentials and photopic negative response in patients with early diabetic retinopathy. *Jpn J Ophthalmol.*, *50*, 367–373. https://doi.org/10.1007/s10384-006-0326-0

Labun, K., Montague, T. G., Krause, M., Torres Cleuren, Y. N., Akon Tjeldnes, H., & Valen, E. (2019). CHOPCHOP v3: Expanding the CRISPR web toolbox beyond genome editing.

Nucleic Acids Res., *47*, 171–174. https://doi.org/10.1093/nar/gkz365

Lander, E. S. (2011). Initial impact of the sequencing of the human genome. *Nature*, *470*, 187–197. https://doi.org/10.1038/nature09792

Lewis, R., Asplin, K. E., Bruce, G., Dart, C., Mobasheri, A., & Barrett-Jolley, R. (2011). The role of the membrane potential in chondrocyte volume regulation. *J Cell Physiol.*, *226*, 2979–2986. https://doi.org/10.1002/jcp.22646

Li, H., Chuang, A. Z., & O'Brien, J. (2009). Photoreceptor coupling is controlled by connexin 35 phosphorylation in zebrafish retina. *J Neurosci.*, *29*(48), 15178–15186. https://doi.org/10.1523/JNEUROSCI.3517-09.2009

Long, S. B., Campbell, E. B., & Mackinnon, R. (2005). Crystal structure of a mammalian voltage-dependent shaker family K+ channel. *Science*, *309*, 897–903.

Long, S. B., Campbell, E. B., & MacKinnon, R. (2005). Voltage sensor of Kv1.2: Structural basis of electromechanical coupling. *Science*, *303*, 903–908. https://doi.org/10.1126/science.1116269

Magoon, E. H., & Robb, R. M. (1981). Development of myelin in human optic nerve and tract: A light and electron microscopic study. *Arch Ophthalmol.*, *99*(4), 655–659. https://doi.org/10.1001/archopht.1981.03930010655011

Mannu, G. S. (2014). Retinal phototransduction. *Neurosciences*, *19*(4), 275–280.

Marc, R. E., Anderson, J. R., Jones, B. W., Sigulinsky, C. L., Lauritzen, J. S., Soiza-Reilly, M., Kasthuri, N., & Tsukamoto, Y. (2014). The AII amacrine cell connectome: a dense network hub. *Front Neural Circuit*, *8*, 1–13. https://doi.org/10.3389/fncir.2014.00104

Matsui, K., Hosoi, N., & Tachibana, M. (1999). Active role of glutamate uptake in the synaptic transmission from retinal nonspiking neurons. *J Neurosci.*, *19*(16), 6755–6766.

McCulloch, D. L., Marmor, M. F., Brigell, M. G., Hamilton, R., Holder, G. E., Tzekov, R., & Bach, M. (2015). ISCEV Standard for full-field clinical electroretinography (2015 update). *Doc Ophthalmol.*, *130*(1), 1–12. https://doi.org/10.1007/s10633-014-9473-7

Menger, G. J., Koke, J. R., & Cahill, G. M. (2005). Diurnal and circadian retinomotor movements in zebrafish. *Vis Neurosci.*, *22*(2), 203–209. https://doi.org/10.1017/S0952523805222083

Michaelides, M., Holder, G. E., Webster, A. R., Hunt, D. M., Bird, A. C., Fitzke, F. W., Mollon, J. D., & Moore, A. T. (2005). A detailed phenotypic study of "cone dystrophy with supernormal rod ERG." *Brit J Ophthalmol.*, *89*(3), 332–339. https://doi.org/10.1136/bjo.2004.050567

Morshedian, A., Kaylor, J. J., Ng, S. Y., Tsan, A., Frederiksen, R., Xu, T., Yuan, L., Sampath, A. P., Radu, R. A., Fain, G. L., & Travis, G. H. (2020). Light-driven regeneration of cone visual pigments through a mechanism involving RGR opsin in Müller glial cells. *Neuron*, *102*(6), 1172–1183. https://doi.org/10.1016/j.neuron.2019.04.004

Murgatroyd, H., & Bembridge, J. (2008). Intraocular pressure. *BJA Educ.*, *8*(2), 100–103. https://doi.org/10.1093/bjaceaccp/mkn015

Nadolski, N. J., Balay, S. D., Wong, C. X. L., Waskiewicz, A. J., & Hocking, J. C. (2020). Abnormal cone and rod photoreceptor morphogenesis in gdf6a mutant zebrafish. *IOVS*, *61*(4), 1–18. https://doi.org/10.1167/iovs.61.4.9

Nadolski, N. J., Wong, C. X. L., & Hocking, J. C. (2020). Electroretinogram analysis of zebrafish retinal function across development. *Doc Ophthalmol.*, 1–11. https://doi.org/10.1007/s10633-020-09783-y

Nakanishi, S., Nakajima, Y., Masu, M., Yoshiki Ueda, Nakahara, K., Watanabe, D., Yamaguchi, S., Kawabata, S., & Okada, M. (1998). Glutamate receptors: Brain function and signal transduction. *Brain Res Rev.*, *26*, 230–235. https://doi.org/10.1016/S0165-0173(97)00033-7

Nelson, R. F., & Singla, N. (2009). A spectral model for signal elements isolated from zebrafish photopic electroretinogram. *Vis Neurosci.*, *26*, 349–363. https://doi.org/10.1017/S0952523809990113

Nelson, R., & Kolb, H. (2003). ON and OFF pathways in the vertebrate retina and visual system. *Vis Neurosci.*, *1*, 260–278.

Nüsslein-Volhard, C., & Dahm, R. (2002). *Zebrafish: A practical approach*. Oxford University Press.

Ogura, T., Satoh, T. O., Usui, S., & Yamada, M. (2003). A simulation analysis on mechanisms of damped oscillation in retinal rod photoreceptor cells. *Vision Res.*, *43*(19), 2019–2028. https://doi.org/10.1016/S0042-6989(03)00309-2

Okunuki, Y., Mukai, R., Pearsall, E. A., Klokman, G., Husain, D., Park, D. H., Korobkina, E., Weiner, H. L., Butovsky, O., Ksander, B. R., Miller, J. W., & Connor, K. M. (2018). Microglia inhibit photoreceptor cell death and regulate immune cell infiltration in response to retinal detachment. *PNAS*, *115*(27), 6264–6273. https://doi.org/10.1073/pnas.1719601115

Omri, S., Omri, B., Jonet, L., Thillaye-Goldenberg, B., Thuret, G., Gain, P., Jeanny, J. C., Crisanti, P., & Behar-Cohen, F. (2010). The outer limiting membrane (OLM) revisited: Clinical implications. *Clin Ohthalmol.*, *4*, 183–195.

Ottschytsch, N., Raes, A., Van Hoorick, D., & Snyders, D. J. (2002). Obligatory heterotetramerization of three previously uncharacterized Kv channel α-subunits identified in the human genome. *PNAS*, *99*(12), 7986–7991. https://doi.org/10.1073/pnas.122617999

Park, P. S. H. (2019). Rhodopsin oligomerization and aggregation. *J Membane Biol.*, *252*(3), 413–423. https://doi.org/10.1007/s00232-019-00078-1

Pepe, I. M. (1999). Rhodopsin and phototransduction. *J Photochem Photobiol B: Biol.*, *48*, 1–10.

Pepperberg, D. R., & Masland, R. H. (1978). Retinal-induced sensitization of light-adapted rabbit photoreceptors. *Brain Res.*, *151*, 194–200.

Reichenbach, A., & Bringmann, A. (2013). New functions of Müller cells. *Glia*, *61*(5), 651–678. https://doi.org/10.1002/glia.22477

Reichenbach, A., & Bringmann, A. (2020). Glia of the human retina. *Glia*, *68*(4), 768–796. https://doi.org/10.1002/glia.23727

Richardson, R., Tracey-White, D., Webster, A., & Moosajee, M. (2017). The zebrafish eye: A paradigm for investigating human ocular genetics. *Eye*, *31*(1), 68–86. https://doi.org/10.1038/eye.2016.198

Robson, A. G., Webster, A. R., Michaelides, M., Downes, S. M., Cowing, J. A., Hunt, D. M., Moore, A. T., & Holder, G. E. (2010). "Cone dystrophy with supernormal rod electroretinogram": A comprehensive genotype/phenotype study including fundus autofluorescence and extensive electrophysiology. *Retina*, *30*(1), 51–62. https://doi.org/10.1097/IAE.0b013e3181bfe24e

Runkle, E. A., & Antonetti, D. A. (2011). The blood-retinal barrier: Structure and functional significance. In S. Nag (Ed.), *The blood-brain and other neural barriers* (pp. 133–148). Springer.

Sagne, C., Isambert, M.-F., Henry, J.-P., & Gasnier, B. (1996). SDS-resistant aggregation of membrane proteins: application to the purification of the vesicular monoamine transporter. *Biochem J.*, *316*, 825–831.

Santina, L. Della, Piano, I., Cangiano, L., Caputo, A., Ludwig, A., Cervetto, L., & Gargini, C. (2012). Processing of retinal signals in normal and HCN deficient mice. *PLoS ONE*, *7*(1). https://doi.org/10.1371/journal.pone.0029812

Saszik, S., & Bilotta, J. (1999). ERG assessment of zebrafish retinal development. *Vis Neurosci.*, *16*(5), 881–888. https://doi.org/10.1017/S0952523899165076

Schein, S. J. (1988). Anatomy of macaque fovea and spatial densities of neurons in foveal representation. *J Comp Neurol.*, *269*(4), 479–505. https://doi.org/10.1002/cne.902690403

Schindelin, J., Arganda-Carreras, I., Frise, E., Kaynig, V., Longair, M., Pietzsch, T., Preibisch, S., Rueden, C., Saalfeld, S., Schmid, B., Tinevez, J. Y., White, D. J., Hartenstein, V., Eliceiri, K., Tomancak, P., & Cardona, A. (2012). Fiji: An open-source platform for biological-image analysis. *Nat Methods*, *9*(7), 676–682. https://doi.org/10.1038/nmeth.2019

Schneeweis, D. M., & Schnapf, J. L. (1995). Photovoltage of rods and cones in the macaque retina. *Science*, *268*(5213), 1053–1056. https://doi.org/10.1126/science.7754386

Seeliger, M. W., Brombas, A., Weiler, R., Humphries, P., Knop, G., Tanimoto, N., & Müller, F. (2011). Modulation of rod photoreceptor output by HCN1 channels is essential for regular mesopic cone vision. *Nat Commun.*, *2*(1), 1–10. https://doi.org/10.1038/ncomms1540

Seeliger, M. W., Rilk, A., & Neuhauss, S. C. F. (2002). Ganzfeld ERG in zebrafish larvae. *Doc Ophthalmol.*, *104*(1), 57–68. https://doi.org/10.1023/A:1014454927931

Segev, A., Garcia-Oscos, F., & Kourrich, S. (2016). Whole-cell patch-clamp recordings in brain slices. *J Vis Exp.*, *112*, 54024. https://doi.org/10.3791/54024

Sergouniotis, P. I., Holder, G. E., Robson, A. G., Michaelides, M., Webster, A. R., & Moore, A. T. (2012). High-resolution optical coherence tomography imaging in KCNV2 retinopathy. *Br J Ophthalmol.*, *96*, 213–217. https://doi.org/10.1136/bjo.2011.203638

Sillman, A. J., Ito, H., & Tomita, T. (1969). Studies on the mass receptor potential of the isolated frog retina. *Vision Res.*, *9*(12), 1435–4451.

Słomka, M., Sobalska-Kwapis, M., Wachulec, M., Bartosz, G., & Strapagiel, D. (2017). High resolution melting (HRM) for high-throughput genotyping-Limitations and caveats in practical case studies. *Int J Mol Sci.*, *18*, 1–21. https://doi.org/10.3390/ijms18112316

Smith, K. E., Wilkie, S. E., Tebbs-Warner, J. T., Jarvis, B. J., Gallasch, L., Stocker, M., & Hunt, D. M. (2012). Functional analysis of missense mutations in Kv8.2 causing cone dystrophy with supernormal rod electroretinogram. *JBC*, *287*(52), 43972–43983. https://doi.org/10.1074/jbc.M112.388033

Sperelakis, N. (2011). Origin of resting membrane potentials. In N. Sperelakis (Ed.), *Cell physiology source book: Essentials of membrane biophysics* (4th ed., pp. 121–145).

Elsevier.

Steinberg, R. H., Schmidt, R., & Brown, K. T. (1970). Intracellular responses to light from cat pigment epithelium: Origin of the electroretinogram c-wave. *Nature*, *227*, 728–730.

Strauss, O. (2005). The retinal pigment epithelium in visual function. *Physiol Rev.*, *85*, 845–881. https://doi.org/10.1152/physrev.00021.2004

Sun, C., Galicia, C., & Stenkamp, D. L. (2018). Transcripts within rod photoreceptors of the zebrafish retina. *BMC Genom.*, *19*(1), 1–18. https://doi.org/10.1186/s12864-018-4499-y

Sun, C., Mitchell, D. M., & Stenkamp, D. L. (2018). Isolation of photoreceptors from mature, developing, and regenerated zebrafish retinas, and of microglia/macrophages from regenerating zebrafish retinas. *Exp Eye Res.*, *177*, 130–144. https://doi.org/10.1016/j.exer.2018.08.002

Thoreson, W. B., & Bryson, E. J. (2004). Chloride equilibrium potential in salamander cones. *BMC Neurosci.*, *5*(53), 1–7. https://doi.org/10.1186/1471-2202-5-53

Thyme, S. B., & Schier, A. F. (2016). Polq-mediated end joining is essential for surviving DNA double-strand breaks during early zebrafish development. *Cell Reports*, *15*(4), 707–714. https://doi.org/10.1016/j.celrep.2016.03.072

Tsang, S. H., & Sharma, T. (2018). *Atlas of inherited retinal diseases*. Springer.

Van Hook, M. J., Nawy, S., & Thoreson, W. B. (2019). Voltage- and calcium-gated ion channels of neurons in the vertebrate retina. *Prog Retin Eye Res.*, *72*, 1–34. https://doi.org/10.1016/j.preteyeres.2019.05.001

Vergara, C., Latorre, R., Marrion, N. V, & Adelmant, J. P. (1998). Calcium-activated potassium channels. *Curr Opin Neurobiol.*, *8*, 321–329. http://biomednet.com/elecref/0959438800800321

Vincent, A., Wright, T., Garcia-Sanchez, Y., Kisilak, M., Campbell, M., Westall, C., & Héon, E. (2013). Phenotypic characteristics including in vivo cone photoreceptor mosaic in KCNV2-related "cone dystrophy with supernormal rod electroretinogram." *IOVS*, *54*(1), 898–908. https://doi.org/10.1167/iovs.12-10971

Wang, J.-S., & Kefalov, V. J. (2011). The cone-specific visual cycle. *Prog Retin Eye Res.*, *30*(2), 115–128. https://doi.org/10.1016/j.preteyeres.2010.11.001

Ward, R., Kaylor, J. J., Cobice, D. F., Pepe, D. A., McGarrigle, E. M., Brockerhoff, S. E., Hurley, J. B., Travis, G. H., & Kennedy, B. N. (2020). Non-photopic and photopic visual cycles differentially regulate immediate, early and late-phases of cone photoreceptor-mediated vision. *JBC*, *295*(19), 6482–6497. https://doi.org/10.1074/jbc.ra119.011374

Weinstein, G. W., Hobson, R. R., & Dowling, J. E. (1967). Light and dark adaptation in the isolated rat retina. *Nature*, *215*(5097), 134–138. https://doi.org/10.1038/215134a0

Wen, X., & Thoreson, W. B. (2019). Contributions of glutamate transporters and Ca2+-activated Cl− currents to feedback from horizontal cells to cone photoreceptors. *Exp Eye Res.*, *189*, 1–13. https://doi.org/10.1016/j.exer.2019.107847

Werblin, F. S. (1975). Regenerative hyperpolarization in rods. *J Physiol.*, *244*, 53–81.

Werblin, F. S., & Dowling, J. E. (1969). Organization of the retina of the mudpuppy, Necturus macubsus. II. Intracellular recording. *J Neurophysiol.*, *32*, 339–355.

Westerfield, M. (2000). *The zebrafish book. A guide for the laboratory use of zebrafish (Danio* *rerio)* (4th ed.). University of Oregon Press.

Wissinger, B., Dangel, S., Jägle, H., Hansen, L., Baumann, B., Rudolph, G., Wolf, C., Bonin, M., Koeppen, K., Ladewig, T., Kohl, S., Zrenner, E., & Rosenberg, T. (2008). Cone dystrophy with supernormal rod response is strictly associated with mutations in KCNV2. *IOVS*, *49*(2), 751–757. https://doi.org/10.1167/iovs.07-0471

Wong, K. Y., Adolph, A. R., & Dowling, J. E. (2004). Retinal bipolar cell input mechanisms in giant danio: Electroretinographic analysis. *J Neurophysiol.*, *93*, 84–93. https://doi.org/10.1152/jn.00259.2004

Wu, H., Cowing, J. A., Michaelides, M., Wilkie, S. E., Jeffery, G., Jenkins, S. A., Mester, V., Bird, A. C., Robson, A. G., Holder, G. E., Moore, A. T., Hunt, D. M., & Webster, A. R. (2006). Mutations in the gene KCNV2 encoding a voltage-gated potassium channel subunit cause "cone dystrophy with supernormal rod electroretinogram" in humans. *Am J Hum Genet.*, *79*(3), 574–579. https://doi.org/10.1086/507568

Xie, J., Jusuf, P. R., Goodbourn, P. T., & Bui, B. V. (2019). Electroretinogram recording in larval zebrafish using a novel cone-shaped sponge-tip electrode. *J Vis Exp.*, *145*, 1–7. https://doi.org/10.3791/59487

Xu, X., & Karwoski, C. (1995). Current source density analysis of the electroretinographic d-wave of frog retina. *J Neurophysiol.*, *73*(6), 2459–2469.

Yu, W., Xu, J., & Li, M. (1996). NAB domain is essential for the subunit assembly of both-and-complexes of shaker-like potassium channels. *Neuron*, *16*, 441–453.

Zelinger, L., Wissinger, B., Eli, D., Kohl, S., Sharon, D., & Banin, E. (2013). Cone dystrophy with supernormal rod response: Novel KCNV2 mutations in an underdiagnosed phenotype. *Ophthalmology*, *120*(11), 2338–2343. https://doi.org/10.1016/j.ophtha.2013.03.031

Zhao, L., Zabel, M. K., Wang, X., Ma, W., Shah, P., Fariss, R. N., Qian, H., Parkhurst, C. N., Gan, W., & Wong, W. T. (2015). Microglial phagocytosis of living photoreceptors contributes to inherited retinal degeneration. *EMBO Mol Med.*, *7*(9), 1179–1197. https://doi.org/10.15252/emmm.201505298

Zobor, D., Kohl, S., Wissinger, B., Zrenner, E., & Jägle, H. (2012). Rod and cone function in patients with KCNV2 retinopathy. *PLoS ONE*, *7*(10). https://doi.org/10.1371/journal.pone.0046762